Fatigue behavior of continuous-discontinuous sheet molding compounds

Zur Erlangung des akademischen Grades einer

DOKTORIN DER INGENIEURWISSENSCHAFTEN (Dr.-Ing.)

von der KIT-Fakultät für Maschinenbau des
Karlsruher Instituts für Technologie (KIT)

angenommene

DISSERTATION

von

Miriam Bartkowiak, M.Sc.

Tag der mündlichen Prüfung:	03. März 2022
Hauptreferent:	Prof. Dr.-Ing. Kay André Weidenmann
Korreferenten:	John Montesano, Ph.D., P.Eng.
	Prof. Dr.-Ing. Peter Elsner

Abstract

Sheet molding compound (SMC) composites have been well-established as non-structural and semi-structural components in vehicles due to their high lightweight potential. Over the past decade, increasing need for further vehicle weight reduction has fueled endeavors to further improve mechanical properties of SMC and thereby to expand their suitability as structural components. One promising approach to achieve this goal is the combination of discontinuous glass fiber SMC with local continuous carbon fiber reinforcement, which is currently being investigated by the German-Canadian research training group GRK 2078. Such hybrid continuous-discontinuous composites enable the production of components with excellent mechanical properties while maintaining the advantages of the SMC process including geometric flexibility, short cycle times and cost efficiency. However, several factors prevent the exploitation of the composite's full potential. Major obstacles for a safe and efficient application of continuous-discontinuous SMC are the lack of knowledge regarding their fatigue behavior and about uncharted effects of hybridization on damage behavior under cyclic loading conditions.

This thesis describes a systematical analysis of the fatigue behavior of continuous-discontinuous SMC both under cyclic tensile and bending loads at different temperatures and frequencies. The hybrid composite, which consists of a discontinuous glass fiber SMC core and unidirectional carbon fiber SMC face plies, shows significantly higher fatigue resistance compared to discontinuous SMC without continuous reinforcement. The effect of hybridization is more pronounced under cyclic loading than under monotonic loading, which is a result of distinct damage mechanisms acting at distinct applied stresses. The mechanical behavior of continuous-discontinuous SMC is dominated by the continuous plies at high

stresses and by the discontinuous ply at low stresses. The effect of hybridization is particularly distinctive under cyclic bending load on account of the composite's sandwich-like structure. In addition, relative stiffness degradation of continuous-discontinuous SMC is less pronounced over a larger loading period compared to discontinuous SMC. While damage evolution within the discontinuous SMC ply remains largely unaffected by hybridization, the continuous SMC plies are enabled to withstand significantly higher cyclic loads than continuous SMC specimens that are not a part of a hybrid composite. When using a cross-ply instead of a unidirectional continuous reinforcement, early initiation of cracks in the 90° ply at comparatively low stresses leads to rapidly growing delaminations and large cracks in the discontinuous SMC ply. Consequently, the effect of hybridization under cyclic loading is less pronounced. While continuous-discontinuous SMC is largely insensitive to a change in frequency, enhanced temperature leads to early failure of the unidirectional ply on the compression loaded side, which results in a significant decrease of fatigue life.

Kurzfassung

Sheet Molding Compounds (SMC) werden aufgrund ihres Leichtbaupotentials bereits seit längerer Zeit erfolgreich als nicht-strukturelle und semi-strukturelle Bauteile in Fahrzeugen eingesetzt. Aufgrund des zunehmenden Bedarfs an einer weiteren Gewichtsreduzierung bei Fahrzeugen zielte die Entwicklung in den letzten zehn Jahren darauf ab, die mechanischen Eigenschaften von SMC derart zu verbessern, dass der Verbundwerkstoff auch für strukturelle Anwendungen eingesetzt werden kann. Ein vielversprechender Ansatz, der derzeit vom deutsch-kanadischen Graduiertenkolleg GRK 2078 untersucht wird um dieses Ziel zu erreichen, besteht in der Kombination von diskontinuierlich verstärktem Glasfaser-SMC mit einer lokalen Endloskohlenstofffaserverstärkung. Aus solch einem hybriden Verbundwerkstoff können Bauteile mit hervorragenden mechanischen Eigenschaften hergestellt und dennoch die Vorteile des SMC-Verfahrens beibehalten werden. Zu diesen Vorteilen gehören vor allem die geometrische Designfreiheit, kurze Zykluszeiten und Kosteneffizienz. Allerdings limitieren mehrere Faktoren die Ausschöpfung des vollen Werkstoffpotentials. Fehlende Kenntnisse über das Ermüdungsverhalten und die Auswirkungen der Hybridisierung auf das Schädigungsverhalten unter zyklischen Belastungsbedingungen stellen eine große Hürde für eine sichere und effiziente Auslegung und Anwendung dar.

Diese Arbeit beschreibt die systematische Analyse des Ermüdungsverhaltens von kontinuierlich-diskontinuierlich verstärktem SMC sowohl unter zyklischer Zugbeanspruchung als auch unter zyklischer Biegebeanspruchungen bei unterschiedlichen Temperaturen und Frequenzen. Der Hybrid, der aus einem

diskontinuierlichen Glasfaser-SMC-Kern und unidirektionalen Kohlenstofffaser-SMC-Decklagen besteht, zeigt im Vergleich zu rein diskontinuierlich verstärktem SMC deutlich höhere Ermüdungsfestigkeiten und Lebensdauern. Der Effekt der Hybridisierung ist bei zyklischer Belastung stärker ausgeprägt als bei monotoner Belastung und ist unter Biegebelastung aufgrund der Sandwichstruktur besonders groß. Darüber hinaus ist die relative Steifigkeitsdegradation im kontinuierlich-diskontinuierlichem SMC über einen größeren Belastungszeitraum hinweg geringer. Während die Schädigungsentwicklung in der diskontinuierlichen SMC-Lage durch die Hybridisierung weitgehend unbeeinflusst bleibt, führen Wechselwirkungen zwischen den Lagen dazu, dass die in den Hybridverbund integrierte kontinuierliche Kohlenstofffaser-SMC-Lage deutlich höheren zyklischen Belastungen standhalten kann als kontinuierliche SMC-Proben, die nicht Teil eines Hybridverbunds sind. Bei Verwendung einer kreuzweisen kontinuierlichen Verstärkung anstelle einer unidirektionalen, führt die frühe Rissbildung in der 90°-Lage bei vergleichsweise geringen Spannungen zu schnell wachsenden Delaminationen und großen Rissen in der diskontinuierlichen SMC-Lage. Dementsprechend sind Hybridisierungseffekte unter zyklischer Belastung weniger stark ausgeprägt. Während kontinuierlich-diskontinuierlich verstärktes SMC weitgehend unempfindlich gegenüber einer Veränderung der Frequenz ist, führt eine erhöhte Temperatur zu einem wesentlich schnelleren Versagen der unidirektionalen Kohlenstofffaser-SMC-Lage auf der druckbelasteten Seite, was eine reduzierte Ermüdungslebensdauer zur Folge hat.

Acknowledgement

The research documented in this doctoral thesis was conducted within the framework of the International Research Training Group "Integrated engineering of continuous-discontinuous long fiber-reinforced polymer structures" (GRK 2078) and has been funded by the German Research Foundation (DFG). The support by the DFG is gratefully acknowledged. The thesis summarizes the research I conducted during three and a half pleasant and eventful years at the Institute for Applied Materials, Karlsruhe Institute of Technology. I would like to thank those who supported and encouraged me and during this time and have contributed to my professional and personal development.

First and foremost, I wish to express my gratitude to my supervisor Prof. Kay André Weidenmann for the continuous support and encouragement, for all the helpful advice, for his trust and for always taking time to discuss my questions and concerns. I appreciate very much the high value you attribute to the good supervision of your doctoral students. You have provided me with the best framework to focus on my research and to work on this thesis I am incredibly grateful that I was able to experience such dedicated scientific guidance. My gratitude goes also to my second supervisor Prof. John Montesano. Thank you for the opportunity to be part of your research group at the University of Waterloo, for being interested in my work and for the fruitful discussions, valuable feedback and advice that enriched my research. I would also like to thank Prof. Peter Elsner for taking the time to evaluate my thesis.

Furthermore, I sincerely appreciate the encouraging support by Willi Liebig, who has headed our group Hybrid and Lightweight Materials since April 2019. Although you took on this task at the most difficult and stressful time due to

the pandemic, you always found time for intensive scientific discussions, brain storming and for giving me input that greatly improved my work.

Many thanks to all my current and former colleagues and friends at the Institute for Applied Materials (IAM-WK) at KIT, the International Research Training Group GRK 2078 and the Composites Research Group at the University of Waterloo for numerous discussions, for unfailing helpfulness and for an all in all very pleasant and enjoyable atmosphere at work. I gratefully thank Anna Trauth, from whom I learned a lot especially in my early days at the Institute and always helped me with her professional expertise when I had questions. Many thanks to Benedikt Scheuring, who provided valuable support in the testing laboratory while I was busy and stressed writing the thesis and lightened up my mood with his cheerful and enthusiastic manner. Special thanks to my office colleague Ludwig Schöttl for providing and processing the µCT scans, for the pleasant and productive atmosphere at the office and also for the great time we spend together in Canada. Thanks to Sergej Ilinzeer for the time and effort to manufacture the materials. Furthermore, many thanks to Henrik Werner for hours of intensively discussing my scientific questions, for valuable advice but also for the nice activities we spend besides the work place, which were important to be able to switch off from work once in a while. Thanks to Christoph Breuner, who was always there for me when I needed a friend to talk but also when I needed his know-how in the fatigue testing laboratory. I would also like to thank the technical staff at the IAM-WK, in particular Sebastian Höhne, Ralf Rößler, Marc Brecht and Michaela Nagel for their irreplaceable support with technical questions and problems.

I greatly acknowledge the good work and high motivation of all students, who contributed to the contents of this work, especially Hannes Weit, Melike Kizak, Maria Isabel Aliano Ramos and Nikol Vlavaki.

My gratitude goes also to my friends who motivated me but also provided the necessary distraction when I needed it. My sincere thanks go to my dance partner Kai Becker for the support, inspiration and motivation, for listening to my problems so I could get them out of my head and for cheering me up in difficult times. The joy of going to practice and dancing with you in the evenings

helped me get through the most stressful times. Many thanks also to Thomas and Tatjana Bilich for the motivation and encouragement especially within the last few months. Thank you so much Tatjana, for thoroughly checking the thesis for spelling and grammatical errors.

Last but not least I would like to thank my family with all my heart for their love and support. I will never stop being grateful that my parents gave me all the opportunities they didn't have themselves and who laid the groundwork for my accomplishments. Thank you, Manuel, for being proud of me and my achievements, especially in times when I doubted myself, for understanding that I have been focusing a lot on myself and my work and thank you for making sure I was happy, healthy and had a good work-life balance when sometimes I forgot to worry about those things myself.

Contents

Acronyms and symbols

Acronyms

AE	Acoustic emission
C20	20 % by weight continuous fibers
$CaCO_3$	Calcium carbonate
CF	Carbon fiber
CFRP	Carbon fiber-reinforced polymer
CDS	Characteristic damage state
Co	Continuous
CoDiCo	Continuous-discontinuous (0° reinforcement)
$CoDiCo^{0/90}$	Continuous-discontinuous (0°/90° reinforcement)
CV	Coefficient of variation
DIC	Digital image correlation
DiCo	Discontinuous
FRP	Fiber-reinforced polymer
GF	Glass fiber
GFRP	Glass fiber-reinforced polymer

GRK	Graduate school
HM	Hybrid material
HO	Highly oriented
IR	Infrared
M_1	Material 1
M_2	Material 2
POI	Point of interest
PTFE	Polytetrafluoroethylene
R25	25 % by weight randomly oriented fibers
R30	30 % by weight randomly oriented fibers
R50	50 % by weight randomly oriented fibers
R65	65 % by weight randomly oriented fibers
RO	Randomly oriented
SMC	Sheet molding compound
S-N	Stress-life
TGA	Thermogravimetric analysis
T-T	Tension-tension
UPPH	Unsaturated polyester-polyurethane hybrid resin
UFS^F	Ultimate flexural strength at fatigue strain rate
UFS^S	Ultimate flexural strength at quasi-static strain rate
UTS^F	Ultimate tensile strength at fatigue strain rate
UTS^S	Ultimate tensile strength at quasi-static strain rate

vol.-%	Volume percent
wt.-%	Weight percent
1D	One-dimensional
2D	Two-dimensional
µCT	Micro-computed tomography

Latin symbols and variables

A	Area
A_{D}	Damaged area
b	Width
D	Damage parameter
E	Modulus of elasticity
E_{dyn}	Dynamic stiffness
$E_{\mathrm{dyn,4}}$	Initial dynamic stiffness
$\bar{E}_{\mathrm{dyn,4}}$	Average initial dynamic stiffness
E_{fat}	Fatigue modulus
F	Force
f	Frequency
h	Thickness
L	Span length
$L_{\mathrm{c,total}}$	Accumulated crack length
L_{g}	Gauge length

N	Number of cycles
N_{f}	Number of cycles to failure
P_{1}	Parameter
P_{2}	Parameter
P_{S}	Probability of failure
R	Stress ratio
T	Temperature
v	Velocity

Greek symbols and variables

α	Coefficient of thermal expansion
δ	Deflection
ε	Strain
ε_{t}	Failure strain
γ	Volume fraction
μ	Standard deviation
ν	Poisson's ratio
ρ	Density
ρ_{w}	Weighted crack length
σ	Stress
σ^{F}	Fatigue stress
$\tilde{\sigma}$	Comparative stress

$\bar{x}$	Mean value

Operators and math symbols

Δ	Difference

General deep indexes

$(\cdot)_{0}$	Initial
$(\cdot)_{\mathsf{flex}}$	Flexural
$(\cdot)_{\mathsf{max}}$	Maximium
$(\cdot)_{\mathsf{min}}$	Minimum
$(\cdot)_{\mathsf{tens}}$	Tensile

1 Introduction

1.1 Continuous-discontinuous FRP composites

Fiber-reinforced polymers (FRPs) have become indispensable for aircraft, automotive, wind power and leisure industries due to their high specific strength and stiffness and the possibility to design material properties specifically tailored for an application. FRPs consist of a matrix that can either be a comparatively brittle thermoset, or a more flexible thermoplastic and are mostly reinforced with glass fibers (GFRPs) or carbon fibers (CFRPs). Glass fibers are comparatively cheap and are therefore used preferentially for cost-critical applications. Carbon fibers are more expensive and are favorable for applications requiring higher strength and stiffness. These fibers are especially convenient for lightweight construction due to their outstanding specific mechanical properties in the fiber direction.

FRPs can further be classified as continuously or discontinuously fiber-reinforced. In continuous FRPs, fiber length is limited solely by structural dimensions, which allows for the achievement of the highest stiffnesses and strengths. Therefore, continuous FRPs composites are often deployed in aerospace, wind turbines or sporting goods. However, due to their poor flowability, continuous fibers come along with limitations regarding feasible part geometries thus reducing design freedom to parts not exceeding a certain curvature. Furthermore, manufacturing of continuous FRPs components is expensive. The conventional autoclaving process is capital-, labor- and energy-intensive and production cycles are typically measured in hours (Malnati, 2015). In contrast, discontinuous FRPs can be molded into complex geometries, featuring tight radii and rib structures, due

to their ability to flow during the molding process. In contrast to continuous FRPs, the production of discontinuous FRPs is considerably budget-friendly. Their suitability for rapid and high-volume manufacturing makes them specifically interesting for automotive components. Sheet molding compound (SMC) composites, for example, which are thermoset-based discontinuous composites (typically glass fiber-reinforced), that are manufactured by compression molding, are well-established and widely utilized for non-structural and semi-structural automotive components. Their use in structural components, however, is not yet established as they are inferior to continuous or unidirectional FRPs in terms of stiffness and strength as a result of their limited fiber length.

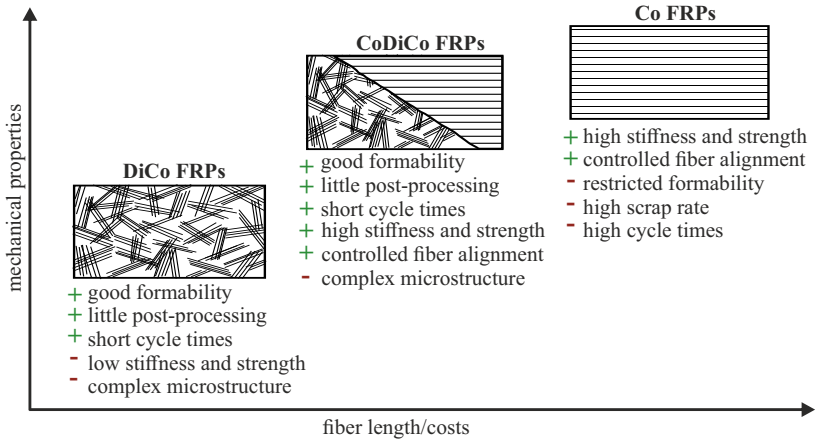

Figure 1.1: Mechanical properties and costs of continuous (Co), discontinuous (DiCo) and continuous-discontinuous (CoDiCo) FRPs.

The consortium of the International Research Group GRK 2078 "Integrated engineering of continuous-discontinuous long fiber-reinforced polymer structures" (CoDiCo FRP) aims to explore hybrid composites uniting the design freedom of low cost discontinuous GFRPs with the high stiffness and strength of unidirectional CFRPs (Figure 1.1). Both components are combined in a one-step molding process in order to create complex shaped SMC parts with a local continuous reinforcement, where highest mechanical properties are required. The

main objective is the development of manufacturing, modeling, dimensioning and characterization concepts for CoDiCo FRP parts (Böhlke et al., 2016).

Hybrid CoDiCo FRPs hold the potential to substitute other materials in automotive structural components to further reduce vehicle mass. An example for such an application is the CFRP subframe combining continuous and chopped fiber SMC in a co-molding process, which was developed within the scope of a joint research project of Ford Motor Co. (Dearborn, MI, US) and Magna International (Aurora, ON, Canada) and is depicted in Figure 1.2 (Gardiner, 2018). The subframe is located in the front of the vehicle and supports the engine and chassis components, subjecting it to significant loads. Another example for an automotive application of continuous-discontinuous SMC was presented by Bruderick et al. (2013), who reported on the use of unidirectional carbon fibers to selectively stiffen the windshield surround in the 2003 Dodge Viper, which is primarily composed of chopped glass and carbon fiber SMC.

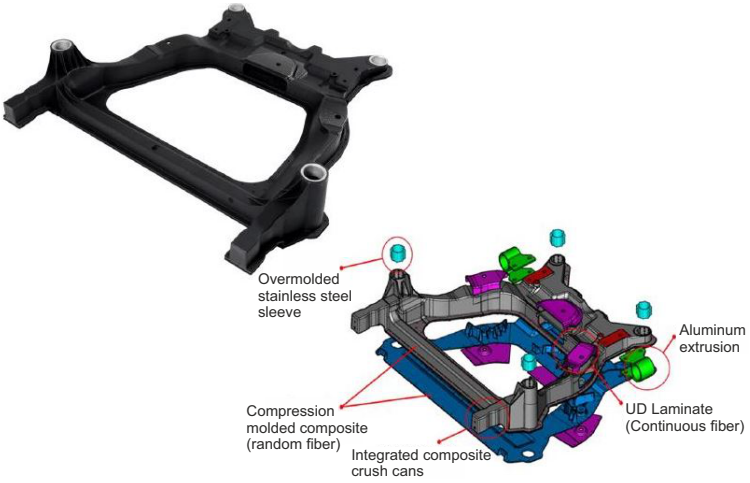

Figure 1.2: Continuous-discontinuous carbon fiber composite subframe (Gardiner, 2018).

1.2 Challenges of hybrid composites

Despite all the advantages of CoDiCo FRPs, structural complexity remains an important challenge. Hybrid composites are anisotropic and heterogenous on both the macroscale and the microscale. Numerous parameters can be modified, such as the type of fiber and matrix as well as length, orientation and volume content of fibers. In flowable composites such as discontinuous SMC, the fiber orientation and curvature are process-dependent and influenced by the movement of the conveyor belt, the geometry of the mold, the initial mold coverage and the molding parameters. Complexity is further enhanced by hybridization with continuous carbon fibers. The additional reinforcement not only yields an additional interface with an individual property profile but also influences the discontinuous material's flow and thus the resulting microstructure. To reduce experimental effort for material characterization and to enable modeling mechanical behavior, identification of process-structure-property relationships is crucial.

Besides the versatility of the microstructure, interactions between the different components on the micro level results in a material behavior, that cannot be captured accurately based solely on their individual macroscopic properties. A detailed knowledge of the damage mechanisms and their respective influences on material performance is necessary to evaluate effects of hybridization. These aspects taken into account, Trauth (2020) introduced adapted experimental methods and analytical tools for characterizing and modeling mechanical behavior of CoDiCo SMC under different monotonic loading conditions. In addition, Trauth (2020) introduced criteria to evaluate hybridization effects and emphasized the strong dependence on the load case, since distinct damage mechanisms are relevant for distinct loading conditions. For example, tensile and compressive moduli of elasticity can be estimated with sufficient accuracy by using a rule of mixtures, while more sophisticated modeling approaches are required to describe the flexural behavior and strength parameters of a hybrid material. The results suggest a divergence of hybridization effects under cyclic loading from those observed under monotonic loading, thus calling for a re-evaluation when the hybrid composite is subjected to fatigue.

1.3 Fatigue of hybrid composites

The damage behavior of hybrid composites is very complex especially under cyclic loading conditions. Constraining effects change the deformation behavior of the individual components. Mechanical properties of the different plies degrade at distinct rates leading to an alternation in load distribution from cycle to cycle, thereby making every constant amplitude cyclic load to a problem of variable amplitude fatigue. The properties of the interface can also be progressively damaged due to fatigue, which must be taken into account. In addition, damage mechanisms occurring in one of the constituents can trigger damage in the other. Since most engineering applications are exposed to cyclic loading and the vast majority of mechanical failures are attributed to fatigue damage (Mortazavian and Fatemi, 2015), such hybridization effects need to be understood and accounted for when dimensioning hybrid composite structures.

1.4 Objectives and scope

The aim of this work is to characterize the fatigue behavior of hybrid CoDiCo SMC composites and to provide a deeper understanding of hybridization effects under different cyclic loading conditions. To this end, general aspects of hybrid materials and their properties, followed by an introduction to the material systems at hand and a comprehensive literature review of the state-of-the-art of CoDiCo SMC composites are introduced. Fundamentals on the fatigue of FRPs in general as well as current know-how on fatigue of continuous FRPs and discontinuous SMC are assessed and discussed. A review of common experimental techniques for damage analysis in FRPs allows for the identification of the most suitable method to characterize the evolution of damage in CoDiCo SMC during cyclic loading. Together with the theoretical background, an extensive experimental program, that includes tension-tension fatigue tests as well as more application-related bending fatigue tests at different frequencies and temperatures, provides the foundation

for evaluation of fatigue properties of continuous, discontinuous and continuous-discontinuous SMC on coupon level and for the analysis of hybridization effects. This includes the determination of stress-dependent fatigue lives, stress- and cycle-dependent loss of mechanical properties and underlying damage mechanisms. A closer look on unidirectional plies and 0°/90° plies, two different types of continuous reinforcement in the context of hybrid materials, demonstrates the influence of a variation of fiber architecture on damage behavior and material properties. Suitable damage parameters and state-of-the-art modeling strategies in terms of their applicability for CoDiCo SMC composites are discussed in light of possible service life predictions.

2 State of the art

2.1 Hybrid materials

2.1.1 Definition and general aspects

Common engineering materials cover only parts of Ashby's modulus-density space (Figure 2.1), leaving vast blank regions, referred to as *holes*, that offer potential for material development (Ashby, 2011). The general idea behind hybrid materials is to combine two or more materials to achieve a property profile, that monolithic materials cannot offer and in turn fill these *holes*, at least partially.

According to the general idea behind hybrid materials, every composite material can be called a hybrid. Composite materials consist of a matrix and a reinforcement, that can be either fibrous or particulate. While heterogenous on a microscopic scale, a composite material behaves as a homogenous continuum on a macroscopic scale and can be described by its own set of mechanical and physical properties (Ashby, 2011).

The definition of hybrid materials is not constrained to macroscopic homogeneity. Consequently, materials that are inhomogenous on a macroscopic scale can also fall in the category of hybrid materials. One such example is a sandwich structure consisting of two face plies and a core material. When applying a bending load, which represents the most prominent load case for sandwich structures, both components fulfill different tasks within the hybrid. The main task of the core material is the separation of the face plies to increase the geometrical moment of inertia, whereas the face plies themselves carry the large share of the load. The

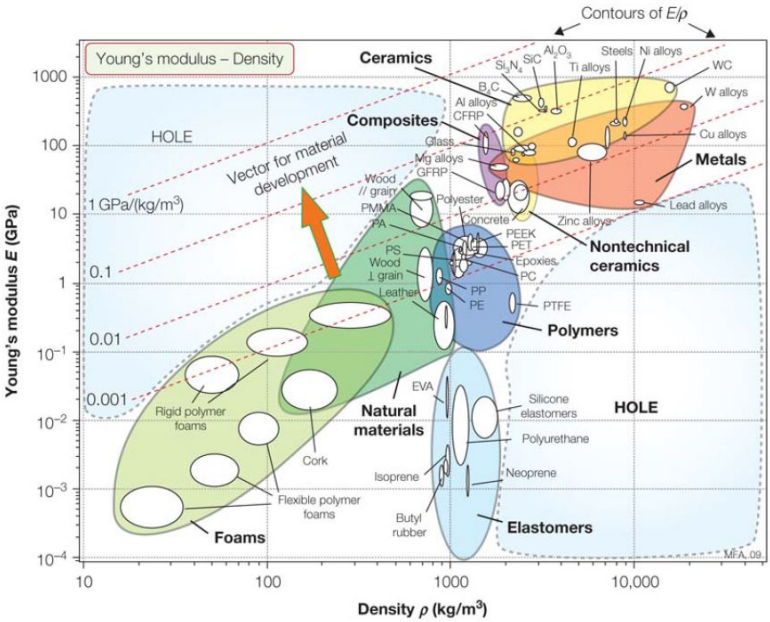

Figure 2.1: Modulus-density space containing common engineering materials as well as *holes* that show potential for material development (Ashby, 2011).

core material therefore has to be light, while being stiff and strong enough to carry shear stresses, whereas the face layers must feature high stiffness and strength under tension or compression, respectively. A corresponding sandwich structure has the potential to fill the upper left hole in Figure 2.1, with the core having low density and the surface plies having a high Young's Modulus. The individual materials forming a macroscopically inhomogenous hybrid can be monolithic, but also composite materials (Henning et al., 2011). In the sandwich structure example, the face sheets themselves can be FRPs.

In this thesis, only polymer-based fiber composites are considered. To avoid confusion, the term *hybrid composite* is used henceforth to describe a polymer-based composite containing two different types of fibrous reinforcement (e.g.

carbon and glass), that can be either continuous or discontinuous. Different possible configurations of hybrid composites are depicted in Figure 2.2. A crucial aspect in hybrid composites is the dispersion of the different fiber types. It is defined as the reciprocal of the smallest repeat length and is thus a measure for how well the fiber types are mixed. In Figure 2.2, the dispersion increases from (a) to (d).

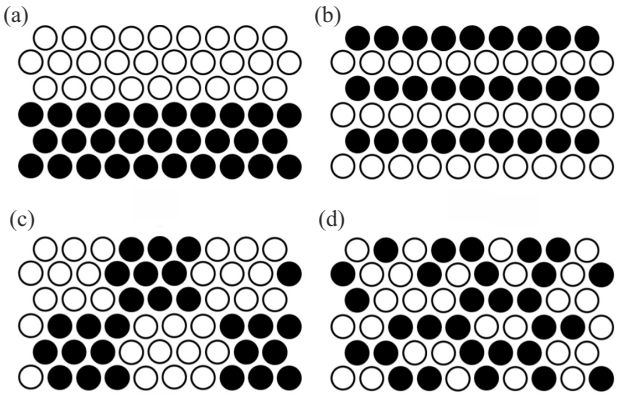

Figure 2.2: Possible configurations of hybrid composites featuring different degrees of dispersion (a) two layers, (b) alternating layers, (c) bundle-by-bundle dispersion and (d) completely random dispersion (Swolfs et al., 2014). The white and black circles represent two different fiber types.

2.1.2 Evaluation of hybrid materials

Even though hybrid composites can be heterogenous on a macroscopic scale, there is merit for treating them as homogenous materials with their own effective properties. In this way, the mechanical behavior of hybrid composites can be compared with that of the individual components (Ashby, 2011). Depending on the material configuration, the way the materials are combined and depending on the use case, different possibilities arise for the effective properties, that can

be achieved. Ashby (2011) defined four scenarios, each typical for a different material combination and use case, that are shown in Figure 2.3.

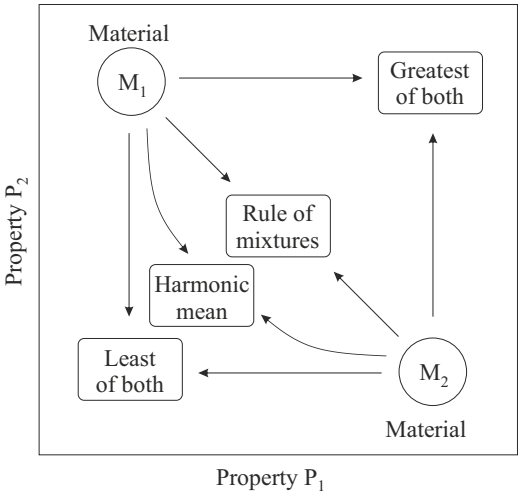

Figure 2.3: Possible effective properties of hybrid materials resulting from the properties of the individual components (Ashby, 2011).

The *best of both* scenario is often achieved when the bulk material properties of one component are combined with the surface properties of the second component (e.g. zinc-coated steel, featuring the high mechanical properties of steel and the corrosion resistance of zinc). The *rule of mixtures* scenario states, that the effective properties correspond to the arithmetic average of the properties of the components, weighted by their volume fractions. This is the theoretical maximum that can be achieved when combining the bulk properties of the different components. For example, the tensile modulus of elasticity of unidirectional FRPs is close to the rule of mixtures. Sometimes the effective properties of hybrids are dominated by the weaker link with effective properties being below the rule of mixtures and rather close to the *harmonic mean* scenario. Such a behavior can be found, for example, in particulate composites. The *least of both* scenario is achieved when one component of a hybrid is designed to fail early to fulfill a

certain function. An example is a wax-metal hybrid for fire sprinkler systems, whose function is determined by the melting point of the wax.

Prior to analyzing hybridization effects in terms of mechanical properties, there must be clarity about whether the individual components perform different tasks (as in the case of zinc-coated steel) or the same task (as when combining bulk properties of different components). In the latter case, the effect of hybridization can be expressed by a positive or negative deviation of the considered material property from a linear rule of mixtures (Marom et al., 1978; Summerscales and Short, 1978), as depicted in Figure 2.4a. However, while the linear rule of mixtures is suitable to determine elastic properties in the longitudinal direction when the different components are arranged in parallel (Trauth, 2020), other mechanical properties, such as strength, cannot be approximated in a similar way (Huang and Zhou, 2012). Manders and Bader (1981), who studies hybrid glass/carbon fiber composites, found the strength to rather follow a bilinear rule of mixtures.

An effect of hybridization can also be expressed by an enhancement of a certain property of the hybrid material with respect to one of the components, which serves as a reference (Yahaya et al., 2014; Trauth, 2020), as depicted in Figure 2.4b. In this example, the hybrid material's strength increases with respect to material 2, which can be considered a positive hybridization effect. Furthermore, the hybrid material's failure strain increases with respect to reference material 1, which can also be considered a positive hybridization effect. This approach is easier to implement and can also be used for a broader range of properties.

2.1.3 Effects of hybridization

Several researchers investigated effects of hybridization while most of them focused on hybrid composites combining different continuous fiber reinforcements. Early investigations were concerned with the failure strain enhancement of carbon fibers when combined with glass fibers (Hayashi, 1972). One reason for this effect is a change in the way damage develops, which can be traced back to the statistical nature of the carbon fibers' strength (Swolfs et al., 2014). When

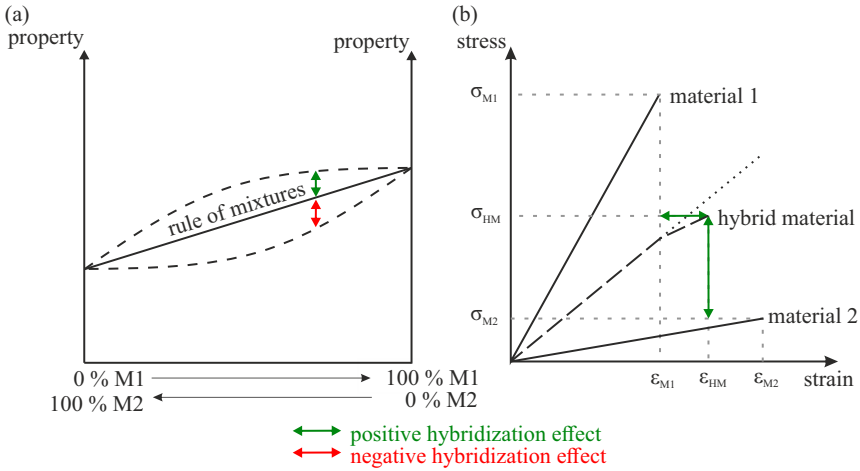

Figure 2.4: Definitions of hybridizations effects in terms of (a) a positive or negative deviation from the linear rule of mixtures and (b) a deviation of a distinct property of the hybrid with respect to one of the components serving as reference.

applying a strain to a unidirectional carbon fiber composite, first fibers start to fracture locally at some point. The fiber breaks are randomly distributed in the volume. Neighboring fibers will be subjected to stress concentrations and locally take over the additional load, which leads to an increasing failure probability in the neighboring fibers. Further strain enhancement leads to an increased failure probability of the neighboring fibers, which results in the development of broken fiber clusters. Once those clusters reach a critical size, they grow in an unstable manner, which results in final failure (Talreja, 1981). Hybridization with more ductile glass fibers can lead to a reduction of the stress concentrations, which interferes with the cluster development, and can also bridge the more brittle carbon fibers, leading to an increased critical cluster size. The remaining carbon fiber fragments, that are still fully involved in the load transfer at a certain distance from the location of fracture, feature a higher failure strains, as their *weakest link* got eliminated already. Ultimately, the hybrid fails more gradually (Swolfs et al., 2014).

Furthermore, residual stresses also contribute to the hybridization effect on the failure strain (Swolfs et al., 2014). They result from the manufacturing process due to different coefficients of thermal expansion of the different fibers. During the manufacturing process of carbon/glass hybrid composites, temperature is increased to cure the resin matrix which results in an elongation of the glass fibers, whereas the carbon fibers almost maintain their length or even shorten to a small degree. After the resin is cured and the composite is cooled down, the glass fibers would shrink again, if they were not constrained by the surrounding material. This results in the establishment of a force equilibrium putting tensile stresses on the glass fibers and compressive stresses on the carbon fibers. The compressive stresses counteract the applied stress, which results in an apparent increase in failure strain of the carbon fibers (Swolfs et al., 2014). However, the effect of residual stresses is insufficient to explain the full hybrid effect (Zweben, 1977; Manders and Bader, 1981).

Effects of hybridization depend on various factors, such as the relative amount of fibers, their elastic properties, the failure strain ratio, the fiber strength distribution and the degree of dispersion (Swolfs et al., 2014). Due to the complexity of many parameters, prediction of hybridization effects remains challenging. Furthermore, most studies focus on the hybridization effect on failure strain. If failure strain is enhanced, a corresponding increase in tensile strength may be expected, when the fibers deform in a linear elastic manner. However, the reason for the failure strain enhancement is mainly attributed to a more gradual failure, meaning that the last part of the stress-strain curve is not linear anymore, as depicted in 2.4b, and may even reach a plateau.

Only few studies on the effect of hybridization with regard to fatigue properties exist. Dickson et al. (1989) carried out tension-tension fatigue tests on glass/carbon hybrid composites in an alternating layer configuration (cf. Figure 2.2b) with different fiber volume ratios. The fatigue strength for a given number of cycles to failure varied linearly with the relative volume ratio of the fibers. Since the tensile strength did not vary in a linear but rather in a bilinear way with this ratio, a positive hybridization effect on the fatigue resistance was implied (Figure 2.5a). The effect was observed for both unidirectional and quasi-isotropic layups.

Since the authors noted that a linear rule of mixtures may not be appropriate for evaluation of fatigue resistance, hybridization effects were additionally evaluated based on the fatigue ratio, which was defined by the fatigue stress at a given number of cycles divided by the monotonic tensile strength (Figure 2.5b). The hybrid composites featured a higher fatigue ratio than both single-fiber CFRP and GFRP composites. Dickson et al. (1989) further noticed increased scatter of the stress-life data compared to the single-fiber composites.

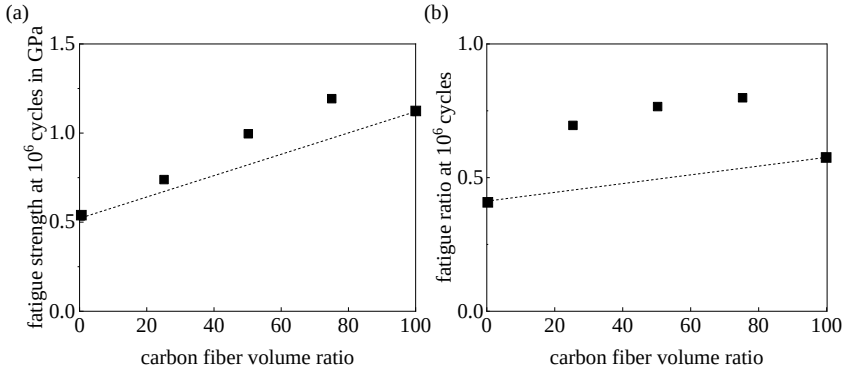

Figure 2.5: Hybridization effect on the fatigue response of hybrid glass/carbon composites expressed in terms of (a) deviation from the linear rule of mixtures and (b) the fatigue ratio (Dickson et al., 1989).

Hofer et al. (1978) studied quasi-isotropic glass/carbon epoxy hybrids in alternating configuration and found the tensile fatigue behavior to be comparable to that of CFRP when using a carbon to glass ratio of 2:1. Hofer et al. (1978) named the uniform distribution of plies as a crucial factor for the good performance and indicates that sandwich-like constructions have a severe modulus mismatch at the interface, which leads to high interlaminar shear stresses promoting earlier failure.

2.2 Sheet molding compound composites

2.2.1 Discontinuous SMC composites

Sheet molding compounds (SMC) are thermoset semi-finished materials containing discontinuous fiber bundles with a typical length of 25.4 mm (1 inch) or 50.8 mm (2 inches) at a fiber weight fraction between 10 % and 65 % (Orgéas and Dumont, 2011). Usually, SMC is processed by compression molding into predominantly shell-shaped geometries. Various types of fiber reinforcements can be used with glass fibers being the most common choice. In most cases, the thermoset resin is either polyester, vinyl ester or epoxy resin containing various additives (initiators, inhibitors, thickeners and mold release agents) and fillers (e.g. calcium carbonate) to prevent shrinkage during molding, thereby enabling the production of Class-A surfaces (Orgéas and Dumont, 2011). In addition to conventional SMC, there are also alternative material compositions that aim to further improve the mechanical properties (cf. Section 2.2.1.5).

2.2.1.1 Manufacturing

Manufacturing of SMC components includes two process steps: Manufacturing of SMC semi-finished sheets and compression molding (Orgéas and Dumont, 2011). In the first step of compounding, the resin system is applied to a carrier foil. Glass fiber bundles are cut to the desired length by a cutting unit and fall onto the carrier foil in almost transverse isotropic alignment. A second carrier foil with the resin system is placed on top of the lower foil before the sandwich passes through the calendering zone, which ensures a good impregnation of the fibers. Subsequently, the material is rolled up and left for maturation for several days. After maturation, the material is cut into sheets, then freed from the carrier foil and ultimately stacked into packages of several plies. The so-called initial charge is placed into the mold typically covering 30 % to 70 % of the mold surface. The mold is closed and the material flows into its final shape. The flow causes a certain re-orientation of the fiber bundles, which affects the local microstructure.

This process is strongly influenced by the temperature rise that varies across the thickness direction (Ehrenstein, 2006), resulting in plug flow in the core and preferential flow near the mold surface. The resulting material microstructure is mainly characterized by preserved fiber bundles (Meyer et al., 2020) oriented predominantly in flow direction, while in a small region near the charge-mold interface the bundles are broken up roughly and the fibers exhibit strong curvature (Le et al., 2008). Cross-linking of the thermoset eventually leads to a solid part. Solidification takes about 1 min to 5 min, depending on the thermoset matrix and part thickness (approximately 1 min per mm thickness).

2.2.1.2 Mechanical properties

Standard SMC composites used in the automotive industry are produced with an isotropic fiber distribution and have a rather low fiber content due to the use of fillers, that are added to obtain a good surface quality. By increasing the fiber content and simultaneously reducing the filler content (Taggart et al., 1979; Riegner and Sanders, 1979; Trauth, 2020) and by partially aligning the fibers in loading direction during the molding process (Trauth, 2020), mechanical properties can be significantly improved. To give a rough overview of the mechanical performance of quasi-isotropic polyester-based SMC that is typically used in the automotive industry compared to partially aligned SMC based on an unsaturated polyester-polyurethane hybrid (UPPH) resin without fillers in 0° and 90° direction, the corresponding tensile and flexural properties are summarized in Table 2.1. As a result of the partial alignment of the fibers in the UPPH-based SMC described by Trauth (2020), the mechanical properties are higher in flow direction (0° direction) compared to transverse direction (90° direction). Due to the high fiber volume content, mechanical properties in 90° direction are still comparable to those of the quasi-isotropic SMC studied by Orgéas and Dumont (2011), despite the less favorable fiber orientation.

Table 2.1: Tensile (E_{tens}) and flexural (E_{flex}) modulus of elasticity, as well as ultimate tensile strength (UTS^S) and ultimate flexural strength (UFS^S) at quasi-static strain rate of polyester-based SMC with a nominal glass fiber content of 25 wt.-% and fillers (calcium carbonate) with an approximately isotropic fiber orientation (Orgéas and Dumont, 2011) and properties of UPPH-based SMC in 0° and 90° direction with a nominal glass fiber content of 41 wt.-% (without fillers) that experienced one-dimensional flow (Trauth, 2020).

	Orgéas and Dumont (2011)	Trauth (2020)	Trauth (2020)
Resin	Polyester	UPPH	UPPH
Fiber content in wt.-%	25	41	41
Fiber orientation	quasi-isotropic	0° (1D flow)	90° (1D flow)
E_{tens} in GPa	10	13.1	9.5
E_{flex} in GPa	10	12.6	9.1
UTS^S in MPa	75	177	90
UFS^S in MPa	170	283	170

2.2.1.3 Viscoelastic behavior

The values stated in Table 2.1 were determined at quasi-static strain rates and ambient temperature. Jendli et al. (2004) showed that the mechanical behavior of unsaturated polyester-based SMC with 26 wt.-% fibers and calcium carbonate fillers is strongly strain rate-dependent. In corresponding studies, an increased strain rate resulted in a delayed onset of damage and ultimate failure at higher stresses and strains. Furthermore, stiffness and strength of SMC is temperature-dependent, as shown by Denton (1979) (Figure 2.6), who studied polyester-based SMC with different fiber volume fractions and calcium carbonate fillers. Above room temperature, strength decreased at a high rate with increasing temperature, whereas the temperature-dependence was less pronounced at lower temperatures. Heimbuch and Sanders (1978), who studied different types of SMC with respect to the matrix system, observed no temperature dependence of tensile strength below room temperature and an increasing influence at about 50 °C for epoxy-based

SMC, while polyester-based SMC showed a pronounced temperature dependence, even at subambient temperatures.

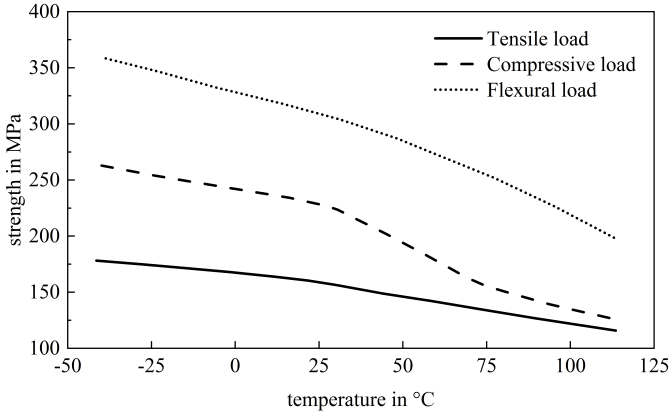

Figure 2.6: Temperature influence on the tensile, compressive and flexural strength of polyester-based SMC according to Denton (1979).

2.2.1.4 Damage mechanisms under tensile load

The predominant damage mechanisms in SMC are matrix cracking and fiber-matrix debonding. Interface failure between overlapping fiber bundles, hereinafter referred to as pseudo-delamination, can also be observed, usually immediately prior to final failure (Trauth, 2020). Fiber bundle fracture is rarely observed (Wang and Chim, 1983; Trauth, 2020). Transverse matrix cracks are induced in matrix-rich regions or in fiber-rich regions where fibers are oriented in loading direction. These cracks form abruptly due to the brittleness of the matrix and arrest at fiber bundles. If fiber bundles are oriented at an angle to the loading direction, microcracks tend to grow along the interface between fiber and matrix. Figure 2.7 shows a stress-strain curve typical for SMC with a knee point at a stress that is dictated by the strain rate. A similar behavior is already known from studies on cross-ply laminates described by Puck (1967).

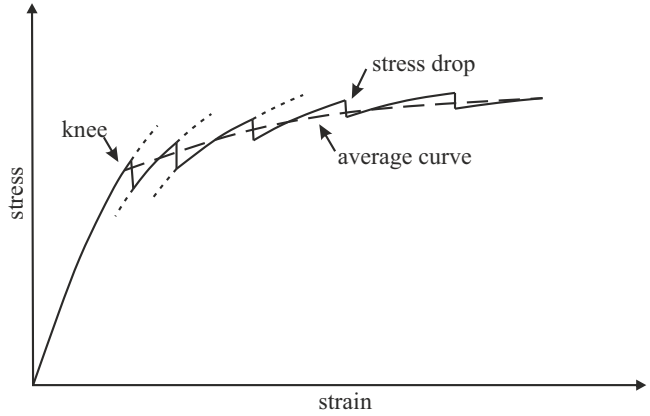

Figure 2.7: Schematic stress-strain curve of SMC, according to von Bernstorff (1989), showing the characteristic knee point and an enlarged view on the small stiffness drops caused by multiple cracking, that lead to a successive decrease of the curve.

No significant damage occurs within the first linear range. When reaching the so-called knee stress, the formation of multiple matrix cracks leads to a gradual stiffness decrease. This was demonstrated for example by von Bernstorff (1989), who combined tensile tests with acoustic emission analysis and observed, that no acoustic emission was measured in the linear elastic strain range, while the knee point correlated with an abrupt strong increase of acoustic emission. Von Bernstorff (1989) and Wang and Chim (1983) also found a link between the knee point and multiple cracking in fractographic analysis. Since the energy necessary for arrested cracks to grow further is very high, additional loading leads to new cracks initiating at different locations. Multiple small drops in the stress-strain curve, caused by multiple cracking, lead to a decreasing slope of the macroscopic curve (Owen, 1982). Shortly before final failure, large-scale interfacial bundle-matrix debonding (referred to as pseudo-delamination) and pull-out of fiber bundles dominate the failure process (Trauth, 2020) and lead to a loss of load-bearing capacity.

2.2.1.5 Recent developments

Several documented approaches were aiming to improve the mechanical performance of SMC composites and thus facilitating their use for structural applications. One approach is the increase of fiber volume content (Shirinbayan et al., 2015, 2017) together with a reduction of the filler content. Another approach is to align the discontinuous fibers in loading direction, which can be done either by introducing discontinuity into aligned continuous fibers by breaking and cutting (Taketa et al., 2008), or by aligning short fibers using fluid, acoustic, electrical, or mechanical mechanisms (Such et al., 2014). Combining a glass fiber and a carbon fiber reinforcement (Wulfsberg et al., 2014) or using carbon fibers exclusively (Nony-Davadie et al., 2019) are other approaches, that have been pursued increasingly in recent years. Finally, combining discontinuous SMC with continuous reinforcement offers the possibility of producing parts with high stiffness and strength while retaining the advantages of conventional SMC (Böhlke et al., 2019). This approach is discussed in detail in Section 2.2.3. In light of the recent progress made in SMC technology, SMC composites are considered as equally suitable candidates for structural applications and might even enter the aerospace industry in the near future (Wulfsberg et al., 2014).

2.2.2 Continuous SMC composites

For a long time, a major hurdle in the automotive industry was the development of faster production processes for continuous FRP parts based on thermosets, which require time to cross-link. A conventional prepreg part cured in an autoclave has production cycles that are usually measured in hours. Since the development of non-autoclave processes and fast-curing resins, continuous FRP structures can be produced cost-effectively and with shorter cycle times (Malnati, 2015). One of these processes is prepreg compression molding, in which specifically formulated, pre-shaped CFRP prepregs can be molded into simple geometries.

An adapted SMC process for the production of unidirectional carbon fiber SMC based on an UPPH resin was presented by Bücheler and Henning (2016). In this process, unidirectional fabric is fed to a slightly modified conveyor belt. The resin is a two-step curing system providing a stable and highly viscous B-stage that is beneficial for cutting, preforming and handling (Trauth, 2020). This stage is achieved by raising the temperature after impregnating the fibers to initiate cross-linking reactions, which are then stopped in a controlled manner by cooling the material back to room temperature. Continuous SMC parts can subsequently be produced by compression molding with mechanical properties similar to those of CFRPs produced by conventional autoclave-based methods (Trauth et al., 2016). The material also offers the possibility for co-molding with discontinuous SMC, as both share the same resin system. Due to the flowability of discontinuous fibers, this in turn enables the production of more complex parts with a local reinforcement for improved mechanical performance: so-called continuous-discontinuous SMC (cf. Section 2.2.3).

2.2.3 Continuous-discontinuous SMC composites

2.2.3.1 Existing concepts and preliminary investigations

The idea of reinforcing discontinuous glass fiber SMC with unidirectional carbon fibers for the cost-efficient achievement of excellent mechanical properties is not new, in general. In the 1970s, the automotive industry became increasingly interested in reducing vehicle mass by replacing metal parts with FRPs, particularly because of a federal law that set fuel economy standards for passenger cars in terms of minimum miles per gallon (US Congress, 1975). Glass fiber composites are cost-effective, but stiffness is frequently a critical aspect in automotive applications. The excellent mechanical properties of continuous carbon fiber composites and their potential for weight saving were highly recognized at that time, but the high cost of carbon fibers limited their use in automotive components. It became obvious that a combination of low-cost glass fiber composites

and high-performance carbon fibers would be the most feasible approach to retain cost effectiveness. It was also recognized that aerospace-typical designs and manufacturing methods were not suitable for automotive applications.

To the authors knowledge, the first research activities on such a hybrid approach and its possible applications in the automotive sector, were reported at the mechanical session "Composite Materials in the Automobile Industry" held in San Francisco in 1978 (Kulkarni et al., 1978). Kliger (1978) investigated materials with a core of randomly oriented chopped glass fibers in a polyester or fast-curing epoxy matrix and unidirectional or bidirectional (0° on the outside and 90° on the inside) carbon fiber face sheets. The preimpregnated glass fibers were cured in a compression mold together with stacks of carbon fiber prepreg (one to four plies on each side). Kliger (1978) examined tensile and flexural properties for different sandwich thicknesses, ratios of carbon to glass fiber plies, as well as glass fiber orientations. An overview of the investigated properties for the epoxy-based and the polyester-based hybrid composites with different ratios of chopped glass and unidirectional carbon fibers is provided in Table 2.2 and Table 2.3, respectively.

Chamis and Sinclair (1978) already considered local carbon fiber reinforcements in structures made of chopped glass fiber SMC, which were referred to as *strip hybrids*. They presented a computational study, in which they subjected a strip reinforced random composite square panel to static, cyclic or impulsive loads to demonstrate their structural efficiency. The matrix system considered for the study has not been specified.

Another approach to generate continuous-discontinuous SMC followed by Jutte and Fiberglas (1979), who presented a process to manufacture advanced SMC consisting of a discontinuous glass fiber reinforcement combined with continuous glass fibers of variable fiber volume contents. The different reinforcement types were already combined during manufacturing of the semi-finished sheets on the conveyor belt (Figure 2.8). A high-reactivity isophthalic polyester resin was used as the matrix material. Jutte and Fiberglas (1979) reported superior tensile properties compared to SMC with an entirely discontinuous reinforcement, but at the expense of flowability. Compared to an entirely continuous reinforcement,

Table 2.2: Properties of epoxy-based SMC that was reinforced with different numbers of continuous carbon fiber plies (Kliger, 1978).

face plies	none	1 x 0°	2 x 0°	3 x 0°	4 x 0°	4 x 0°	2 x 0° and 2 x 90°
T in °C	22	22	22	22	22	22 / 82	22 / 82
h_{carbon} in mm	0	0.25	0.58	0.71	0.91	1.01	1.01
h_{glass} in mm	2.29	2.29	2.29	2.29	2.29	2.11	2.11
UFS^S in MPa	443	660	758	800	924	938 / 538	745 / 579
E_{flex} in GPa	22.7	51.7	66.2	76.5	88.3	86.6 / 69.6	61.4 / 57.9
UTS^S in MPa	284	356	466	554	631		
E_{tens} in GPa	25.4	38.6	46.9	55.2	60.7		

Table 2.3: Properties of discontinuous polyester-based SMC that was reinforced with different numbers of continuous carbon fiber plies (Kliger, 1978).

face plies	none	1 x 0°	2 x 0°	3 x 0°	4 x 0°
T in °C	22 / 82	22 / 82	22 / 82	22 / 82	22 / 82
h_{carbon} in mm	0	0.25	0.58	0.76	1.14
h_{glass} in mm	2.41	2.41	2.41	2.41	2.41
UFS^S in MPa	354 / 227	411 / 251	538 / 282	648 / 347	683 / 379
E_{flex} in GPa	15.2 / 11.0	39.3 / 33.1	53.1 / 42.1	64.1 / 48.3	71.7 / 55.8
UTS^S in MPa	251 / 154	330 / 284	412 / 326	469 / 372	552 / 460
E_{tens} in GPa	17.9 / 13.1	30.3 / 26.9	37.2 / 32.4	40.0 / 37.9	48.3 / 45.5

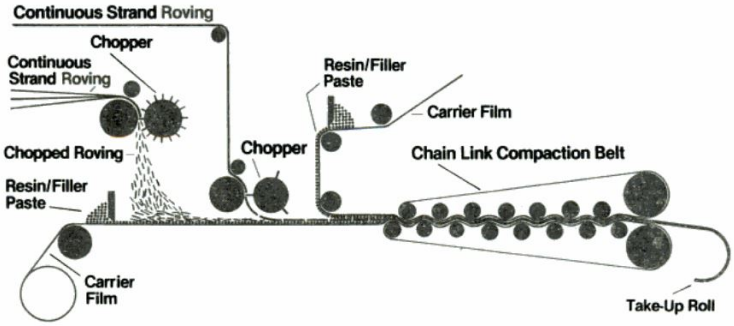

Figure 2.8: Modified SMC line to manufacture continuous-discontinuous semi-finished sheets for compression molding presented by Jutte and Fiberglas (1979).

processing and charge handling prior to molding was improved, transverse mechanical properties were enhanced and the feasibility to incorporate minor bosses and ribs was increased.

Further investigations of the mechanical properties of continuous-discontinuous FRPs with glass fibers being used as continuous and discontinuous reinforcement followed by Taggart et al. (1979), Riegner and Sanders (1979), Kay (1982), Sridharan (1982), Kundrat et al. (1982), Springer (1983) and Mallick (1986).

Taggart et al. (1979) studied mechanical properties of polyester-based SMC with different fiber volume fractions as well as a hybrid composites with 30 wt.-% chopped glass fibers and 20 wt.-% continuous glass fibers under tension and compression load. The authors reported a significant increase of the material's stiffness and strength in the fiber direction while transverse tensile modulus and strength were not significantly affected.

Riegner and Sanders (1979) characterized the fatigue behavior of similar polyester-based hybrid composites under tension-tension load at 5 Hz in longitudinal and transverse direction. Fatigue tests were carried out at ambient temperature and at 90 °C. The authors found that the slope of the longitudinal stress-life (S-N) curve was higher compared to the slope of the transverse curve. However, relative to the

ultimate static tensile strength (UTS^S), the fatigue behavior was similar in both directions. The modulus decay was found to be higher in transverse direction compared to the longitudinal direction. At a stress level of 40 % UTS^S, 93 % of the initial modulus was retained after 10^6 cycles in longitudinal direction and 50 % in transverse direction. In longitudinal direction, the fatigue behavior at 90 °C was similar to that observed at room temperature, while the material showed a temperature-dependent behavior in transverse direction.

Kay (1982) investigated the mechanical properties of hybrids with a chopped glass fiber-reinforced core and a continuous glass fiber-reinforced skin with varying layup sequences. The matrix was a low-profile isophthalic polyester resin without fillers. Tensile, compressive, flexural, shear and impact strength, as well as Poisson's ratio were determined. Mechanical properties of the hybrid laminates increased by factors of two to four compared to purely discontinuous reinforced SMC. Kay (1982) also reported that the continuous fibers retarded the matrix damage that regularly occurs early in the strain history of discontinuous SMC.

Sridharan (1982) focused on modeling the linear elastic behavior of continuous-discontinuous glass fiber-reinforced composites as laminates of plies with different reinforcement types in a vinyl ester matrix. The elastic moduli of different hybrid compositions could successfully be calculated from the constituent plies. Strength calculations only provided useful estimates of the tensile strengths.

Kundrat et al. (1982) studied the fatigue damage behavior of two different continuous-discontinuous glass fiber-reinforced composite materials based on a vinyl ester resin with a small amount of calcium carbonate fillers. The first material system contained 60 wt.-% continuous glass and 5 wt.-% randomly oriented fibers. The second material contained 45 wt.-% continuous and 20 wt.-% randomly oriented fibers. Discontinuous fibers featured a length of 25.4 mm. The outer plies of the symmetric laminates contained short random fibers in both cases. S-N curves were determined for both material systems by testing at maximum stresses between 20 % and 80 % UTS^S at a stress ratio of $R = 0.05$ and a frequency of 3.3 Hz for high stress levels and 10 Hz for low stress levels.

Residual strength, stiffness and damping measurements were carried out to investigate the degradation behavior. In both cases, the material sustained more than $3 \cdot 10^6$ cycles at stresses that corresponded to 38 % UTS^S. No investigations were pursued with composites containing solely unidirectional or randomly oriented fibers. Effects of hybridization could thus not be examined.

Springer (1983) investigated effects of moisture and temperature on the properties of polyester-based continuous-discontinuous SMC. The properties surveyed include tensile strength and modulus, compression strength and modulus, shear strength and modulus, flexural strength and modulus, fatigue, creep, vibration damping, moisture absorption characteristics and thermal expansion. Results on the effect of temperature reported by Springer (1983) are presented in Section 2.3.4.3.

Mallick (1986) was concerned with the effect of cross-flow when co-molding continuous-discontinuous SMC. The sheets were produced on a SMC machine that added a layer of continuous E-glass fiber rovings on top of a layer of randomly oriented chopped E-glass fiber strands. The matrix was a vinyl ester resin. Continuous fiber buckle and bow-out in the direction of cross-flow was observed for two different fiber architectures with the continuous fibers being oriented unidirectionally and X-patterned, respectively. The influence of fiber misorientation on the mechanical properties was investigated in tension tests.

Although the advantages of continuous-discontinuous FRP could be clearly set out, no further research activities were published in the following decades. In 2014, a process for hybrid compression molding of unidirectional carbon fiber prepreg and discontinuous carbon fiber SMC was presented by Akiyama (2014). The matrix was a bisphenol A type epoxy resin, which was optimized for both the preform and the compression molding process. Bending tests were carried out on specimens with several laminate designs and an increase of strength or stiffness was observed when positioning the prepreg on the crosshead or support side of the specimen respectively. Prepreg reinforcement of SMC also reduced the variation of mechanical properties. Furthermore, a hybrid structural floor model part for automotive applications was developed. The interface strength between prepreg

and SMC of a co-molded part was superior compared to an adhesively bonded structure when tested at elevated temperatures.

Tension and bending tests on hybrid materials containing unidirectional and randomly oriented discontinuous glass fibers in an epoxy matrix were carried out by Selmy et al. (2011) on different layups to investigate the effect of stacking sequences and relative volume fraction of randomly oriented fibers on the tensile strength, tensile modulus, Poisson's ratio, bending strength and bending stiffness. In 2012, the same research group investigated the in-plane shear properties (Selmy et al., 2012a) and the interlaminar shear properties (Selmy et al., 2012b) of the same hybrid materials. They observed that forming hybrid composites with random glass fibers considerably improved in-plane shear properties of unidirectional fiber composites. In contrast interlaminar shear strength of unidirectional composite did not benefit from a hybrid configuration and was higher than both, that of the hybrid as well as that of the random composite.

Wulfsberg et al. (2014) took up the idea of co-molding discontinuous SMC and unidirectional or woven prepreg with the continuous plies being positioned in the core of the laminate. In contrast to the work of Selmy et al. (2011), carbon fibers were used for both types of reinforcements and an unsaturated polyester resin served as matrix material. The positive effect of hybridization on mechanical properties was demonstrated by means of tension and bending tests. Further studies were conducted by the same research group to develop an appropriate manufacturing procedure (Fette et al., 2016) and a microstructural modeling approach for the prediction of the elastic properties (Fette et al., 2017).

Gortner et al. (2015a) analyzed a hybrid material combining discontinuous SMC composites based on an unsaturated polyester resin reinforced with non-crimp glass or carbon fiber fabrics that were impregnated during the molding process. Different symmetric and asymmetric layups were analyzed. Strong focus was set on the impregnation behavior of the dry fabric depending on the filler content in the SMC semi-finished material. Tension and bending properties as well as Charpy impact resistance and puncture resistance were determined (Gortner et al., 2015b).

Corbridge et al. (2017) co-molded unidirectional carbon fiber prepreg and advanced SMC made from chips of unidirectional prepreg. The matrix was a fast curing epoxy resin. The authors investigated the effect of the SMC flow on the unidirectional fiber architecture and showed that the composite stiffness followed a simple rule of mixtures. However, when the unidirectional fibers were oriented transverse to the SMC flow direction, the stiffness of the specimens was lower and showed higher variability compared to specimens where fibers were aligned in flow direction due to fiber rotation and transverse shearing of the unidirectional plies.

Evans (2018) investigated a hybrid material combining epoxy-based discontinuous carbon fiber molding compound and continuous carbon fiber patches. The discontinuous compound was manufactured in a direct fiber compounding process in which chopped fibers were depositioned while epoxy was applied simultaneously as a liquid resin spray. For the local reinforcement, carbon fiber textile was used, that was impregnated in the same manner. The author investigated tensile and bending properties of symmetric and asymmetric layups, interface properties between the continuous and discontinuous fibers and also performed drop weight impact and compression after impact tests. A second area of interest was the effect of different ply layups in the transition zone from the continuous plies to the discontinuous material on mechanical properties. Different ply step sizes and ply drop strategies were examined under axial loads.

Recently, Gan et al. (2019) presented a method to dry-align discontinuous carbon fiber tows between E-glass chopped strand mats or woven fabrics to manufacture hybrid composite plaques in an out-of-autoclave vacuum-assisted resin infusion process, using epoxy as the matrix. Tension tests on non-hybrid chopped carbon strand mats as well as hybrid materials with aligned and randomly oriented chopped fibers showed that an alignment resulted in enhanced stiffness and strength compared to the non-aligned hybrid. A comparison with the non-hybrid material showed enhanced stiffness of the aligned hybrid as well as a more ductile behavior due to subcritical damage mechanisms, in contrast to the catastrophic brittle failure of the non-hybrid composites.

Since 2015, the international research training group GRK 2078 "Integrated engineering of continuous-discontinuous long fiber-reinforced polymer structures" has been working on continuous-discontinuous SMC in terms of design, manufacturing, simulation and characterization to contribute to a fundamental understanding of the material system (Böhlke et al., 2016).

Within this scope, Bücheler and Henning (2016) investigated the influence of the matrix system and the position of the initial SMC charge on the position and alignment of continuous prepreg carbon fiber patches, that were co-molded together with discontinuous glass fiber SMC. The highly viscous B-stage of the UPPH resin (presented in Section 2.2.2) resulted in a strong flow resistance during compression molding and thus improved the position and alignment of the patch in the final plaque.

Followed by the investigation of Bücheler and Henning (2016), Trauth (2020) extensively studied UPPH-based continuous-discontinuous SMC and made significant contributions towards an understanding of structure-property relationships of hybrid composites by investigating microscopic aspects and macroscopic behavior at coupon, structure and component level. Besides studying mechanical properties, modeling approaches were discussed. The hybrid material's microstructure was characterized by means of µCT scans. Trauth and Weidenmann (2018) found a transition zone at the interface between the continuous and discontinuous plies that was characterized by split up fiber bundles. A similar, albeit less pronounced effect could be observed in the near-mold surface of discontinuous SMC, as was demonstrated for example by Le et al. (2008). Results from quasi-static tension and compression tests were also presented by Trauth and Weidenmann (2018). Compared to discontinuous SMC, the hybrid material showed a significant increase of 171 % and 151 % in tensile and compressive moduli of elasticity, respectively, and an increase of 204 % in tensile strength. The damage behavior was clearly dominated by the continuous plies. Damage evolution was characterized by progressive failure of the continuous carbon fibers starting from the specimen edges, followed by interlaminar delamination and final failure of the discontinuous ply due to extensive pseudo-delamination and fiber pull-out. Effects of hybridization were even more pronounced under bending load. Flexural stiffness of the hybrid SMC

increased by 370 % and flexural strength by 101 % compared to the discontinuous reference material (Trauth, 2020). Effects of hybridization were also demonstrated on component level (Trauth et al., 2018). Four-point bending tests were carried out on a discontinuous SMC component with and without local continuous carbon fiber reinforcement. An increase of mechanical properties resulting from the continuous reinforcement was demonstrated. Furthermore, puncture tests were carried out by Trauth et al. (2019). In these tests, hybridization was found to have a positive effect on the maximum force and energy, especially for quasi-static loading rates. Recently, Trauth et al. (2021) published results from a dynamic-mechanical-thermal analysis of UPPH-based continuous-discontinuous SMC. The glass transition temperature of the hybrid material was comparable to the glass transition temperature of discontinuous SMC. Comparing results of the hybrid with those of continuous carbon fiber SMC, the decrease of storage modulus was shifted towards higher temperatures and damping was significantly increased.

2.3 Fatigue behavior of fiber-reinforced polymers

2.3.1 General aspects

Fatigue of FRP composites presents an enormous challenge, given the number and variety of parameters that can potentially affect the underlying mechanisms. Even though FRP composites are well rated in terms of their fatigue properties, the onset of damage at an early stage of service life leads to a gradual reduction in mechanical properties (Degrieck and van Paepegem, 2001). The failure criterion of a composite component needs not necessarily be defined by a complete loss of its load-bearing capacity. A certain degree of stiffness loss, for example, might also be critical for certain applications. Lack of knowledge regarding the damage mechanisms under cyclic loading and their influence on the degradation behavior of FRPs usually results in large safety factors. Consequently, composite structures

are often overdesigned and extensive prototype testing is performed to provide a reliable service lifetime prediction. Better understanding of the damage behavior and development of accurate lifetime prediction models are crucial for a more economic use of FRP composites.

According to Ehrenstein (2006), analyzing the fatigue behavior of FRP composites ideally includes the definition of macroscopic strength-fatigue criteria (S-N curves), the characterization of the degradation behavior of stiffness and residual strength and the determination of the actual damage mechanisms and damage evolution. Determination of S-N curves is relatively easy to implement by loading different specimens of a distinct material with different constant amplitudes and determining the number of cycles to evoke ultimate failure. The experimental effort is increased if the failure criterion is not defined by a complete loss of load-bearing capacity of the specimen, but, for example, by a certain permissible decrease in stiffness or strength.

To determine a residual strength curve for an individual stress level, several specimens have to be fatigued at the considered constant stress amplitude, until cyclic loading is interrupted after different predefined numbers of cycles. The residual strength can then be determined in a subsequent tensile test for each specimen. If different stress levels are to be considered, the experimental effort grows considerably large.

Stiffness degradation can be determined non-destructively during the fatigue test. The determination of stiffness degradation curves requires a suitable strain measurement system (e.g. a clip-on extensometer) and the definition of a stiffness parameter. The stiffness of a material is usually described by the Young's Modulus. According to DIN EN ISO 527-1, the Young's Modulus is determined by

$$E = \frac{\sigma_2 - \sigma_1}{\varepsilon_2 - \varepsilon_1} \tag{2.1}$$

with σ_1 being the stress in MPa at $\varepsilon_1 = 0.0005\,(0.05\,\%)$ and σ_2 being the stress in MPa at $\varepsilon_2 = 0.0025\,(0.25\,\%)$. In tension-tension fatigue tests that are carried out at stress ratios other than R = 0, the material's strain response might be outside the defined region, which prevents a continuous measurement of Young's Modulus. Other parameters that are more suitable for fatigue testing are the dynamic stiffness used for example by O'Brien and Reifsnider (1981), that corresponds to the secant modulus of the hysteresis loop and is defined by

$$E_{\text{dyn}}(N) = \frac{\sigma_{\text{max}}(N) - \sigma_{\text{min}}(N)}{\varepsilon_{\text{max}}(N) - \varepsilon_{\text{min}}(N)} \tag{2.2}$$

or the fatigue modulus

$$E_{\text{fat}}(N) = \frac{\sigma_{\text{max}}(N)}{\varepsilon_{\text{max}}(N)} \tag{2.3}$$

defined by Hwang and Han (1986). Methods for determining underlying damage mechanisms and monitoring damage evolution under fatigue loading are presented in Section 2.4.

2.3.2 Fatigue of continuous FRP composites

2.3.2.1 Unidirectional FRP composites

The key damage mechanisms in unidirectional FRP laminae under tension-tension fatigue load are fiber-matrix debond growth and fiber fracture, whereas the latter is the most important one under on-axis loading (Talreja, 1981). Fiber fatigue might also influence the mechanical response of a composite. Fiber fracture occurs due to local stresses, caused for example by an externally applied load, that exceeds the local strength of the weakest fiber. During the first cycles of a fatigue

test, fiber fractures occur randomly distributed within the specimen volume. The energy released by a fiber fracture is dissipated by fiber-matrix debonding, matrix cracking and a plastic deformation of the matrix (Nairn, 1997; Laws and Dvorak, 1987). Further cyclic loading leads to a propagation of the debond. The crack tips of debonds and matrix cracks cause local stress concentrations that induce further fiber fracture close to the already broken fibers (Sørensen and Goutianos, 2019). Consequently, several fiber fracture clusters are formed and ultimate failure occurs due to unstable growth of one fiber fracture cluster (Gamstedt, 2000).

Kawai and Yano (2016), Taheri-Behrooz et al. (2010) and Chen and Hwang (2006) presented experimentally determined normalized S-N data of different unidirectional carbon/epoxy FRP composites that are shown in Figure 2.9. The properties of the fibers used by the different authors are listed in Table 2.4 together with the corresponding nominal fiber weight fractions. The S-N data differed significantly due to the use of different fibers, different fiber volume fractions and possibly different fiber-matrix interface properties. However, fatigue strength at approximately 10^6 cycles was between roughly 50 % to 65 % of the corresponding ultimate tensile strength.

Table 2.4: Properties of the carbon fibers used by Kawai and Yano (2016), Taheri-Behrooz et al. (2010) and Chen and Hwang (2006).

	Kawai and Yano (2016)	Taheri-Behrooz et al. (2010)	Chen and Hwang (2006)
Fiber type	T800H	T700	T700
Fiber content	64 wt.-%	48-51 wt.-%	66 wt.-%
Tensile strength	5490 MPa	4900 MPa	4900 MPa
Tensile modulus	294 GPa	230 GPa	230 GPa
Elongation at break	1.9 %	2.1 %	2.1 %

Several authors studied the fatigue behavior of unidirectional FRPs by means of S-N curve-based models (Kawai and Yano, 2016) or micromechanics-based models that consider the propagation of the different fatigue damage modes (Sørensen

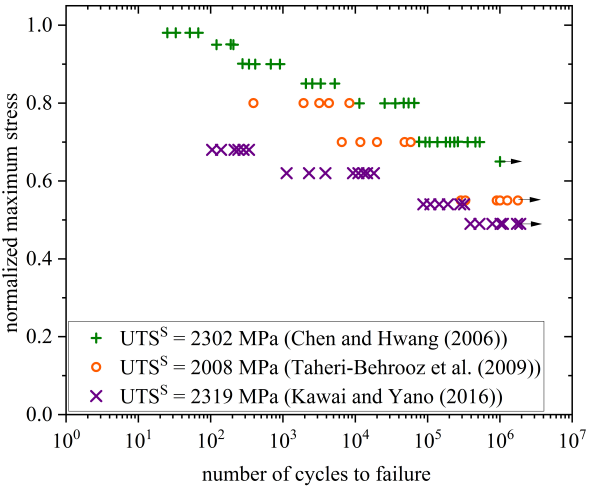

Figure 2.9: S-N data of different unidirectional carbon/epoxy composites obtained from tension-tension fatigue tests (R = 0.1).

and Goutianos, 2019; Alves and Pimenta, 2018; Fazlali et al., 2021). But even when accounting for all key damage mechanisms, it is still proven difficult to accurately predict the material behavior characterized in experiments. One reason might be the complex stress state near the clamps and the fact that there are still uncertainties in terms of the fatigue behavior of single fibers as well as in the input data for the debond growth rate (Fazlali et al., 2021).

2.3.2.2 Cross-ply laminates

Early studies on the fatigue behavior of cross-ply laminates presented in this section were conducted by O'Brien and Reifsnider (1981), Highsmith and Reifsnider (1982), Reifsnider et al. (1983), Talreja (1985) and Schulte (1987).

Reifsnider et al. (1983) discussed the mechanics of composite laminates under tension-tension fatigue loading and distinguished three stages in the stiffness degradation curve, as shown in Figure 2.10. In stage I, a rapid stiffness decrease is

observed. Stage II is characterized by an approximately linear stiffness decrease, whereas the degradation rate increases again in stage III before final failure.

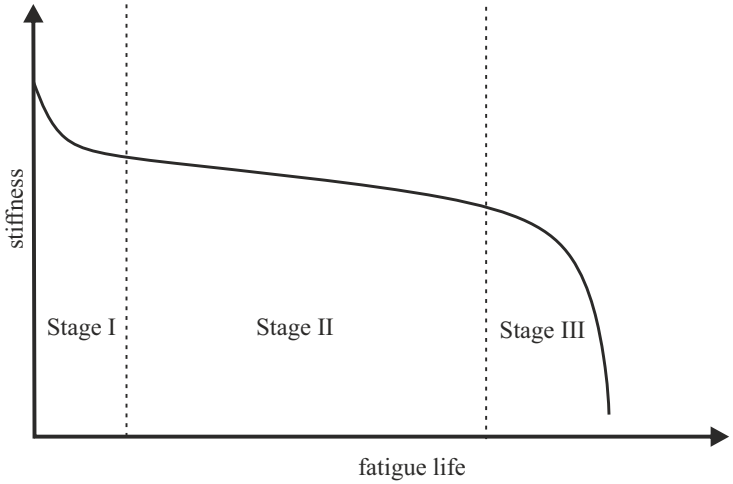

Figure 2.10: Characteristic degradation behavior of FRP according to Schulte and Stinchcomb (1984).

The damage mechanisms leading to stiffness degradation in a cross-ply laminate are presented in Figure 2.11 (Schulte, 1987). The occurrence and interaction of these mechanisms is strongly dependent on geometrical factors, such as stacking sequence, specimen size and the presence of notches, the type of fibers and matrix, as well as their respective fiber volume fractions, environmental factors such as temperature and the surrounding media and finally the type of loading (Schulte and Baron, 1989).

During the initial loading cycles of a tension-tension fatigue test, the initiation and growth of multiple transverse cracks in off-axis plies results in an initial decrease of stiffness in stage I. Crack growth is usually unstable due to the brittle behavior of the matrix. The cracks grow immediately through the ply thickness and arrest at adjacent plies. Depending on the fiber orientation, these cracks may also grow unstably through the full width of the laminate (often observed in 90° plies) or they might not grow across the whole width at all. The load at which first

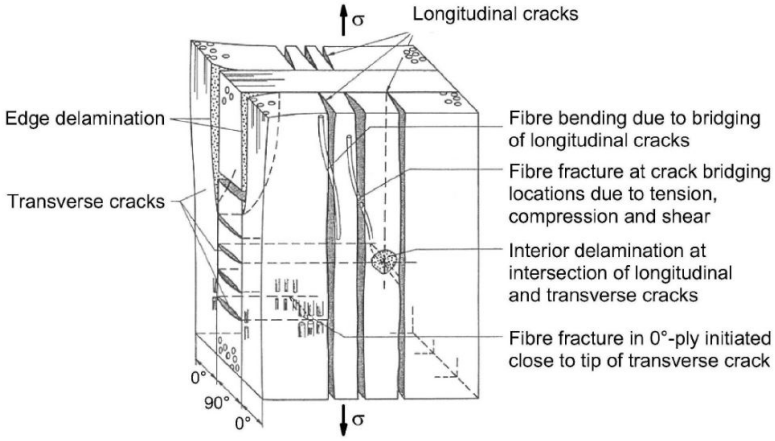

Figure 2.11: Damage mechanisms in a cross-ply laminate according to Schulte (1987).

ply cracks develop strongly depends on the laminate configuration, such as the orientation, thickness and sequence of plies (Talreja and Singh, 2012). Garrett and Bailey (1977) have shown that the thinner the constrained plies are, the greater the constraining effect due to an adjacent uncracked ply and consequently the higher the strain to initiate a transverse crack was. Conversely, the constraining effect decreases for a comparatively thick constrained ply. Further cyclic loading leads to the formation of new cracks between already existing ones. They usually occur at regular intervals, which decrease as the number of cycles increases. This process continues until a crack density is reached at which the distance between two adjacent cracks is so small, that the tensile stresses in between are no longer high enough to form new cracks. This state of saturated crack density is called characteristic damage state (CDS). Stage II is dominated by the formation of longitudinal cracks in the 0° plies and interlaminar cracks between the differently oriented plies. The formation of longitudinal cracks is caused by tensile stresses perpendicular to the loading axis due to the large Poisson mismatch between the differently oriented plies. Interlaminar cracks are typically observed at the specimen edges or at the intersection point of transverse cracks

in one ply and longitudinal cracks in the adjacent ply. In stage III, these small and isolated interlaminar cracks merge and form large delaminations, resulting in localized loss of integrity. Further damage develops locally and is characterized by extensive fiber fracture. The coalescence of locally damaged regions leads to a significant reduction of the load-bearing cross-section and eventually to ultimate failure. stage III involves only a small number of cycles. The onset of stage III is highly stochastic by nature and thus difficult to predict.

2.3.3 Fatigue of discontinuous SMC composites

Investigations on the fatigue behavior of discontinuous glass fiber-reinforced thermosets date back to the early 1970s. Howe and Owen (1972) presented a cumulative damage study on chopped strand mat/polyester resin laminates, in which the interaction of fatigue and creep loading as well as the effect of fatigue and creep damage on the residual tensile strength was investigated. Accompanying microscopic examinations indicated a correlation between resin cracking during fatigue and a reduction of static tensile strength, while fiber-matrix debonding did not diminish the static strength. Resin cracking was more pronounced under fatigue than under monotonic tension load. Owen and Howe (1972) quantified matrix cracks and transverse fiber debonding by examining the polished specimen edges. Damage was found to be dependent on the individual microstructure, but a normalized representation of the amount of matrix cracks and debonded fibers led to a single, non-linear curve. Crack density and stiffness loss showed a common trend, which supported the theory that transverse fiber debonding does not directly affect the strength. However, the debonds propagated into matrix cracks which led to further loss of strength.

Heimbuch and Sanders (1978) investigated static, fatigue, impact and long-term static properties of polyester- and epoxy-based SMC with varying glass fiber content. For the epoxy-based SMC with 57 wt.-% fibers, tensile strength was approximately 160 MPa and tensile fatigue strength at 10^6 cycles was 68 MPa, which is approximately 42 % UTS^S. Fatigue strength of polyester-based SMC as

a percent UTS^S was 50 % and 35 % for fiber contents of 25 wt.-% and 65 wt.-%, respectively. Corresponding values were slightly lower under bending fatigue load. Runout specimens showed a considerable loss of residual strength. Stiffness was measured during fatigue testing of polyester-based SMC with 25 wt.-% fibers, showing a decay of more than 25 % before separation of the specimen. Creep strain during fatigue loading was also determined. The amount of creep increased with enhanced load and temperature. Creep strain typically did not exceed 0.2 % for the considered materials, stresses and temperatures.

Denton (1979) characterized the tension-tension fatigue behavior of a polyester-based SMC with a fiber content of 50 wt.-% and 16 wt.-% calcium carbonate. An apparent fatigue limit was detected at 39 % UTS^S, which corresponds to the stress at which specimens withstood 10^7 cycles. Nevertheless, a decrease in residual strength of 16 % on average was measured for the corresponding specimens after cyclic loading. Furthermore, tensile stiffness decreased with increasing numbers of cycles, even when tested at stresses that corresponded only to 15% to 20 % UTS^S.

Mandell and Meier (1983) studied glass fiber-reinforced SMC composites with fiber weight fractions of 25 % (SMC R25) and 50 % (SMC R50). For SMC R25, the major damage mechanism was matrix cracking perpendicular to loading direction. For SMC R50, damage was mainly characterized by interface debonding between matrix and bundles. The authors measured crack densities by counting the number of cracks crossing a line from top to bottom of a predefined length. Crack density was subject to large scatter throughout all stress ranges. No correlation between crack density and fatigue life was observed. The density of matrix cracks at ultimate failure was independent of the load history. Mandell and Meier (1983) determined S-N curves with a slope of approximately 10 % of the single-cycle ultimate tensile strength per decade of cycles.

Wang and Chim (1983) investigated fatigue-induced stiffness degradation in randomly oriented short (25.4 mm) glass fiber polyester composites. Cyclic loading caused crack initiation and growth resulting in a reduction of stiffness and a change in the shape of the hysteresis loops. Microcracking in the form of matrix cracks,

fiber-matrix interface debonding and fiberend-cracks were the dominating damage mechanisms. The planes of the microcracks were oriented normal to the loading direction in matrix-dominant areas as well as in fiber-dominant areas, where fibers were oriented in parallel to the loading direction. In the latter case, smaller crack lengths were observed. In fiber bundles oriented with an angle to the loading direction, microcracks were observed to grow along the interface between fiber and matrix. The damage mechanisms observed in SMC with 50 wt.-% fibers tested at 60 % UTS^S are shown in Figure 2.12. Wang and Chim (1983) reported, that the overall crack density was higher, with the average crack length being smaller in specimens tested at higher stresses compared to specimens tested at lower stresses. At a given stress level, the magnitude of stiffness degradation increased with the number of cycles due to continuous initiation and growth of cracks. Increasing stress also led to a significant increase in the magnitude and the rate of stiffness reduction. For example, at a cyclic stress of 70 % UTS^S, a 20 % stiffness reduction was determined prior to failure.

Wang et al. (1986) analyzed the cyclic fatigue degradation and associated damage-induced anisotropy of elastic properties through the development of probabilistic density functions of microcrack length and orientation. While the mechanical properties of the pristine randomly oriented SMC composite could be considered as macroscopically isotropic, the preferred orientation of microcracks led to anisotropic degradation of elastic properties (Figure 2.13). Stiffness degradation rates decreased exponentially with fatigue loading due to rapid depletion of crack initiation, slow growth of microcracks and several crack-arrest mechanisms. Magnitudes and rates of the change in stiffness were significantly higher in loading direction compared to the transverse direction.

Von Bernstorff (1989) explained in detail the damage evolution in SMC under cyclic loading and distinguished between fatigue at loads above and below the knee point. For cyclic tensile loads below the knee point, no or very few microcracks developed. Therefore, no significant loss of stiffness was observed up to a high number of cycles, with the hysteresis loop remaining almost linear and its slope equal to the Young's Modulus. Viscoelastic effects led to a horizontal shift of the hysteresis loop without significant reduction of the slope. When loaded above

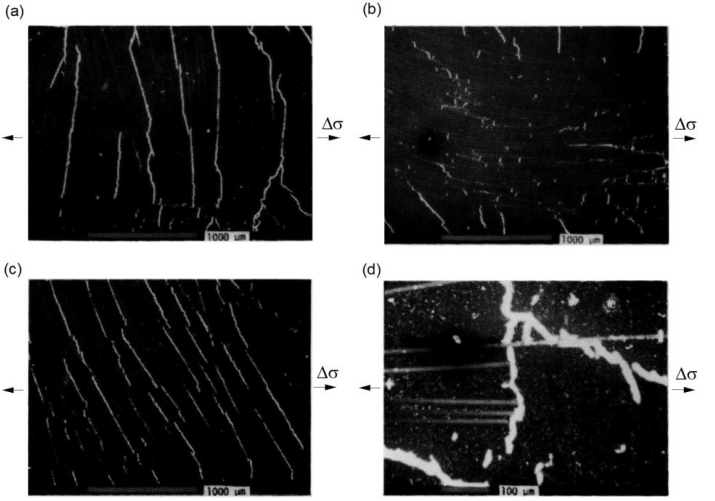

Figure 2.12: Scanning electron micrographs of microcracks in (a) a matrix-dominated area with sparsely dispersed fibers, (b) a fiber-dominated area with fibers parallel to the loading direction, (c) an area with fibers oriented at an angle to the loading direction and (d) at fiber ends (modified from Wang et al. (1986)).

the knee point, multiple cracks initiated in the specimens within the first few cycles. The number of cracks increased with the number of cycles. When the smallest possible crack spacing was reached, fiber-matrix debonds occurred at the corresponding crack tips. The difference in stiffness between the bundles and the matrix, resulting in alternating mode II shear stress, caused further debonding. The same mechanism is responsible for delamination in unidirectional laminates. The larger the area of delamination, the smaller the fraction of the load that the fiber bundle could support and the higher the stresses in the rest of the material. This leads to further multiple cracking in thinner matrix regions with smaller crack spacing. This multiple cracking is responsible for a decrease of stiffness, resulting in a decreasing slope of the hysteresis loops. According to von Bernstorff (1989), a CDS, which is common in cross-ply laminates, can also be observed for SMC. In this case, crack spacing was larger in matrix-rich regions, where the distance between adjacent fibers was large and smaller in fiber-rich regions,

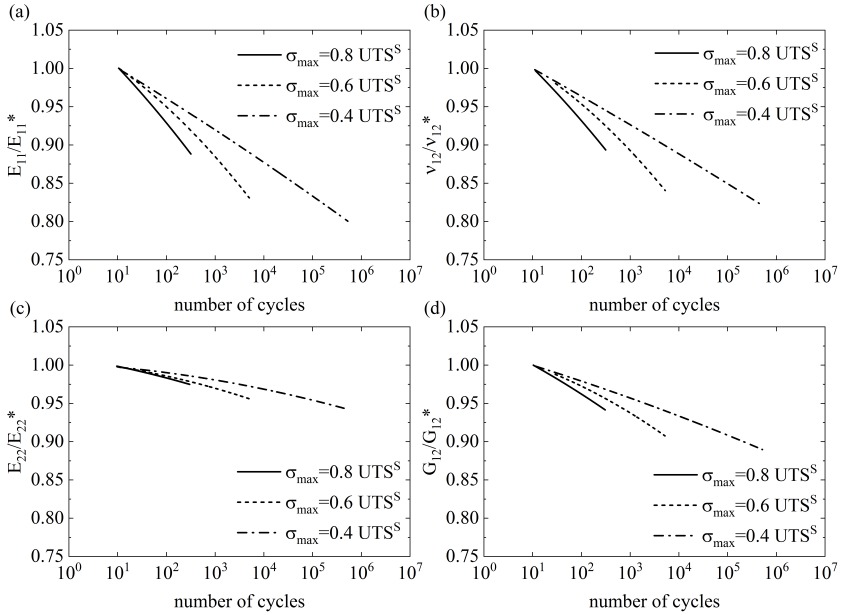

Figure 2.13: Evolution of elastic properties in SMC with 50 % by weight fibers during cyclic loading at R = 0.05 and f = 2 Hz at different stress levels (according to Wang et al. (1986)).

where the distance between adjacent fibers was small. Von Bernstorff (1989) also noted, that the CDS is unique to a particular microstructure. This means that a specimen, that failed due to fatigue, features the same crack density as a specimen with identical microstructure, that has been monotonically loaded to ultimate failure. However, Wang and Chim (1983) noted, that the crack density depends on the loading history.

2.3.4 Influence of frequency and temperature

Polymers with and without fiber reinforcement show a viscoelastic, meaning a time- and temperature-dependent behavior, even below the glass transition temperature. In automotive applications, components are exposed to cyclic loads

that vary in amplitude and frequency at temperatures between approximately -40 °C and 80 °C. The influence of these parameters on the fatigue properties is therefore of high interest.

2.3.4.1 Temperature-dependent fatigue behavior of continuous FRP composites

In a study by Miyano et al. (1994), the flexural fatigue behavior of a satin woven CFRP based on an epoxy resin with a high glass transition temperature of 236 °C was investigated. Fatigue tests were carried out at 50 °C, 150 °C and 230 °C at frequencies of 2 Hz and 0.02 Hz, respectively. Flexural fatigue strength decreased with increasing temperature. According to Miyano et al. (1994), temperature dependence (and frequency dependence) was more pronounced at higher temperatures. However, the slope of the S-N curve remained the same throughout the whole temperature range.

Miyano et al. (1999) investigated the fatigue behavior of unidirectional CFRPs made from high-strength carbon fibers (TORAY T400-3K) and epoxy resin (EPIKOTE 828) with a glass transition temperature of 112 °C. Fatigue tests were carried out in at temperature ranging between 50 °C and 150 °C. Specimens tested at a frequency of 2 Hz and a load ratio of 0.1 showed a reduced fatigue strength at a temperature of 110 °C (or higher) compared to specimens tested at 50 °C. However, this temperature was already close to the material's glass transition temperature.

Kawai et al. (2001) analyzed the off-axis fatigue behavior of unidirectional carbon fiber-reinforced epoxy at room temperature and at 100 °C. For off-axis angles between 10° and 90°, fatigue strength at 100 °C was reduced to one-half to two-thirds of the fatigue strength at room temperature, while no significant effect of temperature was observed in the fiber direction (0°).

A study by Shimokawa et al. (2008) on the fatigue behavior of carbon fiber-reinforced bismaleimide with a quasi-isotropic stacking sequence at room temperature and 150 °C showed that temperature had a minor effect on the S-N curve, due to the fiber dominated material behavior.

Montesano et al. (2012), who studied the fatigue behavior of off-axis satin-woven carbon/bismaleimide, observed a strong influence of temperature on stiffness degradation, strain ratcheting and energy dissipation, which was explained by the matrix-dominated material configuration.

A study by Sjogran (2002) on continuous carbon fiber-reinforced epoxy subjected to mode I, mode II and mixed-mode fatigue loading revealed that elevated temperatures accelerated delamination crack growth rates. Double cantilever beam, end-notch flexural and mixed-mode bending setups were investigated in the study. However, it could not be clarified whether this influence is the same in case of uniaxial cyclic loading.

From the results reported in the literature, it can be concluded that the effect of temperature on fatigue properties strongly depends on whether the material exhibits fiber-dominated or matrix-dominated behavior, i.e. on the fiber architecture and content.

2.3.4.2 Frequency-dependent fatigue behavior of continuous FRP composites

Mandell and Meier (1983) presented results from tension-tension fatigue tests on cross-ply E-glass/epoxy laminates at 1 Hz, 0.1 Hz and 0.01 Hz and observed that specimens tested at a higher frequency had higher fatigue lives. The effect was more pronounced in the low cycle fatigue range compared to the high cycle fatigue range. Linearized S-N curves had different slopes and an extrapolation of the curves showed convergence after approximately $6.2 \cdot 10^6$ cycles.

Barron et al. (2001) examined the effect of frequency on the fatigue behavior of a carbon fiber/epoxy matrix composites in different orientations. Tension-tension fatigue tests were carried out at 5 Hz, 10 Hz and 20 Hz. Cross-ply and angle-ply specimens showed a profound frequency dependence, while results for unidirectional specimens were inconclusive due to a large degree of scatter.

The fact, that no distinct frequency dependence of the unidirectional specimens was observed, is in agreement with the findings by Zhou et al. (2010), who carried out tensile tests on carbon fiber bundles and showed, that strain rate had a negligible effect on the ultimate tensile strength and failure strain. Since carbon fibers are known to be largely strain rate-insensitive, a frequency effect on the fatigue behavior was also not expected.

2.3.4.3 Temperature-dependent fatigue behavior of discontinuous SMC composites

Heimbuch and Sanders (1978) carried out fatigue tests on polyester-based SMC with fiber weight fractions of 25 wt.-% (SMC-25) and 65 wt.-% (SMC-65) at -40 °C, ambient temperature and 93 °C. For both material systems, no significant difference in the fatigue behavior at -40 °C and ambient temperature was observed. At 93 °C, the fatigue strength after 10^6 cycles was reduced by almost 30 % in the case of SMC-25 and by more than 50 % in the case of SMC-65, compared to the results obtained at ambient temperature.

Denton (1979), who carried out fatigue tests on polyester-based SMC with 50 wt.-% fibers at different temperatures found an apparent fatigue limit at 39 % and 31 % of the material's ultimate tensile strength at 23 °C and 93 °C, respectively, with the quasi-static ultimate tensile strength being measured at 23 °C. When expressed in percent of the ultimate tensile strength at the investigated temperature, the fatigue limit was 39 % for both cases. However, specimens subjected to stresses corresponding to their respective fatigue limit showed a smaller amount of stiffness degradation at 93 °C compared to those tested at 23 °C.

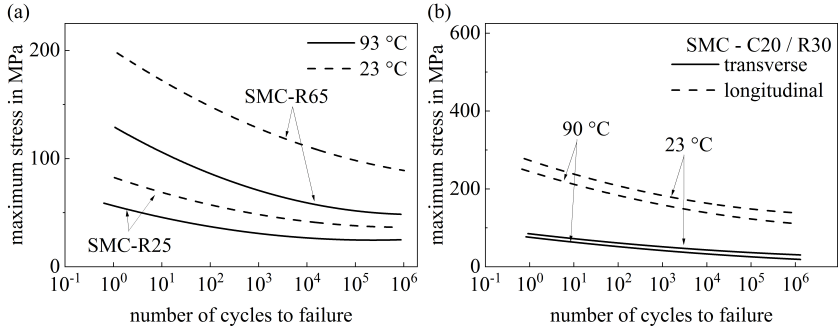

Figure 2.14: Temperature dependent S-N curves of (a) discontinuous SMC (randomly oriented) with fiber weight fractions of 25 wt.-% (SMC-R25) and 65 wt.-% (SMC-R65) and (b) continuous-discontinuous SMC with 20 wt.-% continuous fibers and 30 wt.-% randomly oriented discontinuous fibers (SMC-C20/R30) in transverse and longitudinal direction (data from Springer (1983)).

Springer (1983) investigated the fatigue behavior of polyester-based SMC with different reinforcement architectures (randomly oriented chopped glass fibers, continuous glass fibers and a combination of continuous and chopped fibers, whereas the arrangement of the reinforcement is not further described). Here, he summarized the effects of temperature and moisture on various engineering properties (quasi-static, fatigue and creep properties). In contrast to the observations made by Denton (1979), a high influence of temperature was determined for chopped fiber composites subjected to tension-tension loading. A temperature increase from 23 °C to 93 °C resulted in a reduction of maximum stress of approximately 30 % (70 MPa) and 50 % (40 MPa) in the low cycle and high cycle fatigue range, respectively, for a fiber content of 65 wt.-%. A reduction of approximately 30 % (up to 25 MPa in the low cycle fatigue range and 12 MPa to 15 MPa for the high cycle fatigue range) was observed for a fiber weight content of 25 %, as depicted in Figure 2.14. Springer (1983) described the reduction of fatigue strength to be less pronounced in the case of a combined continuous and discontinuous reinforcement. However, absolute difference between corresponding experiments

at 23 °C and 90 °C was not negligible, especially for specimens tested in longitudinal direction, with 25 MPa (reduction of 10 % for low cycle fatigue and up to 20 % for high cycle fatigue), as shown in Figure 2.14.

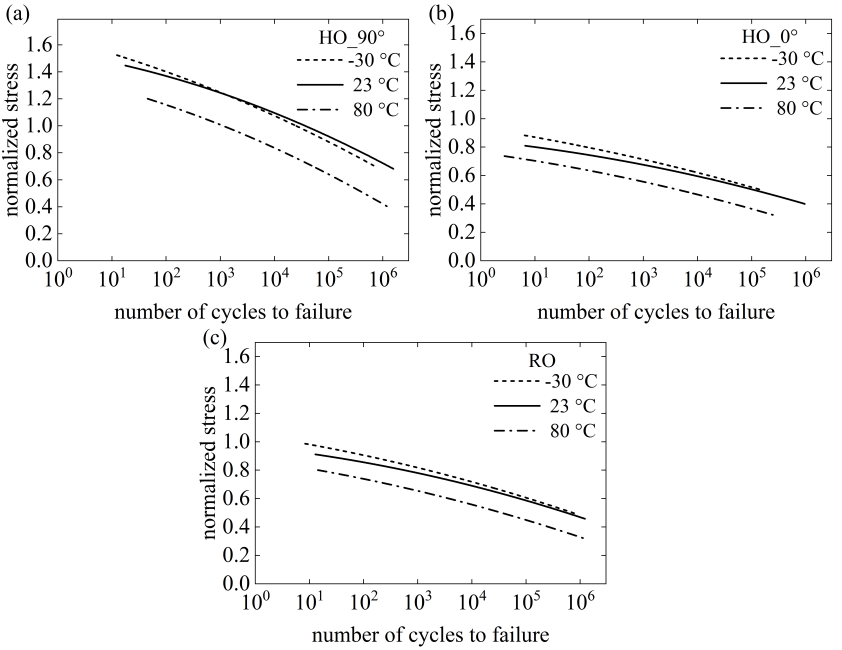

Figure 2.15: Temperature dependent S-N curves of (a) highly oriented SMC in longitudinal direction (HO_0°), (b) highly oriented SMC in transverse direction (HO_90°) and (c) randomly oriented SMC (RO) (data from Tamboura et al. (2020)).

Further investigations on SMC submitted to variable temperature loading were presented by Tamboura et al. (2020). The material system was a polyester resin reinforced by 28 wt.-% chopped glass fiber bundles and 37 wt.-% $CaCO_3$ filler. A quasi-isotropic configuration as well as a configuration with highly oriented fiber bundles were examined. A temperature increase from 23 °C to 80 °C led to a decrease of fatigue strength. In the case of randomly oriented fiber reinforcement, fatigue strength decreased by approximately 11 % and 13 % of the

material's ultimate strength in the low cycle and high cycle fatigue range, respectively. Comparable results were obtained for SMC with highly oriented fibers. At temperatures of -30 °C, fatigue life slightly increased in the low-cycle fatigue range, while no clear trend was observed in the high-cycle fatigue range.

2.3.4.4 Frequency-dependent fatigue behavior of discontinuous SMC composites

Most studies published on the effect of frequency on the fatigue behavior of discontinuous FRPs where carried out on thermoplastic-based composites. In those composites, induced thermal fatigue led to softening of the matrix and hence to a reduced fatigue resistance at high frequencies (Bellenger et al., 2006; Handa et al., 1999).

To the authors knowledge, the first and only study on the frequency dependence of SMC was presented by Shirinbayan et al. (2017), who investigated the fatigue behavior of a vinyl ester-based discontinuous glass fiber SMC at 10 Hz, 30 Hz, 50 Hz and 100 Hz. For low stresses, the difference in fatigue life of specimens loaded at 10 Hz, 30 Hz and 50 Hz was small, as depicted in Figure 2.16. For high stresses, the S-N curve was shifted to lower fatigue lives with increasing frequency. At 100 Hz, a frequency effect was observed even for low stresses. At 40 % UTS^S, fatigue life was 40 times lower compared to the fatigue life of specimens tested at frequencies of 50 Hz and below. This behavior was explained by self-heating and resulting induced thermal fatigue.

2.4 Experimental methods for fatigue damage analysis

Various methods have been used by different researchers to investigate the damage mechanisms and damage evolution in FRPs under cyclic loading. All of these methods have their advantages and disadvantages. Which method or combination

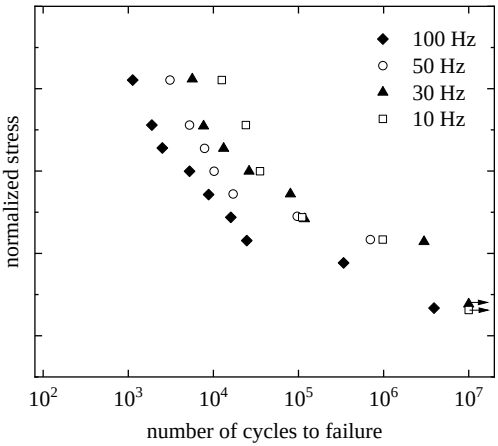

Figure 2.16: Normalized S-N data of randomly oriented discontinuous SMC at different frequencies (Shirinbayan et al., 2017).

of methods is most promising, depends on the material system and the objectives of the investigation.

One experimental method is a visual inspection that can optionally be supported by a back-light system or a light source in front of the specimens. This method can be used, for example, for manual or automatic crack detection, as described in several studies of the Quaresimin group (Quaresimin et al., 2014; Maragoni et al., 2017). The method is non-destructive, cheap and fast, requires no specimen preparation and is trustable, since no futher interpretation of the results is needed. However, it is limited in terms of scale and can only be used for materials that are transparent to light.

Optical microscopy is also a quick, versatile and reliable method that is cost-effective and is therefore used by many researchers, e.g. Quaresimin et al. (2016). However, the analysis of damage is limited to the specimens' surface and requires careful specimen preparation. It is further limited in depth of field and can thus be used only when having a flat surface, which does not apply for fracture surfaces. When using optical microscopy for monitoring damage evolution during fatigue

loading, specimens usually have to be unclamped after several load intervals to further be analyzed. This can be avoided by using edge replication techniques, as for example presented by Chen and Harris (1993), who characterized the evolution of ply cracks in carbon fiber-reinforced laminates during fatigue loading or by Montesano (2012), who analyzed the damage evolution in braided FRPs.

In contrast, scanning electron microscopy is high in depth of field and can provide information on topography and composition. It is often used for analysis of fracture surfaces, as for example by Trauth (2020), but also allows for in-situ testing. However, this method is destructive, cost-intensive and only a small specimen volume can be investigated. Furthermore, only the surface and not the entire specimen volume can be analyzed.

Digital image correlation (DIC) offers the possibility to investigate damage in small specimens as well as in large components and gives information on the full strain field. However, the method is time- and cost-intensive, since it requires careful calibration and setup, as well as specimen preparation. Furthermore, software is needed to extract and interpret the data. Data is only collected at the surface ply, while little information is obtained for the rest of the specimen volume, at least when thinking of local damage events such as cracks. Miskdjian et al. (2020) used DIC to automatically detect ply cracks in GFRP laminates at the specimen edges. Li et al. (2020), who also used DIC to observe ply cracks in cross-ply laminates showed, that they can even be identified when looking at the 0° surface ply of the specimen. A successful application of DIC to detect delamination was presented, for example, by Szebényi and Hliva (2019).

Using infrared (IR) thermography, damage events can be determined even below the specimen surface without the material being transparent to visible light. Montesano et al. (2014) used this method to characterize damage in braided carbon fiber-reinforced composites, for example. However, a disadvantage is that damage events occurring further away from the surface are harder to detect. Depending on the required resolution of the camera, the method can be quite cost-intensive and know-how and experience are required to interpret the measured data. Small

damage events such as matrix cracks are harder to detect than fiber damage and interface failure, since they dissipate less thermal energy (Munoz et al., 2016).

In comparison to DIC and IR thermography, acoustic emission (AE) analysis allows the detection of very small damage events, such as matrix cracking and single fiber fracture, in the bulk material, making this technique very promising for monitoring the initiation and progression of different damage mechanisms. Intensive research was done to allow for the interpretation of AE signal by analyzing different AE features using clustering algorithms, for example by Sause et al. (2012). Damage events can be detected in the bulk material and there are no particular requirements regarding the material or its preparation. The method is very sensitive and can be used both for small specimens and large structures. Saeedifar and Zarouchas (2020) recently published a review, highlighting the potentials of AE analysis for damage characterization in composites. Besides the problem of noise, that can be challenging for some applications, it requires great skill and a lot of pre-investigations to interpret the data. In materials, in which a lot of different damage events occur at the same time, as for example in SMC, it is difficult to distinguish between damage mechanisms. Potstada et al. (2018) identified characteristics of single-fiber fracture by combining AE analysis with synchrotron computed analysis, so that those can clearly be identified during testing. Other researchers evoked single mechanisms in a targeted manner, for example by testing pure resin specimens or fiber bundles, to obtain the corresponding AE signals separately and using them as a reference, as for example done by Mohammadi et al. (2017). Trauth et al. (2017b) used AE analysis to monitor damage in discontinuous and continuous-discontinuous SMC specimens and applied a clustering algorithm to the obtained data. Despite the two clusters assigned to fiber and matrix damage observed in discontinuous SMC (Trauth et al., 2017a), a third cluster was determined for continuous-discontinuous SMC specimens. Based on post-mortem µCT scans, this cluster was assigned to delamination that occurred in the hybrid material only. Bartkowiak et al. (2019), presented an attempt to reliably distinguish between fiber fracture, matrix cracking and interface damage in discontinuous SMC specimens subject to monotonic tensile load by combining AE analysis with in-situ µCT measurements. The combination of both methods

allowed to distinguish between the peak maximum frequencies of the different signals resulting from fiber fracture and matrix cracks. However, there is still the need for further investigations to analyze the different AE features resulting from different damage events.

Ultrasound can also be used for a damage analysis, but is rather useful for the determination of large scale damage such delamination and therefore is often applied to analyze impact damage. Detection of matrix cracks is difficult but possible as for example shown in Aymerich and Meili (2000) for continuous FRPs and in Aymerich and Meili (1999) for SMC.

Another method for damage analysis in FRPs, that is of increasing interest within the past few years, is µCT X-ray tomography, which has the advantage of providing a 3D representation of the scanned volume. Different magnifications and resolutions can be realized. The method is quite cost-intensive and requires extensive image manipulation and analysis. Nevertheless, it offers high potential for an accurate and quantitative analysis of the damage processes in FRPs, since it also offers the possibility for in-situ measurements. Schöttl et al. (2020) reported results from cyclic in-situ tests on discontinuous SMC specimens together with a method for crack segmentation and determined fiber volume fractions. A method enabling the analysis of the spatial crack orientation distribution to further quantify the damage anisotropy is presented in Schöttl et al. (2021).

2.5 Lifetime prediction modeling of FRP composites

A comprehensive review of fatigue damage models for FRP composites was presented by Degrieck and van Paepegem (2001). The authors classified existing fatigue models into three major categories:

- empirical fatigue life models,
- phenomenological models for residual stiffness or residual strength and

- progressive damage models.

Empirical fatigue life models use S-N curves or Goodman-type diagrams and introduce a fatigue failure criterion without considering damage accumulation and underlying damage mechanisms. Fatigue life is determined for fixed loading conditions. Depending on the number of parameters to be considered, the experimental effort is very high.

Phenomenological models express the degradation of mechanical properties mathematically, without considering the underlying mechanisms. Residual strength models have the major disadvantage that extensive destructive testing is required to calibrate the model. In contrast, stiffness degradation models have the advantage that stiffness can be determined non-destructively during testing. One of the major causes of stiffness degradation in FRPs is matrix cracking. This type of progressive damage suggests the use of a continuum damage model to describe the material behavior (van Paepegem, 2010), which is why the vast majority of the phenomenological residual stiffness models are based on the continuum damage mechanics theory (Kachanov, 1990). To describe damage in a quantitative manner, a damage variable D was introduced, which describes the effective surface density of defects and hence takes the value 0 in the case of an undamaged material and 1 in the case of a completely damaged material. Hence, D can be described by

$$D = \frac{A_D}{A_0}, \tag{2.4}$$

with A_D being the damaged specimen area and A_0 being the initial area. Applying the concept of strain equivalence, which states that a damaged volume of material loaded at a stress σ shows the same strain response as a similar undamaged volume loaded with a comparative stress $\tilde{\sigma}$ (Krajcinovic and Lemaitre, 1987) leads to

$$\varepsilon = \frac{\tilde{\sigma}}{E_0} = \frac{\sigma}{E_0(1-D)} \tag{2.5}$$

such that D, defined as

$$D = 1 - \frac{E}{E_0} \tag{2.6}$$

becomes a measure for the stiffness degradation.

An important outcome of a fatigue model is always the prediction of fatigue life. Residual strength models have a natural failure criterion, in a sense that failure occurs, when the applied stress equals the residual strength. Residual stiffness models assume that fatigue failure occurs, when the modulus has dropped to a critical level. This critical level has been defined differently by distinct researchers. According to Hahn and Kim (1976) and O'Brien and Reifsnider (1981), ultimate failure due to cyclic loading occurs, when the fatigue secant modulus drops to the secant modulus at the time of failure in a static test. According to Hwang and Han (1986), ultimate failure occurs when the resultant strain reaches ultimate strain in a static test. In any case, it is important to choose a criterion that is consistent with experimental results.

Progressive damage models rely on physics-based modeling of the damage mechanisms, that lead to a degradation of the mechanical properties. These models can be further subdivided into models that predict damage growth (e.g. the number of matrix cracks or the size of the delaminated area) and models that correlate damage evolution with mechanical property evolution. Progressive damage models are clearly the most promising tool for predicting fatigue life when well calibrated. A major hurdle in the development of these models is the complexity of the fatigue damage mechanisms in FRP composites, which first needs to be analyzed in detail.

2.6 Scientific questions

Several studies have been published on concepts to manufacture and design continuous-discontinuous FRP composites. Experimental investigations by different authors highlight the beneficial mechanical properties and potentials of such a hybrid approach. In most of the published studies, a focus was set on mechanical properties under quasi-static load. Since existing as well as potential applications for continuous-discontinuous FPR composites are subject to cyclic loading, their fatigue behavior is of high interest. Early investigations by Riegner and Sanders (1979), Kundrat et al. (1982) or Springer (1983) in the late 1970s and early 1980s considered fatigue loads in continuous-discontinuous SMC with glass fibers being used for both reinforcement types. Due to the low difference in failure strain of both components, effects of hybridization were not expected to be particularly pronounced, which was reflected in a moderate resistance to fatigue.

Trauth (2020) carried out extensive experimental investigations to characterize quasi-static properties of discontinuous glass fiber SMC with continuous carbon fiber reinforcement under tension, compression and bending loads. Static and dynamic puncture properties were also characterized (Trauth et al., 2019) and a dynamic-mechanical-thermal analysis was carried out (Trauth et al., 2021). The combination of continuous carbon fibers and discontinuous glass fibers resulted in pronounced hybridization effects. However, no investigations on the fatigue behavior of continuous-discontinuous SMC have been presented so far. The following questions have thus remained unanswered:

- Is the fatigue behavior of the individual UPPH-based composites comparable to conventional continuous and discontinuous FRP composites?
- What are the effects of hybridization on the fatigue properties of continuous-discontinuous SMC?

To gain a better understanding of the material behavior and effects of hybridization, it is necessary to understand the underlying damage mechanisms, their initiation and evolution. Trauth (2020) evaluated measurement techniques to find the most

suitable for capturing damage evolution in continuous-discontinuous SMC and performed corresponding analyses under quasi-static loading conditions. These techniques are not necessarily applicable to characterize damage evolution under cyclic loading. Several approaches to characterize fatigue damage in either discontinuous or continuous FRPs have been presented in literature. This thesis aims to address the following questions:

- What is a suitable experimental technique to qualitatively and quantitatively analyze damage evolution in continuous-discontinuous SMC under cyclic loading?
- How does hybridization influence the damage mechanisms and damage evolution of the discontinuous glass fiber and the continuous carbon fiber SMC ply?

Thinking of future applications of continuous-discontinuous SMC, part geometries and loading conditions become more complex. Multiaxial-stress states may motivate the use of continuous reinforcements other than a unidirectional 0° ply. Whether a 0°/90° reinforcement might be suitable will be clarified by answering the following questions:

- What effect does the choice of a 0°/90° instead of a unidirectional 0° carbon fiber reinforcement have on the damage evolution under cyclic loading and how does the changed damage evolution influence fatigue life and the stiffness degradation behavior?

Additional complexity of application-related load is further added by non-uniform oscillations and varying temperatures, which raises the question:

- To what extent do frequency and temperature influence the fatigue behavior of continuous-discontinuous SMC?

Different strategies for modeling the fatigue behavior of FRPs in general have been discussed in the literature. To use the hybrid composite in an efficient manner and to avoid large safety factors and extensive experimental investigations in the

future, the final goal must be the development of a lifetime prediction model for continuous-discontinuous SMC that can account for the varying geometries and loading conditions. As a first step to reach this goal, this thesis addresses the question:

- What are potential strategies for lifetime prediction modeling of continuous-discontinuous SMC?

Together with the already existing knowledge on the fatigue of continuous and discontinuous FRPs postulated by different scientists, on the mechanical behavior of continuous-discontinuous FRPs in general and together with the knowledge obtained from extensive investigations by Trauth (2020) on the mechanical properties and the damage evolution of the considered UPPH-based continuous-discontinuous SMC, the findings observed in experimental investigations within this thesis shall help to answer these questions.

3 Materials

3.1 Material composition

The materials examined in this thesis are sheet molding compounds (SMC) with either a continuous (Co) carbon fiber or a discontinuous (DiCo) glass fiber reinforcement, as well as hybrids combining both reinforcement types in two different configurations, that are shown in Figure 3.1. Details of the measured thicknesses of the individual plies are given in Section 3.3.

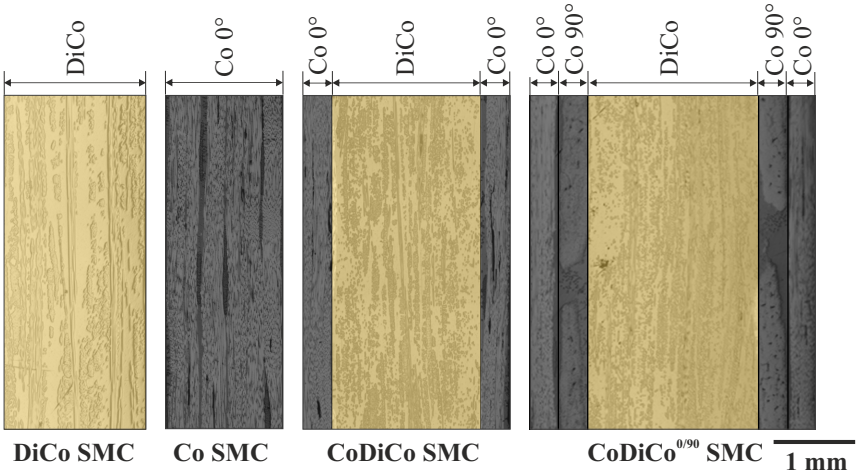

Figure 3.1: Material architectures, which were examined within this thesis.

The focus of this thesis is on hybrid composites with DiCo SMC in the core and one 0° Co SMC ply on each surface, that are henceforth referred to as continuous-discontinuous SMC (CoDiCo SMC) composites. A second configuration with a 0°/90° carbon fiber reinforcement was additionally analyzed under tension-tension fatigue load to investigate the effect of a deviating reinforcement type on damage mechanisms and fatigue life. Corresponding specimens are referred to as $CoDiCo^{0/90}$ SMC.

The matrix used for both types of reinforcement was an unsaturated polyesther-polyurethan hybrid (UPPH) resin system by Aliancys. This two-step curing resin system was developed at Fraunhofer Institute for Chemical Technology, Pfinztal, Germany, with the aim to obtain a material featuring a stable, highly viscous B-stage that is needed to achieve a stiff and shape-consistent reinforcement for a reliable co-molding process of continuous prepreg with DiCo SMC at high flow rates (Bücheler, 2018). The glass transition temperature of the fully cured material is between 155 °C and 160 °C (Kehrer, 2019). The discontinuous reinforcement was realized by E-glass fibers (Multistar 272 by Johns Manville) that are arranged in bundles of approximately 200 fibers and cut to a length of 25.4 mm during the manufacturing process of the semi-finished SMC. A stitch-bonded unidirectional carbon fiber fabric consisting of 5 mm wide ZOLTEK PX35 50K continuous tow carbon fiber was used for continuous reinforcement. The aligned carbon fiber tows are stitched together with a polyester yarn in a tricot pattern. The mechanical properties of the cured resin system and the fibers are listed in Table 3.1 The resin components and the fiber type of the discontinuous glass fiber SMC and the continuous carbon fiber SMC are listed in Table 3.2 and Table 3.3, respectively.

Table 3.1: Mechanical properties of the resin system (Trauth, 2020), the glass fibers (AZO, 2021) and the carbon fibers (Zoltek, 2017) used in this thesis.

Property	Resin system	Glass fiber	Carbon fiber
Tensile strength	75 MPa	2050 MPa	4137 MPa
Tensile modulus	3.45 GPa	85 GPa	242 GPa
Failure strain	3.0 %	2.8 %	1.7 %

Table 3.2: Resin components and fiber type of discontinuous glass fiber SMC.

Component	Product name	Supplier	Parts	Density	Reference
UPPH resin	Daron 41/B1	Aliancys	100	1.14 gcm^{-3}	DSM (2012)
Release agent	BYK 9085	BYK	2.0	0.92 gcm^{-3}	BYK (2012)
De-airing	BYK-A-530	BYK	0.5	0.81 gcm^{-3}	BYK (2016)
Inhibitor	pBQ	Fraunhofer ICT	0.3	1.32 gcm^{-3}	Sigma-Aldrich (2021a)
Peroxide	Trigonox 117	Akzonobel	1.0	0.95 gcm^{-3}	BASF (2019)
Thickener	Lupranat M20R	BASF	19.5	1.23 gcm^{-3}	BASF (2019)
Fiber	Multistar 272	Johns Manville	44.5 wt.-%	2.57 gcm^{-3}	AZO (2021)

Table 3.3: Resin components and fiber type of continuous carbon fiber SMC.

Component	Product name	Supplier	Parts	Density	Reference
UPPH resin	Daron 41/B1	Aliancys	100	1.14 gcm^{-3}	DSM (2012)
Release agent	BYK 9085	BYK	2.0	0.92 gcm^{-3}	BYK (2012)
Impregn. add.	BYK 9076	BYK	3.0	1.05 gcm^{-3}	BYK (2014)
Inhibitor	pBQ	Fraunhofer ICT	0.3	1.32 gcm^{-3}	Sigma-Aldrich (2021a)
Styrene	Mono Styrol	BASF	2.9	0.91 gcm^{-3}	Sigma-Aldrich (2021b)
Peroxide	Trigonox 117	Akzonobel	1.0	0.95 gcm^{-3}	ChemBK (2015)
Thickener	Lupranat M20R	BASF	25.0	1.23 gcm^{-3}	BASF (2019)
Accelerator	BorchiKat 0243	Borchers	0.17	1.00 gcm^{-3}	Borchers (2021)
Fiber	PX35	Zoltek	64.7 wt.-%	1.81 gcm^{-3}	Zoltek (2017)

3.2 Manufacturing of SMC plaques

Plaques were manufactured at Fraunhofer Institute for Chemical Technology, Pfinztal, Germany. Semi-finished sheets were produced on a conveyor plant type HM-LB-800 by Schmidt and Heinzmann. In this process, continuous glass fiber bundles were cut into a length of 25.4 mm and dropped onto a carrier foil that was wetted with resin. Covered with a second carrier foil and resin, the sandwich went through the calendering zone. It was then rolled up and maturated for at least 3 days at 20 $\pm$ 2 °C. Continuous semi-finished sheets were manufactured by feeding unidirectional carbon fiber fabric instead of chopped glass fibers to the conveyor plant. The conventional SMC manufacturing line was extended by heating and cooling sections to start the curing process by increasing the temperature and then stop the cross-linking reactions by cooling the material down to room temperature again. The heating tables had a total length of 9 m and a temperature of 80 °C. The cooling tables had a total length of 1 m and a temperature of 20 °C. The belt speed was 2 mm/min. The temperature profile was chosen in a way that the first reaction of the two-step curing was completed after this manufacturing step. Plaques of 800 mm length and 250 mm width were compression molded on a hydraulic press (COMPRESS PLUS DCP-G 3600/3200 AS by Dieffenbacher). The temperature of the mold was set to 145 °C. A force of 2500 kN was applied during a mold-closing time of 112 s.

Manufacturing of DiCo SMC plaques involved cutting the semi-finished sheets into plies of 400 mm length and 240 mm width. They were stacked and placed into the middle of the mold, in a way that a preferential flow was enforced during compression molding. To manufacture Co SMC plaques, continuous semi-finished sheets were cut into the shape of the rectangular mold and arranged in stacks of four plies each. Therefore, the material did not significantly flow during molding. Hybrid CoDiCo SMC plaques were manufactured in a one-step compression molding process. Depending on the desired material configuration (CoDiCo SMC or CoDiCo$^{0/90}$ SMC), one or two semi-finished continuous carbon fiber plies (0° or 0°/90°) were placed into the mold (100 % mold coverage), followed by a stack of semi-finished DiCo SMC with 50 % mold coverage and one

or two continuous carbon fiber plies (0° or 90°/0°). Doing so, the discontinuous material was enforced to flow in one direction between the continuous plies. The co-molding process is shown schematically in Figure 3.2. Arrows indicate the movement of the upper mold half and the flow direction on DiCo SMC.

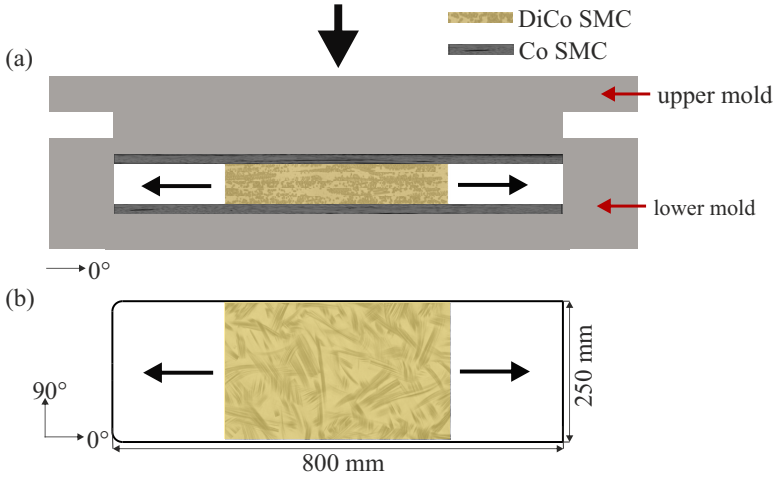

Figure 3.2: (a) Schematic illustration of the compression molding process of CoDiCo SMC and (b) mold geometry indicating the position of the initial charge of DiCo SMC and the flow path.

3.3 Specimen preparation and geometry

Specimens were extracted from the plaques by waterjet cutting at Genther Schneidtechnik GmbH & Co. KG with a cutting quality of Q3 (SN 214001:2010-03). Rectangular shaped specimens were used for the tension-tension fatigue tests. The geometry is shown in Figure 3.3. End tabs were only applied to Co SMC and CoDiCo SMC specimens to protect the unidirectional fibers from damage due to clamping. The end tabs were made of glass fiber multi-axial fabric and

epoxy (PREGNIT GMBE by Krempel GmbH) and were attached to the specimens by using the acrylic adhesive DP810 by 3M following the recommendations in DIN EN ISO 527-5. The width of 15 mm as well as the free length of 100 mm were chosen following Trauth (2020), who investigated the same material systems under quasi-static load, to allow for a comparison of the mean static properties. The free length of all specimens was 50 mm shorter compared to the specifications in DIN EN ISO 527-4 and DIN EN ISO 527-5 and the width of the DiCo SMC specimens was reduced by 10 mm compared to the specifications in DIN EN ISO 527-4. However, Trauth (2020) demonstrated that for DiCo SMC a reduction of the length and width did not lead to a relevant change of mechanical properties. A uniform geometry with a width of 15 mm and a reduced free length of 100 mm was thus considered a good compromise.

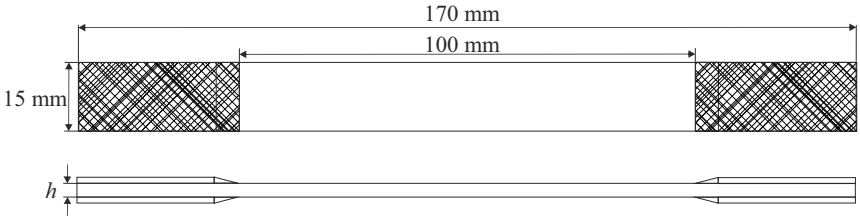

Figure 3.3: Tensile (fatigue) specimens dimensions.

Specimens showed slightly fluctuating dimensions and were measured individually before testing, to allow for a most accurate calculation of the applied stress. The average thickness dimensions of all tensile specimens are summarized in Table 3.4 together with the corresponding variance.

In the hybrid materials, the thickness of the individual plies also showed inter-specimen variation. Four CoDiCo SMC and CoDiCo$^{0/90}$ SMC specimens each were analyzed exemplarily with regard to the thickness of the DiCo SMC and Co SMC plies. However, there is no clear interface between the different plies but rather a transition zone. This can be seen in Figure 3.4 for the example of a CoDiCo$^{0/90}$ SMC specimen. The thickness of a bundle varies strongly over its width and the bundles are partially pushed apart during the molding process, which

Table 3.4: Thickness dimensions of the tensile specimens including coefficient of variation CV.

Material	Thickness h in mm	CV for h in %
DiCo	1.74 ± 0.076	4.37
Co	1.44 ± 0.027	1.87
CoDiCo	2.89 ± 0.077	2.66
$CoDiCo^{0/90}$	3.53 ± 0.120	3.40

results in resin pockets between the bundles. Similar observations were made for CoDiCo SMC specimens with only one 0° carbon fiber reinforcement on each surface. A resin pocket of considerable thickness can also be observed between the 0° and the 90° ply in some cases. The average of ten measurements along the specimen length in the middle of a carbon fiber bundle is considered when measuring the ply thicknesses. The average thickness of an individual Co SMC ply of 0.32 ± 0.021 mm and 0.32 ± 0.028 mm was determined in CoDiCo SMC and $CoDiCo^{0/90}$ SMC, respectively. The DiCo SMC plies featured a thickness of 2.13 ± 0.084 mm in CoDiCo SMC and 1.96 ± 0.084 mm in $CoDiCo^{0/90}$ SMC specimens.

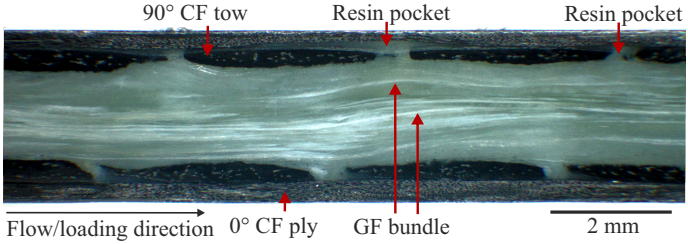

Figure 3.4: Edge of a $CoDiCo^{0/90}$ SMC specimen showing the variation of thickness of the DiCo SMC and Co SMC plies.

Table 3.5 summarizes the thickness dimensions of the coupon specimens used for the bending fatigue tests. The specimen lengths were 50 mm, 60 mm and 100 mm for Co, DiCo and CoDiCo SMC, respectively, and were chosen to be

approximately 120 % of the span length that varied due to the different specimen thicknesses.

Table 3.5: Thickness dimensions of the bending specimens including coefficient of variation CV.

Material	Thickness h in mm	CV for h in %
DiCo	1.70 ± 0.039	2.32
Co	1.43 ± 0.026	1.80
CoDiCo	2.88 ± 0.057	1.99

3.4 Material characteristics

3.4.1 Fiber weight content

The fiber weight content of DiCo SMC and Co SMC plaques was determined by thermogravimetric analysis (TGA) at Fraunhofer Institute of Chemical Technology, Pfinztal, Germany. Specimens were extracted from different plaques as well as from different positions within one plaque to characterize both cross-plaque variations and position-dependent variations. The results are summarized in Figure 3.5a for DiCo SMC and in Figure 3.5b for Co SMC. The fiber volume contents can be calculated with the densities of the UPPH resin and the fibers given in Section 3.1.

The average fiber weight content of the DiCo SMC plaques was be 44.5 ± 3.2 wt.-%. Comparing all TGA specimens, a maximum difference of up to 19 wt.-% was determined. Looking at the example of plaques DiCo7 in Figure 3.5a, vast local variations could also be observed. The adjacent TGA specimens No. 4 and No. 5 revealed a difference in the fiber content of more than 7 wt.-%. The average fiber content of the Co SMC plaques was 64.7 ± 3.1 wt.-%. However, deviations of up to 12 wt.-% were observed within one plaque.

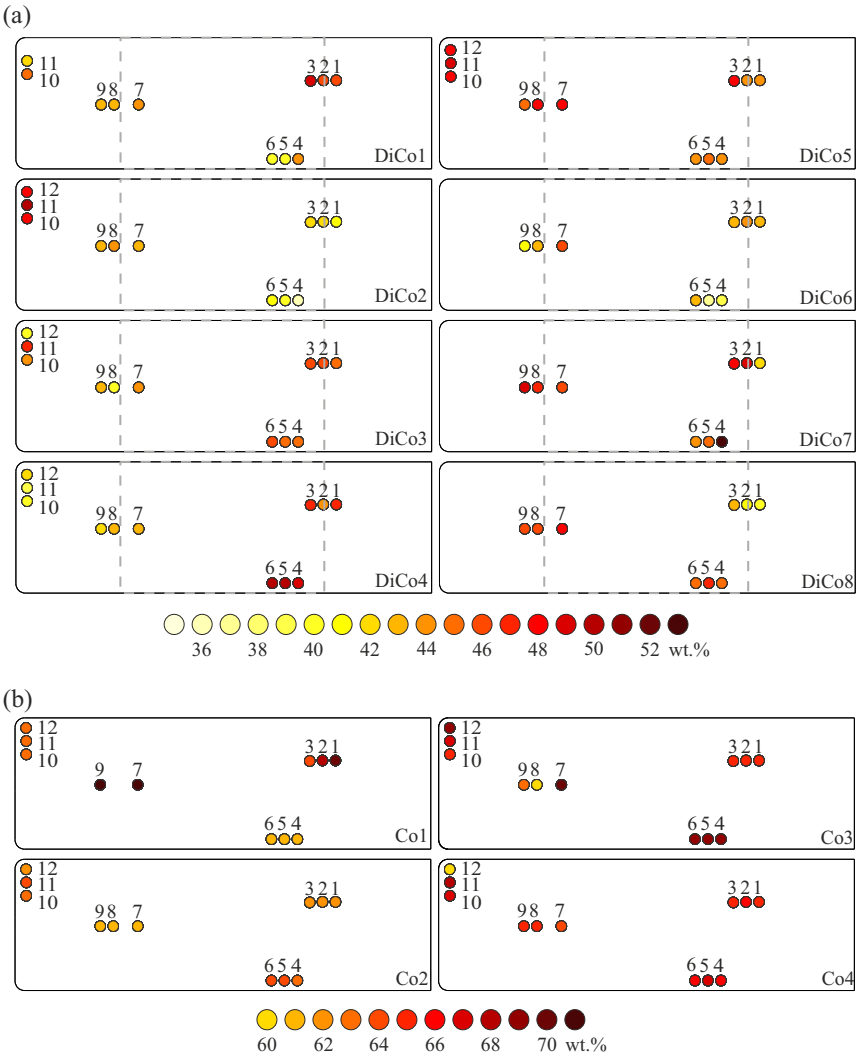

Figure 3.5: Fiber weight content of (a) DiCo SMC plaques and (b) Co SMC plaques obtained by thermogravimetric analysis. The numbers on the panels are the sample numbers.

3.4.2 Microstructure

As a result of the manufacturing process, the initial fiber orientation distribution in the semi-finished DiCo SMC sheets is assumed to be planar isotropic. However, preferential flow during compression molding leads to an increased fiber alignment in flow direction. The fiber orientation distribution is inhomogenous over the thickness due to plug-like flow. While the material in the center only exhibits little shear, the bundle structure is largely retained. High shear stresses in the surface layer close to the mold lead to fiber bundle splicing and partially to an increased curvature. These observations were already reported by Trauth (2020) and also shown for the material considered in this thesis as depicted in Figure 3.6.

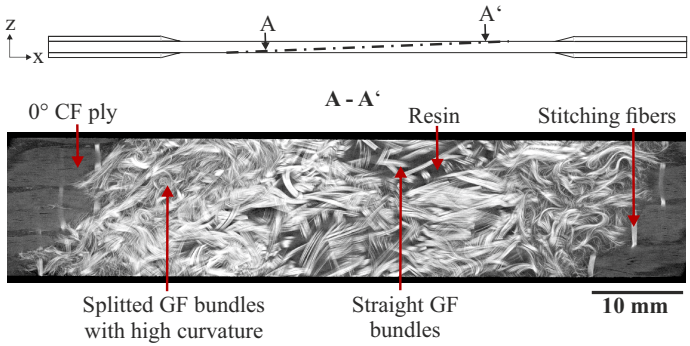

Figure 3.6: Sectional view on the microstructure of CoDiCo SMC obtained from a CT scan. The image was taken from the tilted plane A - A'.

Figure 3.6 shows a 2D µCT image of a CoDiCo SMC specimen that is oriented in flow direction. Going from left to right, the z-coordinate (thickness direction) increases. The effect of fiber bundle splicing and an increased curvature in the outer layer of the DiCo SMC ply is clearly visible. Trauth (2020) observed that the effect of bundle splicing and increased curvature in the outer layer was more pronounced in the DiCo SMC ply of CoDiCo SMC panels compared to DiCo SMC plaques that were molded without the unidirectional reinforcement. The stitch-bonded unidirectional fabric made of 50K continuous carbon fiber tows is shown on the left- and on the right-hand side. The tows are slightly pushed apart

due to the flow of the discontinuous material leading to resin-rich areas between the tows.

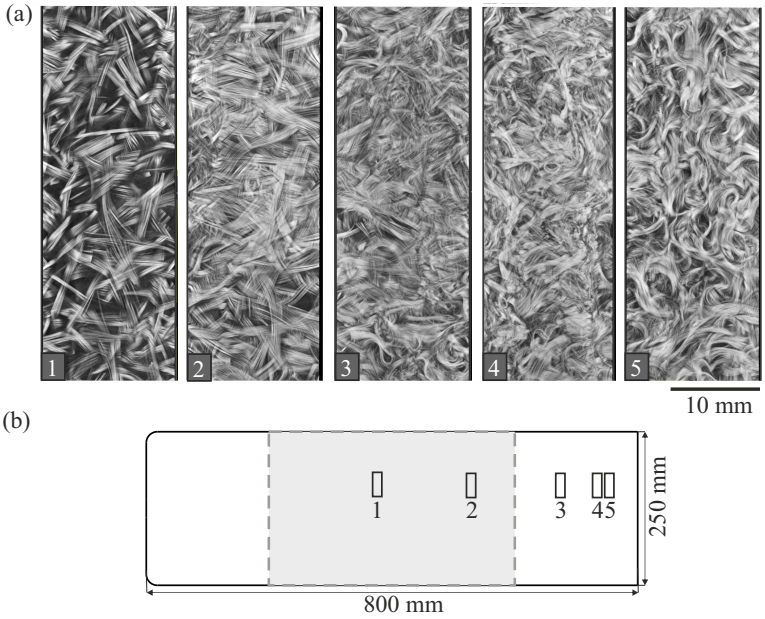

Figure 3.7: (a) Position of five specimens extracted from a CoDiCo$^{0/90}$ SMC plaque for microstructural investigations and (b) sectional view on the microstructure of these specimens obtained from µCT scans. Images were taken from the center plane with regard to the thickness direction.

Figure 3.7a schematically shows a CoDiCo$^{0/90}$ SMC plaque indicating the position of the initial DiCo SMC charge in the mold (grey area). It also indicates the positions of five specimens, that were extracted from the plaques to be analyzed regarding their microstructure. Figure 3.7b shows a sectional view through these specimens. The images show the center plane of the specimens, with regard to their thickness. Moving from left to right (from the charge region to the flow region), the amount of fiber bundle splicing and fiber curvature increases. The characteristic microstructure of DiCo SMC with fibers being largely straight and arranged in bundles, is observed only within a small area in the middle of the

plaques. In flow region, no intact bundle structure remains throughout the whole thickness of the DiCo SMC ply.

Another phenomenon observed after co-molding of CoDiCo$^{0/90}$ SMC plaques is misalignment of the 90° tows in direction of flow. High curvature of these tows can be observed locally in several specimens. An example is given in Figure 3.8.

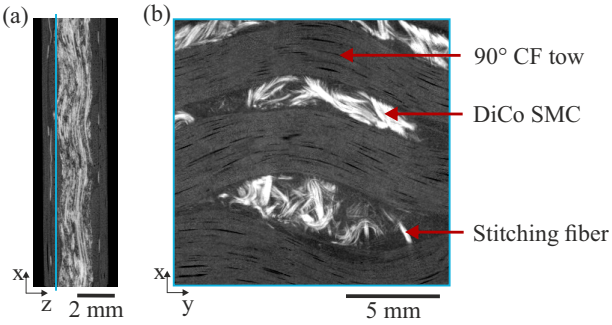

Figure 3.8: µCT scan of a CoDiCo$^{0/90}$ SMC specimen. (a) Position of the considered section over the thickness marked in blue and (b) 2D image showing misaligned 90° carbon fiber tows. The x-direction corresponds to the flow direction.

4 Experimental procedures

The characterization of fatigue properties was carried out according to ISO 13003 and included monotonic tests at quasi-static strain rate as well as at fatigue strain rate. The latter is defined as the strain rate that results in failure of the specimen in a time equivalent to half a cycle time. Fatigue properties were investigated under cyclic tensile loading as well as cyclic bending loading.

4.1 Characterization under tensile loads

4.1.1 Experimental setup

Tensile tests as well as tension-tension fatigue tests were carried out on a servo-hydraulic testing machine (type 1478 by Zwick Roell modified with an additional servo cylinder). The machine was equipped with a load cell (type 1220AJ by interfaceforce) with a capacity of 100 kN. Specimens were hydraulically clamped with a clamping distance of 100 mm. For fatigue testing, an axial clip-on extensometer (type EXA 50-5 by Sandner Messtechnik GmbH) with a gauge length of 50 mm, a measuring displacement of $\pm$ 5 mm and a measuring error of $\pm$ 0.2 % was used to determine the elongation directly on the specimen. The sampling rate of the extensometer was 1000 Hz, resulting in 200 measuring points during one cycle. In addition, a capacitive displacement sensor measuring the displacement of the flange of the actuator was used for displacement control during tensile tests. It was ensured that both measurement systems showed a strictly linear behavior in a displacement range between 0 mm and 5 mm. The experimental setup is shown in Figure 4.1. The ambient temperature in the laboratory was T = 21 °C.

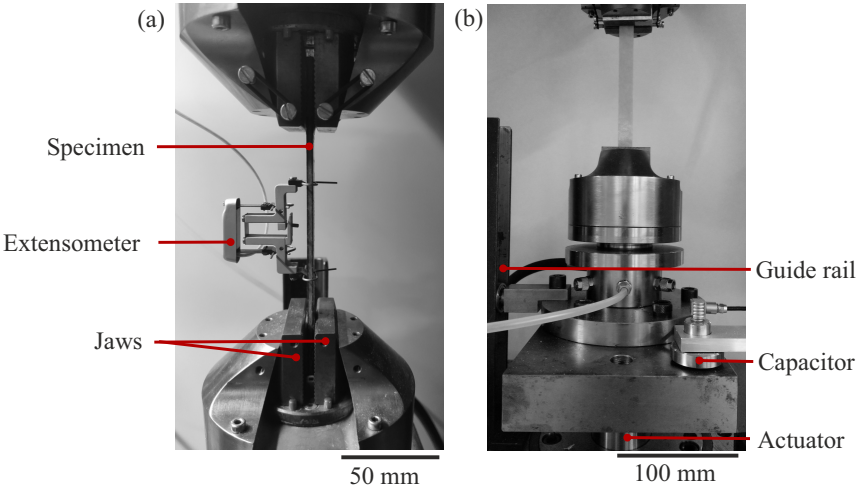

Figure 4.1: Experimental setup for tension-tension fatigue tests with (a) the clip-on extensometer, which was used for strain measurement and (b) the capacitor, which was used for the displacement-controlled tensile test.

4.1.2 Monotonic tensile tests

Monotonic tensile tests were carried out to determine the ultimate tensile strength at quasi-static strain rate (UTS^S) and fatigue strain rate (UTS^F), respectively, with at least five specimens per material system and strain rate. Quasi-static strain-rate corresponds to 2 mm/min according to DIN EN ISO 527-4 and DIN EN ISO 527-5, while the dynamic strain rate defined in ISO 13003 was reached with a nominal actuator speed of 45 mm/s.

4.1.3 Acoustic emission analysis

In the case of DiCo SMC and CoDiCo SMC, additional quasi-static tensile tests were carried out with the aim to determine the average stress, at which damage initiates in the specimens. For this purpose, an AMSY-5 AE analysis system by Vallen Systeme GmbH was used together with two wideband AE sensors (Mistras

HD2WD). Each sensor was linked to a preamplifier of the type AEP3. The setup is shown in Figure 4.2.

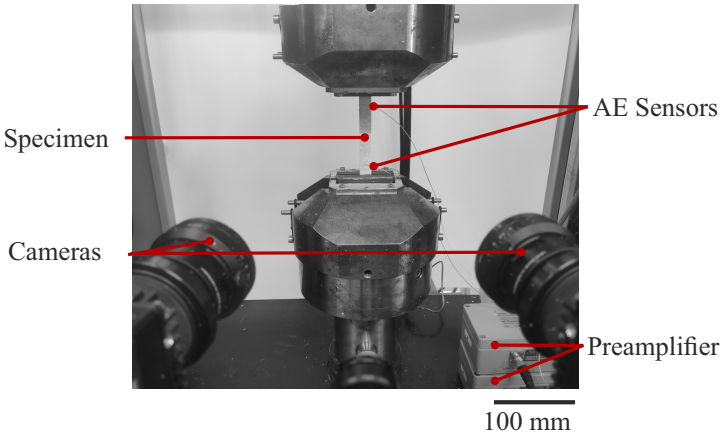

Figure 4.2: Test setup for AE analysis during tensile testing.

A sampling rate of 10 MHz has been selected. The pre-amplification was 34 dB and the threshold was set to 40 dB. A duration discrimination time of 200 µs and a rearm time of 400 µs were chosen. The sensors were positioned at a distance of 70 mm along the specimen length using a 3D-printed bracket and small rubber bands. Silicon grease served as a coupling agent. Correct mounting of the sensors was checked by using a Hsu-Nielsen source according to DIN EN 13554. The use of two sensors allowed the localization of AE signals along the length of the specimen. Only those signals within the 50 mm in the middle of the specimens were included for evaluation. In this manner, signals arising in the clamping region or due to a slight movement of the sensors were neglected. The experiments were carried out on a screw-driven Zwick Roell universal testing machine with a load cell capacity of 100 kN. An Aramis DIC System by gom GmbH was used for strain measurement instead of an extensometer to avoid signal arising from the contact between specimen and extensometer.

4.1.4 Continuous tension-tension fatigue tests

Constant amplitude tension-tension fatigue tests were carried out under load control with a load ratio of R = 0.1, to ensure that the specimens were not exposed to a compressive load at any time. A frequency of 5 Hz was chosen in a way that a temperature increase due to cyclic loading did not exceed 10 °C according to ISO 13003. This was checked by measuring the temperature increase in several specimens during cyclic loading with an IR camera at different stresses (cf. Section 4.1.6).

In each experiment, the mean stress was applied within one second before applying the sinusoidal load. An experiment was declared valid, when the nominal stress amplitude was reached before final failure and if final failure occurred at a distance of more than 10 mm from the jaws. All specimens that met this requirement were included for evaluation of the stress-life fatigue data. For a further evaluation regarding the stiffness degradation behavior, only those specimens that failed within the 50 mm gauge length of the clip-on extensometer were considered. The maximum number of cycles was set to $2.6 \cdot 10^6$ cycles. Specimens that did not fail after this number of cycles were declared runouts.

4.1.5 Interrupted tension-tension fatigue tests

In addition to the continuous tests, several interrupted tension-tension fatigue tests were carried out with DiCo SMC, CoDiCo SMC and CoDiCo$^{0/90}$ SMC specimens to further analyze damage evolution during cyclic loading. The test parameters were selected analogously to the continuous fatigue tests. Before loading, the specimen edges were grinded and polished. Microscopic images were taken from both specimen edges. The specimens were then tested in steps of one decade of cycles until final failure. After each load step, the specimens were unclamped and microscopic investigations of the specimen edges were carried out in an unloaded condition. A quantitative analysis of the images was done with a focus on the

matrix crack density in the DiCo SMC ply within the 50 mm gauge length of the extensometer. The weighted crack length

$$\rho_{\mathrm{w}} = \frac{L_{\mathrm{c,total}}}{h_{\mathrm{DiCo}} \cdot L_{\mathrm{g}}}, \tag{4.7}$$

defined in analogy to Quaresimin et al. (2014) with the accumulated crack length $L_{\mathrm{c,total}}$, the width of the DiCo SMC specimen or DiCo SMC ply h_{DiCo} and the gauge length L_{g} was determined after each load step.

4.1.6 Thermographic investigations

The specimen temperature was monitored for at least one specimen at each stress level by using the infrared camera T420 by FLIR to ensure a maximum temperature rise of 10 °C during cyclic loading on the one hand and to analyze the temperature distribution over the specimen length on the other hand. The temperature was evaluated along a line over the specimen length. Regarding the width direction, the line was positioned in a small distance to one specimen edge, so that beginning damage localization and the location of final failure was captured.

4.2 Characterization under bending loads

4.2.1 Experimental setup

Monotonic and cyclic 3-point bending tests were carried out on an ElectroPuls E3000 by Instron that is equipped with a temperature chamber. The experimental setup is shown in Figure 4.3. The pins prevented the specimens from sliding and twisting. A polytetrafluoroethylene (PTFE) tape was applied onto the lower support, the loading nose and the pins to reduce friction. A span-to-thickness ratio of 1:28 was selected to be used consistently for the different materials for the purpose of comparability, being a compromise with the aim of keeping shear effects in

the continuously reinforced specimens small on the one hand and limiting the maximum deflection of the more flexible DiCo SMC specimens on the other hand. The deflection was determined from the displacement of the crosshead.

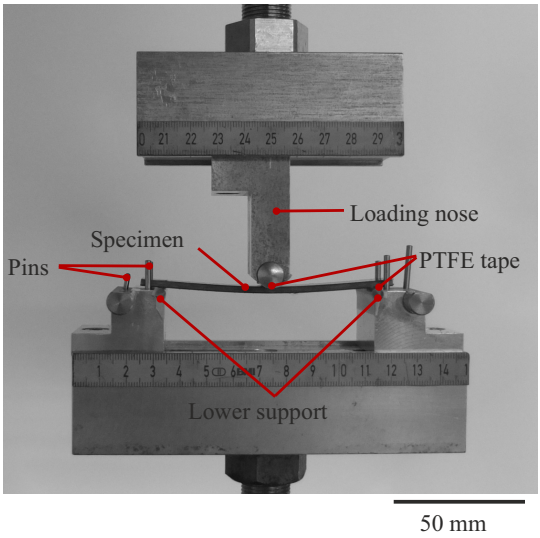

Figure 4.3: Test setup for bending and bending fatigue tests.

4.2.2 Monotonic bending tests

Quasi-static bending tests were carried out at a strain rate of 0.01 min^{-1} according to DIN EN ISO 14125 leading to a crosshead displacement velocity calculated by

$$v = \frac{\varepsilon L^2}{6h}, \tag{4.8}$$

with the outer fiber strain ε, the span length L and the specimen thickness h. The crosshead displacement velocity was 2 mm/min for Co SMC and DiCo SMC and 5 mm/min for CoDiCo SMC. For the tests at fatigue strain rate, the crosshead

velocity was set to 90 mm/s for Co SMC and DiCo SMC and to 180 mm/s for CoDiCo SMC to obtain final failure after around 0.1 s (half a period duration) according to ISO 13003. Assuming the composites behave as homogenous solids on the macroscopic scale, stresses and strains were determined by

$$\sigma = \frac{3FL}{2bh^2} \tag{4.9}$$

$$\text{and } \varepsilon = \frac{6\delta h}{L^2}, \tag{4.10}$$

with the applied force F, span length L, specimen width b, total thickness h and deflection δ (DIN EN ISO 14125). Of note, the hybrid composite is largely inhomogenous on the macroscopic scale. However, assuming macroscopic homogeneity allows for a comparison of the different composites and evaluation of hybridization effects. Failure was defined by a force drop of >80 %.

4.2.3 Bending fatigue tests

Bending fatigue tests were carried out on Co SMC, DiCo SMC and CoDiCo SMC under load control with a load ratio of R = 0.1 and a frequency of 5 Hz at 21 °C, analogously to the tension-tension fatigue tests. Additional test series were carried out with DiCo SMC and CoDiCo SMC to investigate the influence of temperature and frequency on the fatigue behavior.

Table 4.1: Bending fatigue test parameters.

Material	Frequency f	Temperature T	Stress ratio R
DiCo, Co, CoDiCo	5 Hz	21 °C	0.1
DiCo, CoDiCo	5 Hz	80 °C	0.1
DiCo, CoDiCo	5 Hz	-20 °C	0.1
DiCo, CoDiCo	1 Hz	21 °C	0.1
DiCo, CoDiCo	10 Hz	21 °C	0.1

Table 4.1 gives an overview of the different parameter sets used for the experiments. The maximum number of cycles was reduced to $3.6 \cdot 10^5$ cycles for tests carried out at 1 Hz and at -20 °C due to the long test durations on the one hand and since the amount of liquid nitrogen, that was required for cooling, was limited due to the container size on the other hand. An experiment was declared valid, if the target amplitude was reached before final failure. Failure was defined by a stiffness degradation of at least 80 %

5 Experimental results

5.1 Mechanical properties and damage behavior under homogenous loading

5.1.1 Tensile properties

5.1.1.1 Ultimate tensile strength

The results of the tensile tests at quasi-static and fatigue strain rate are summarized in Table 5.1. The tensile strength is strain rate dependent for all investigated materials. DiCo SMC shows the most pronounced strain rate dependence. For further information on the material properties and stress-strain behavior under monotonic loading, the reader is referred to Trauth (2020).

Table 5.1: Ultimate tensile strength of all investigated materials at quasi-static strain rate UTS^S (crosshead velocity of 2 mm/min) and fatigue strain rate UTS^F (crosshead velocity of 45 mm/s). Five specimens were tested for each configuration and strain rate.

	UTS^S			UTS^F		
	$\bar{x}$ in MPa	μ in MPa	CV in %	$\bar{x}$ in MPa	μ in MPa	CV in %
DiCo	197	15.0	7.6	237	14.5	5.9
Co	1002	142.2	14.2	1140	168.8	14.8
CoDiCo	445	22.0	4.9	456	26.5	5.8
$CoDiCo^{0/90}$	382	23.2	6.1	405	52.9	13.1

5.1.1.2 Post-mortem damage analysis

A DiCo SMC specimen that failed due to a tensile load at fatigue strain rate is shown in Figure 5.1. Damage was strongly localized and only few transverse matrix cracks were observed along the specimen apart from the location of final failure, which was characterized by fiber bundle pull-out and pseudo-delamination. In contrast, Co SMC specimens showed a catastrophic failure behavior under tensile load, that included fiber fracture as well as splitting and delamination along the entire specimen length, as depicted in Figure 5.2.

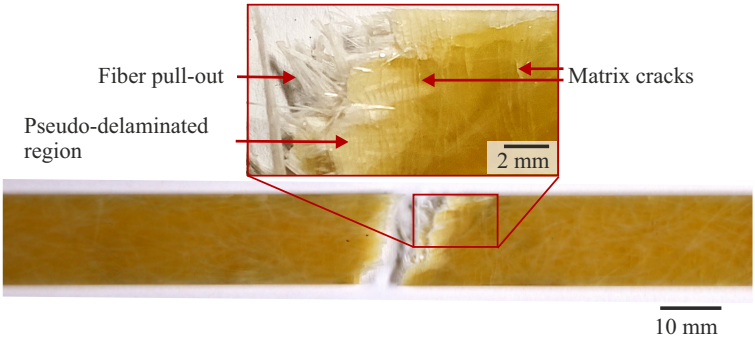

Figure 5.1: DiCo SMC specimen tested under monotonic tensile load at fatigue strain rate.

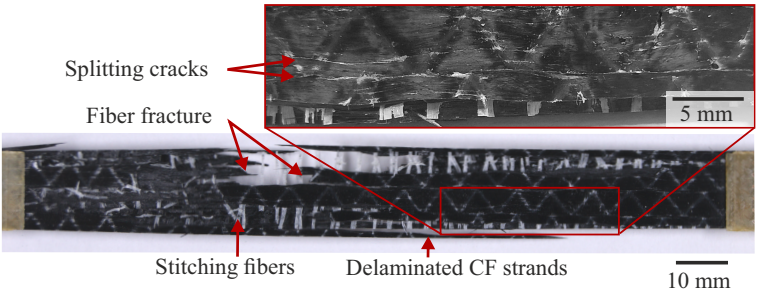

Figure 5.2: Co SMC specimens tested under monotonic tensile load at fatigue strain rate.

The damage pattern of CoDiCo SMC under tensile load varied strongly from specimen to specimen. In all cases, damage extended over a larger area compared to the DiCo SMC specimens and the amount of pseudo-delamination in the DiCo SMC ply was significantly higher. For the specimen shown in Figure 5.3, pseudo-delamination of the DiCo SMC ply extended over approximately 30 mm in both directions from the location of final failure, while in the rest of the specimen almost no signs of damage could be observed. The fibers in the Co SMC ply fractured locally in the region of final failure. Only a thin part of a carbon fiber strand close to the specimen edge delaminated completely while in most part of the specimen the interface between Co SMC and DiCo SMC remained intact. The specimen in Figure 5.4 illustrates the delamination of the Co SMC plies over the entire specimen length and width, along with a high amount of matrix cracking and pseudo-delamination in the DiCo SMC ply.

$CoDiCo^{0/90}$ SMC specimens showed large scale delamination between the 0° and 90° Co SMC plies, as depicted in Figure 5.5. The 0° carbon fiber tows predominantly fractured at the edge of an end tab and were split by longitudinal cracks. Fiber bundle pull-out and pseudo-delamination were observed in the DiCo SMC ply at the location of final failure.

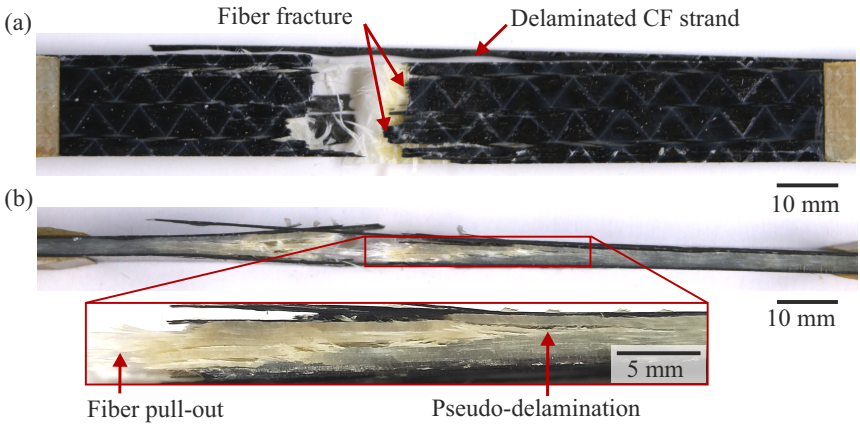

Figure 5.3: CoDiCo SMC specimen tested under monotonic tensile load at fatigue strain rate; damage is localized around the region of final failure.

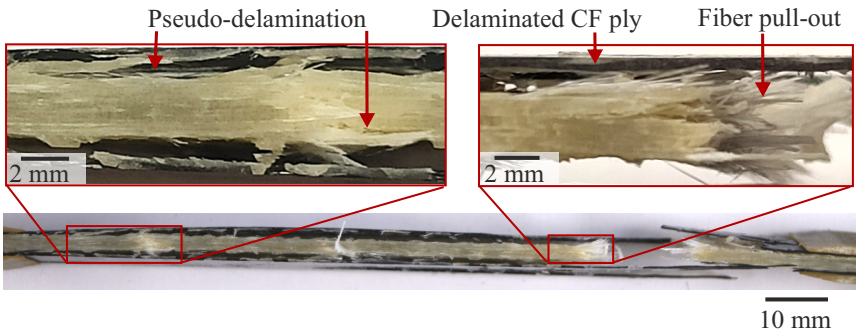

Figure 5.4: CoDiCo SMC specimen tested under monotonic tensile load at fatigue strain rate; Co SMC plies delaminated completely and a high amount of matrix cracks is observed in the DiCo SMC ply over the whole specimen length.

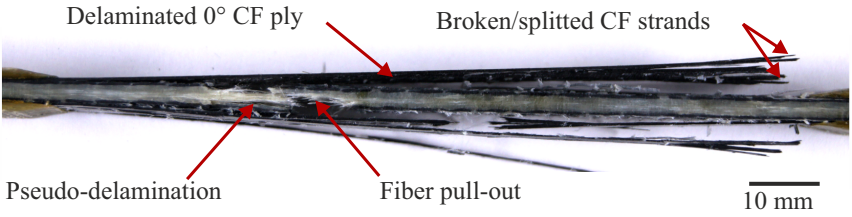

Figure 5.5: CoDiCo$^{0/90}$ SMC specimen tested under monotonic tensile load at fatigue strain rate.

5.1.1.3 Determination of damage initiation

Additional tensile tests at quasi-static strain rate were carried out on DiCo SMC and CoDiCo SMC. In these tests, AE analysis was used for damage monitoring with the aim to determine the stress, at which initial damage occurs. The result is plotted in Figure 5.6a for DiCo SMC. The specified stress corresponds to the mean value of five specimens. An example of the results obtained in one corresponding test is presented in Figure 5.6b, providing the stress response of a representative specimen together with the respective peak amplitudes of the recorded AE signals (HITs). A first HIT was determined at a stress of 56.8 MPa on average.

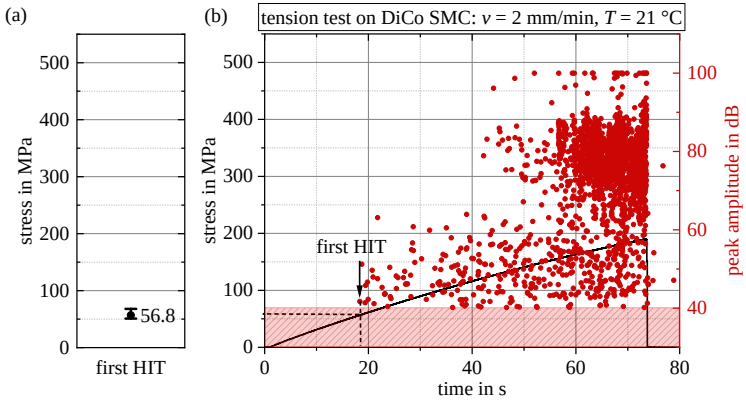

Figure 5.6: Results obtained from AE analysis during quasi-static tensile tests of DiCo SMC.
(a) Mean value and scatter range of the stress at which the first HIT was recorded and
(b) force signal from a representative specimen including the peak amplitudes of the HITs.

Figure 5.7a reveals similar results for CoDiCo SMC, where the first HIT was recorded at a stress of 56 MPa on average. As can be seen from Figure 5.7b this HIT has a high peak amplitude.

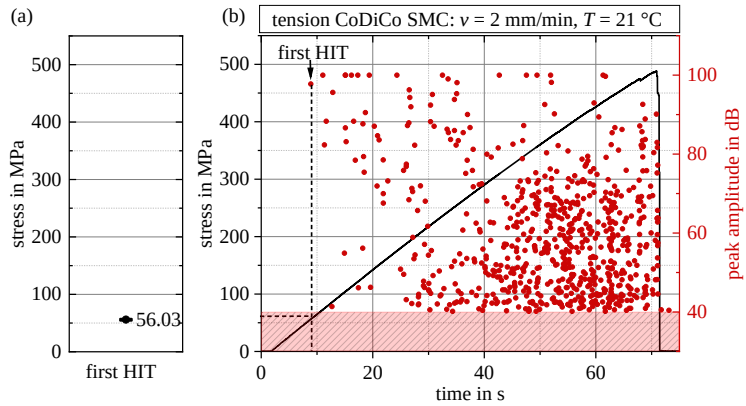

Figure 5.7: Results obtained from AE analysis during quasi-static tensile tests of CoDiCo SMC.
(a) Mean value and scatter range of the stress at which the first HIT was recorded and
(b) force signal from a representative specimen including the peak amplitudes of the HITs.

5.1.2 Tension-tension fatigue behavior

5.1.2.1 Test parameters

Table 5.2 summarizes the investigated stress levels for the tested composites. The specified values correspond to the homogenized maximum stress during cyclic loading and are given both in % UTS^F and in MPa. At least five specimens were tested at each load level, if the applied stress led to failure of the specimen within $2.6 \cdot 10^6$ cycles. For the lowest load level, the number of specimens was reduced, due to the long test durations.

Table 5.2: Load levels investigated in tension-tension fatigue tests.

DiCo SMC		Co SMC		CoDiCo SMC		$CoDiCo^{0/90}$ SMC	
max. stress in		max. stress in		max. stress in		max. stress in	
% UTS^F	MPa	% UTS^F	MPa	% UTS^F	MPa	% UTS^F	MPa
79	187	75	855	90	405	85	344
68	163	70	798	85	382	75	304
58	137	65	741	80	360	65	263
51	120	60	684	75	337	55	223
42	100	55	627	70	315	48	194
37	87			65	292	40	162
				60	270		

5.1.2.2 Tension-tension fatigue behavior of DiCo SMC

Stress-life data

The S-N diagram in Figure 5.8 contains the results of the (uninterrupted) constant amplitude fatigue tests on DiCo SMC as well as the results of the tensile test at fatigue strain rate. Runouts are labeled with an arrow. The numbers behind

the arrows indicate the number of runouts at the corresponding maximum stress. The left y-axis shows the maximum applied stress in MPa, while the right y-axis ordinate shows the respective value in % UTS^F. In the stress range between 100 MPa and 185 MPa, failure occurred due to fatigue. First runouts were obtained at a maximum stress of 100 MPa (42 % UTS^F). At 87 MPa (37 % UTS^F), no failure occurred within $2.6 \cdot 10^6$ cycles. Fatigue strength decreased by approximately 10 % UTS^F per decade of cycles and was subject to scatter in the range of more than two decades of cycles.

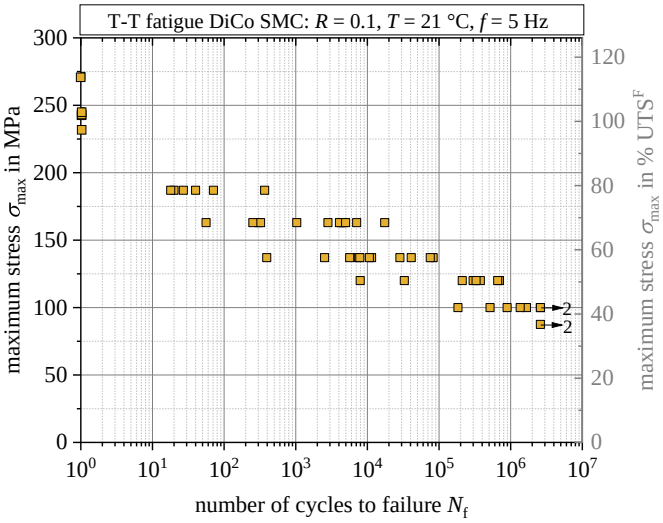

Figure 5.8: S-N data of DiCo SMC under tension-tension (T-T) fatigue load.

Post-mortem analysis of macroscopic damage

DiCo SMC specimens, that were tested at 79 % UTS^F, showed a similar damage pattern compared to those that were tested monotonically (Figure 5.1). As demonstrated in Figure 5.9, damage was highly localized, while hardly any matrix cracks were visible apart from the region of final failure. The specimen in Figure 5.10

was tested at 51 % UTS^F and revealed a high density of matrix cracks along the entire specimen length. The crack distribution was not homogenous due to local variations of the fiber content and fiber orientation distribution. In general, the crack density was higher in specimens that failed in the high cycle fatigue range than in specimens, that failed after fewer cycles.

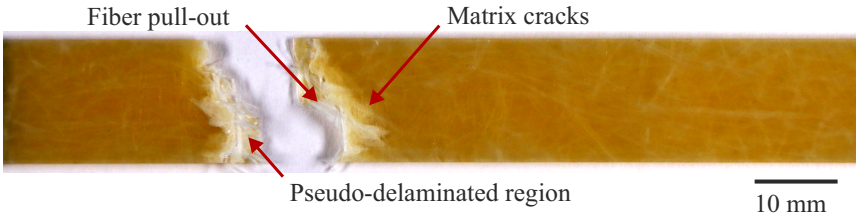

Figure 5.9: DiCo SMC specimen that was tested at a maximum stress of 187 MPa and failed after 71 cycles due to fatigue.

Figure 5.10: DiCo SMC specimen that was tested at a maximum stress of 120 MPa and failed after approximately $3 \cdot 10^5$ cycles due to fatigue.

Stress-strain behavior

The hysteresis loops of three representative specimens that were tested at different load levels are displayed in Figure 5.11. The specimen in Figure 5.11a was tested at the highest load of 79 % UTS^F and failed in the low cycle fatigue range after 27 cycles. A slight tilting of the hysteresis loop correlated with an increasing number of cycles. The specimen tested at 58 % UTS^F in Figure 5.11b failed in the high cycle fatigue range after 75,497 cycles. A shift of the hysteresis loop

(shift of the minimum strain) by approximately 0.13 % strain correlated with an increasing number of cycles and an increasing tilt. Final failure occurred at a lower maximum strain compared to the specimen tested at 79 % UTS^F. Figure 5.11c shows the hysteresis loops of a runout specimen that was tested at 42 % UTS^F. A shift of approximately 0.05 % strain was observed together with slight tilting of the hysteresis loops.

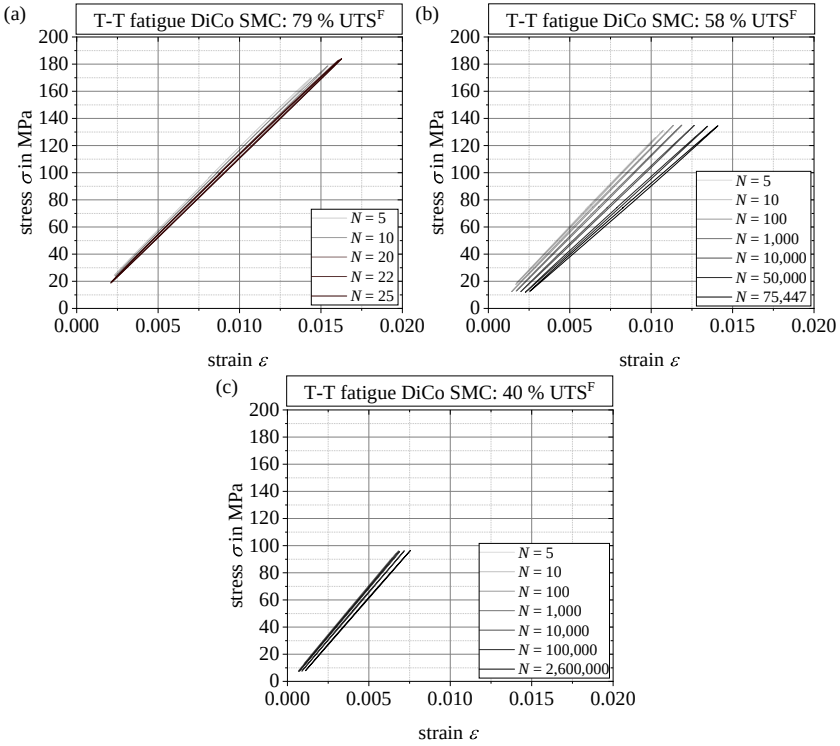

Figure 5.11: Representative hysteresis loops of DiCo SMC specimens under tension-tension fatigue load obtained at (a) 79 % (N_f = 27), (b) 58 % (N_f = 75,487) and (c) 42 % UTS^F (runout), respectively.

Stiffness degradation

The evolution of the normalized dynamic stiffness, which describes the tilt of the hysteresis loops, is depicted in Figure 5.12 for the different maximum applied stresses. Normalized values were used for comparability. The absolute values can roughly be estimated from Figure 5.12, using the average initial stiffness of DiCo SMC of 13.9 GPa ($\mu = 0.8$ GPa). The intial stiffness refers to the value of the fourth cycle, which was chosen due to slight irregularities in the start-up behavior of the machine. Each line represents a single specimen having a fatigue life in the medium range, compared to other specimens tested at the same stress level.

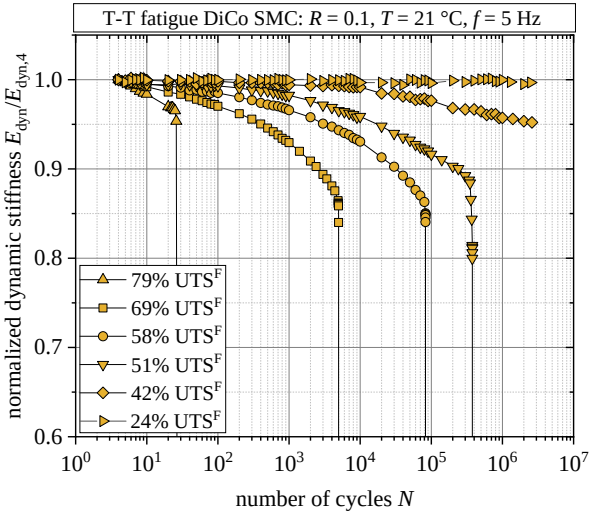

Figure 5.12: Normalized dynamic stiffness of representative DiCo SMC specimens under tension-tension fatigue load at different load levels; 100 % $UTS^F \mathrel{\hat{=}} 237$ MPa, $\bar{E}_{dyn,4} = 13.9$ GPa ($\mu = 0.8$ GPa).

Cyclic loading led to a degradation of the dynamic stiffness. The degradation rate increased in relation to the applied load. At maximum stresses between 51 % and 68 % UTS^F, stiffness degradation rate started to markedly increase shortly before

final failure after a total stiffness loss of 11 % to 14 %. Separation of the specimen occurred after a total stiffness loss of 16 % to 20 %. The specimen tested at 79 % UTS^F showed a considerably lower stiffness loss of less than 5 % before final failure. The specimen tested at 42 % UTS^F did not fail within $2.6 \cdot 10^6$ cycles, but a stiffness loss of approximately 5 % was observed, nevertheless. At 56.8 MPa, which corresponds to the average stress at which initial damage was recorded during a monotonic tension test (cf. Figure 5.6), no stiffness degradation was observed at all. In Figure 5.13, the results are expressed as damage parameter D over the normalized number of cycles. The evolution of damage with respect to the normalized fatigue life was largely independent of the applied load. The damage parameter for specimens tested at maximum stresses between 51 % and 69 % UTS^F showed a similar course, while only the specimen that was tested at 79 % UTS^F and failed after 27 cycles, showed a deviant behavior.

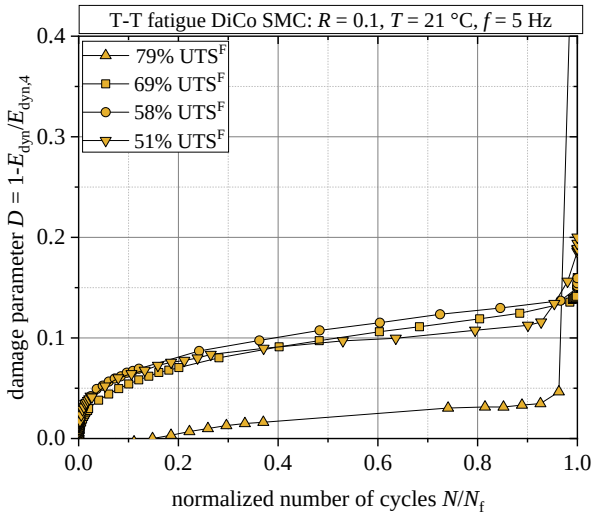

Figure 5.13: Damage parameter of DiCo SMC obtained under tension-tension fatigue load; 100 % $UTS^F \mathrel{\hat{=}} 237$ MPa, $\bar{E}_{dyn,4} = 13.9$ GPa ($\mu = 0.8$ GPa).

Damage evolution

Damage evolution is illustrated in Figure 5.14. The upper left depicts the stiffness degradation curve of a specimen tested at 58 % UTS^F. The remaining figure panel entails microscopic images of a small section of the specimen edge that was captured after different numbers of cycles. The initial scan is shown in the upper right.

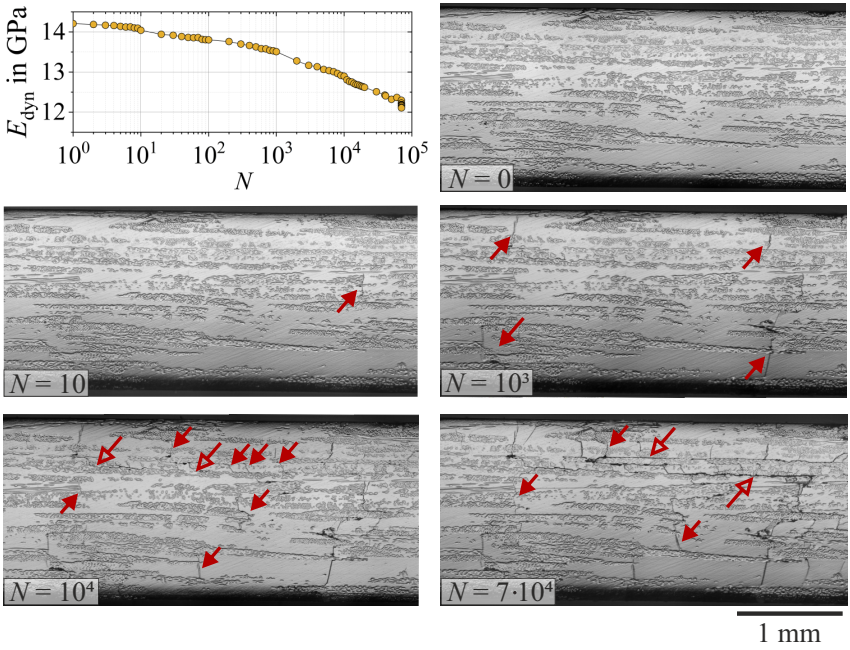

Figure 5.14: Stiffness degradation curve of a DiCo SMC specimen tested at 58 % UTS^F and microscopic images of a section of one specimen edge after different numbers of cycles; filled arrows indicate matrix cracks and hollow arrows indicate pseudo-delamination.

After 10 cycles, a first crack appeared, that is marked by the red arrow in the middle left panel. Three more cracks were visible in this section after 10^3 cycles starting from the specimen edges with considerable distance to each other. Up to this point, the specimen lost approximately 4.5 % of its initial stiffness. With

additional cycles, more cracks emerged with a smaller distance in between each other. Cracks started to accumulate and pseudo-delamination could be observed, marked by hollow arrows in the bottom panels. This resulted in a total stiffness loss of 9 % and 14.5 % after 10^4 and $7 \cdot 10^4$ cycles, respectively. Final failure occurred 258 cycles after the last image was taken outside of the observed length. The damage pattern in terms of crack length and distance was dependent on the local microstructure, that varied extensively along the specimen. Figure 5.15 shows a different region of the same specimen presented in Figure 5.14, featuring large matrix-rich regions with long cracks and fiber-rich regions with small cracks.

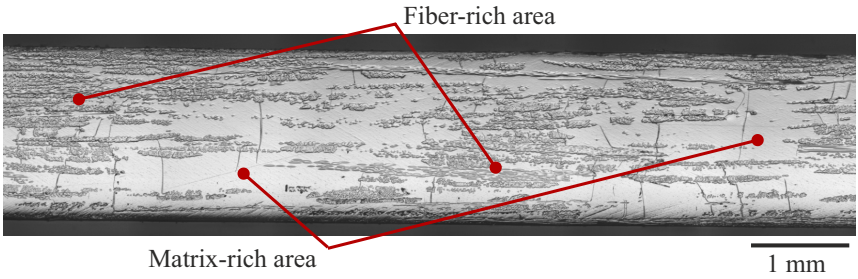

Figure 5.15: Microscopic image of a DiCo SMC specimen tested at 58 % UTS^F after $7 \cdot 10^4$ cycles showing the inhomogeneity in the fiber volume content and the resulting damage pattern.

Matrix cracks were counted and measured at both specimen edges within the gauge length of the extensometer. The weighted crack length determined after different numbers of cycles is given in Figure 5.16, together with the damage parameter derived from the stiffness degradation curve shown in Figure 5.14. Due to partially missing data on one side of the specimen after 10^3 cycles, one data point is missing in the diagram. Nevertheless, a similar development of the damage parameter, derived either from the stiffness degradation data or the weighted crack length, could be observed from Figure 5.16.

Comparable results were observed for a second specimen tested at the same maximum stress, as well as for one specimen tested at 51 % UTS^F in Figure 5.17 and Figure 5.18, respectively.

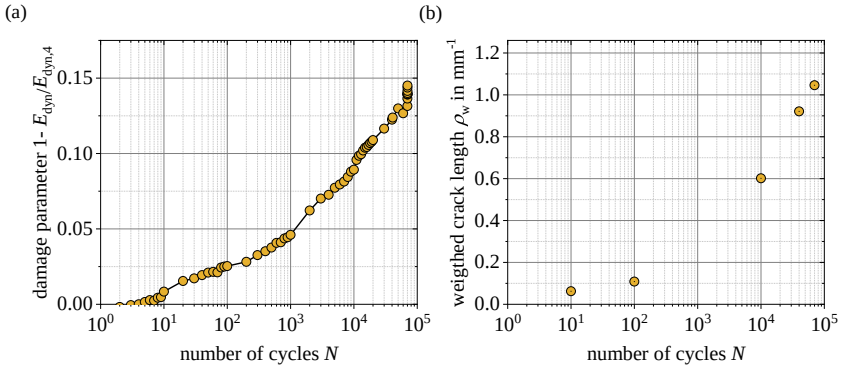

Figure 5.16: (a) Damage parameter of a DiCo SMC specimen tested at 58 % UTS^F and (b) weighted crack length determined from both specimen edges within the gauge length of the extensometer after different numbers of cycles.

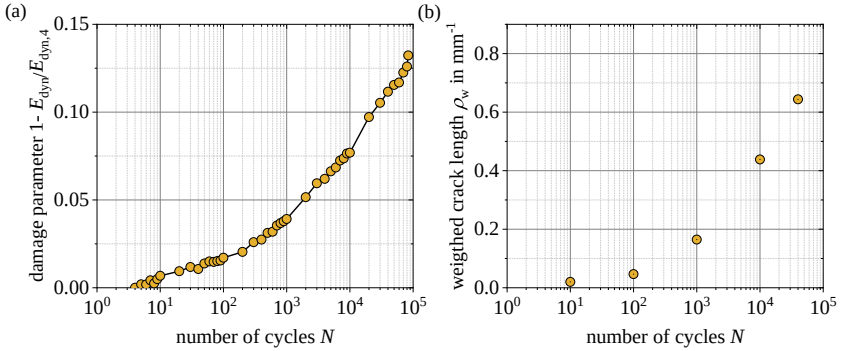

Figure 5.17: (a) Damage parameter of a second DiCo SMC specimen tested at 58 % UTS^F and (b) weighted crack length determined at both specimen edges within the gauge length of the extensometer after different numbers of cycles.

Figure 5.19a delineates the conversion factor between the damage parameter and the corresponding weighted crack length for the different specimens. A connection between the two quantities was not determinable at low numbers of cycles, where the weighted crack length was very small, but became more definite with increasing numbers of cycles and thus higher weighted crack lengths. The

conversion factor ranged between 0.1 mm and 0.2 mm. Expressed in terms of the absolute stiffness loss, the conversion factor was between 1.5 GPa·mm and 3 GPa·mm (Figure 5.19b).

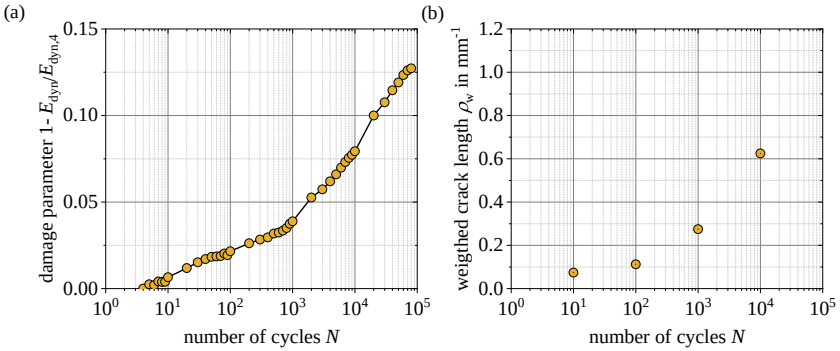

Figure 5.18: (a) Damage parameter of a DiCo SMC specimen tested at 51 % UTS^F and (b) weighted crack length determined from both specimen edges within the gauge length of the extensometer after different numbers of cycles.

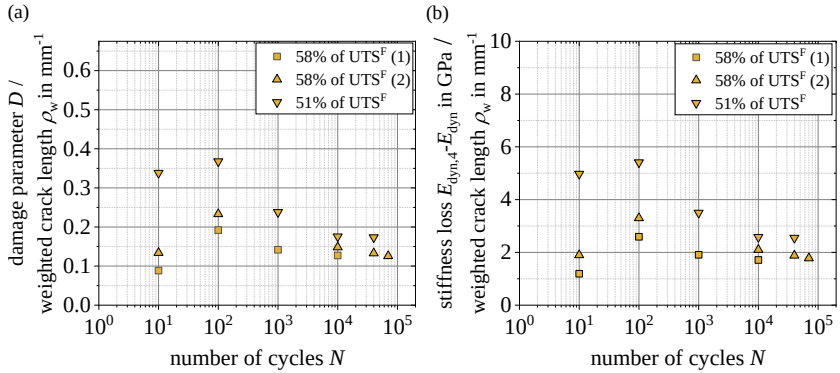

Figure 5.19: Correlation factor between (a) damage parameter and weighted crack length and (b) absolute stiffness loss and weighted crack length for different DiCo SMC specimens.

IR Thermography observations

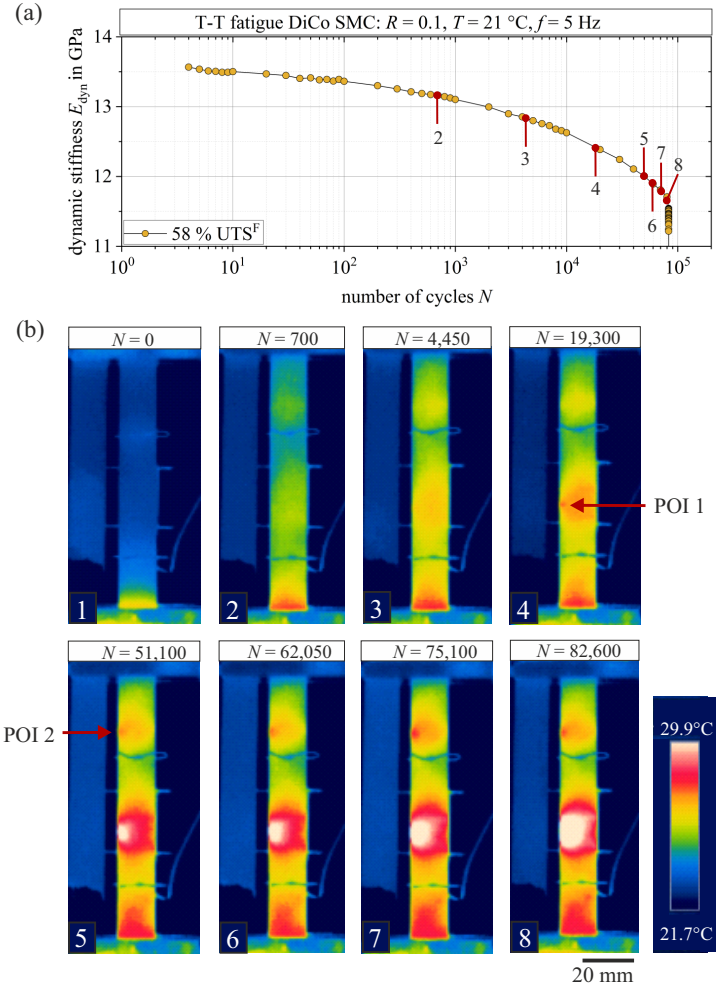

Figure 5.20: (a) Stiffness degradation curve and (b) IR images of a DiCo SMC specimen captured during a tension-tension fatigue test at 58 % UTS^F after different numbers of cycles.

The evolution of temperature over time of a representative DiCo SMC specimen is shown in Figure 5.20. Images were taken after different numbers of cycles that are marked red in the stiffness degradation curve in Figure 5.20a. Infrared images in Figure 5.20b visualize the temperature distribution over the clamped specimen prior to applying the load. Temperature data was extracted over the specimen length along the scale in Figure 5.21a to capture the onset of localization at the specimen edges. The respective temperature profile is depicted in Figure 5.21b for different numbers of cycles.

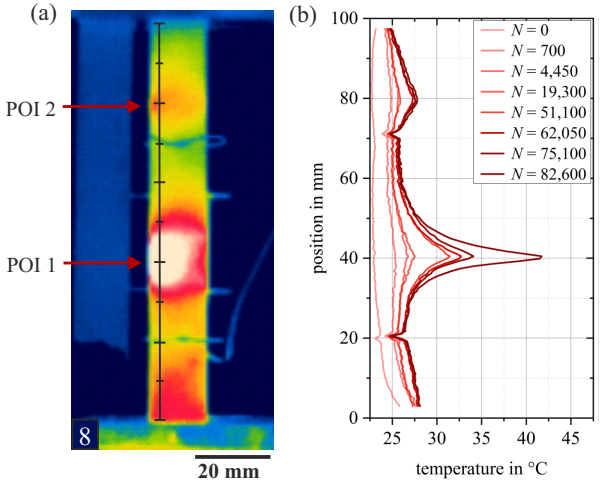

Figure 5.21: (a) DiCo SMC specimen tested at 58 % UTS^F marked with a scale, along which the temperature data was extracted and (b) temperature profile over specimen length after different numbers of cycles *N*.

Temperature increased almost uniformly over the specimen length within the first cycles. Higher temperatures observed near the lower clamp were due to the temperature of the jaw and not damage-related. After approximately $2 \cdot 10^4$ cycles (panel 4), temperature increased more localized with a marked peak at POI 1 (location of final failure). A less pronounced localization was visible at POI 2 after approximately $5 \cdot 10^4$ cycles (panel 5). The lower temperatures at 20 mm and 70 mm were caused by the clamps, that attached the extensometer to the

specimen. The localized temperature increase at 40 mm (POI 1) and 80 mm (POI 2) could be seen after $4.45 \cdot 10^3$ cycles and became more pronounced after $5.11 \cdot 10^4$ cycles. With increasing numbers of cycles beyond this point, a further temperature increase was limited to the region around POI 1.

5.1.2.3 Tension-tension fatigue behavior of Co SMC

Stress-life data

Figure 5.22 shows a fatigue life diagram of Co SMC. The stress range in which specimens failed due to fatigue was between 680 MPa and 855 MPa. All specimens loaded at 625 MPa, which corresponds to 55 % UTS^F, were runouts. Fatigue strength decreased by approximately 5 % UTS^F per decade of cycles. Scatter was more pronounced than in DiCo SMC. Looking at the results obtained at 70 % UTS^F, for example, the scatter range covers between 31 and approximately $1.2 \cdot 10^5$ cycles.

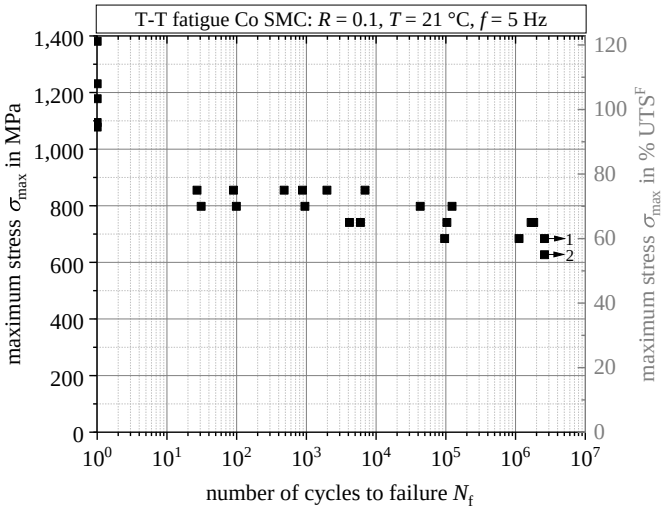

Figure 5.22: S-N data of Co SMC under tension-tension fatigue load.

Post-mortem analysis of damage mechanisms

The Co SMC specimens tested under cyclic loading showed a catastrophic failure behavior characterized by a large number of splitting cracks, delamination and fiber bundle fracture analogous to the specimens that were tested monotonically (Figure 5.2). Figure 5.23 shows a Co SMC specimen that was tested at a maximum stress of 685 MPa (60 % UTS^F) and did not fail within $2.6 \cdot 10^6$ cycles. Splitting cracks in the outer carbon fiber ply could nevertheless be observed along with large-scale delamination at the specimen edges.

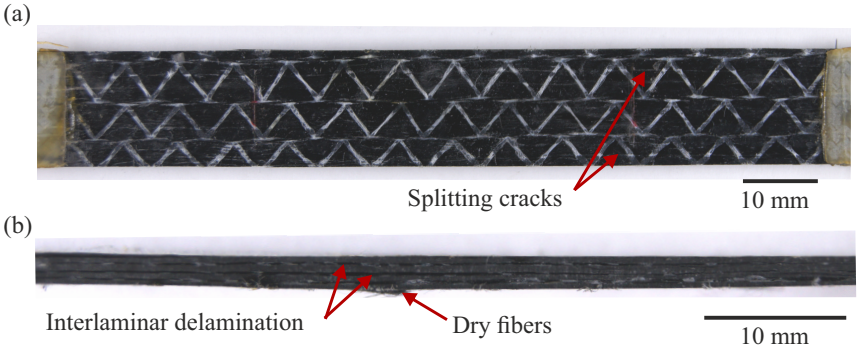

Figure 5.23: Damage pattern of a Co SMC specimen after $2.6 \cdot 10^6$ cycles at a maximum stress of 60 % UTS^F.

Stress-strain behavior

The hysteresis loops of three different Co SMC specimens are shown in Figure 5.24. The specimen in Figure 5.24a was tested at the highest maximum stress of 855 MPa and failed after 212 cycles. The composite exhibited tension stiffening behavior, meaning that stiffness increased with applied stress. A shift of approximately 0.1 % strain could be observed. At 65 % UTS^F, an overall shift of the hysteresis loop of approximately 0.3 % strain was measured, which was considerably higher compared to DiCo SMC. Final failure occurred at a higher maximum strain than

in the specimen tested at 75 % UTS^F. The hysteresis loop of the runout specimen (Fig. 5.24c) also showed a considerable amount of shift and tilt. The slope of the hysteresis loops slightly increased with increasing stress, while the slope was almost constant or slightly decreased for DiCo SMC.

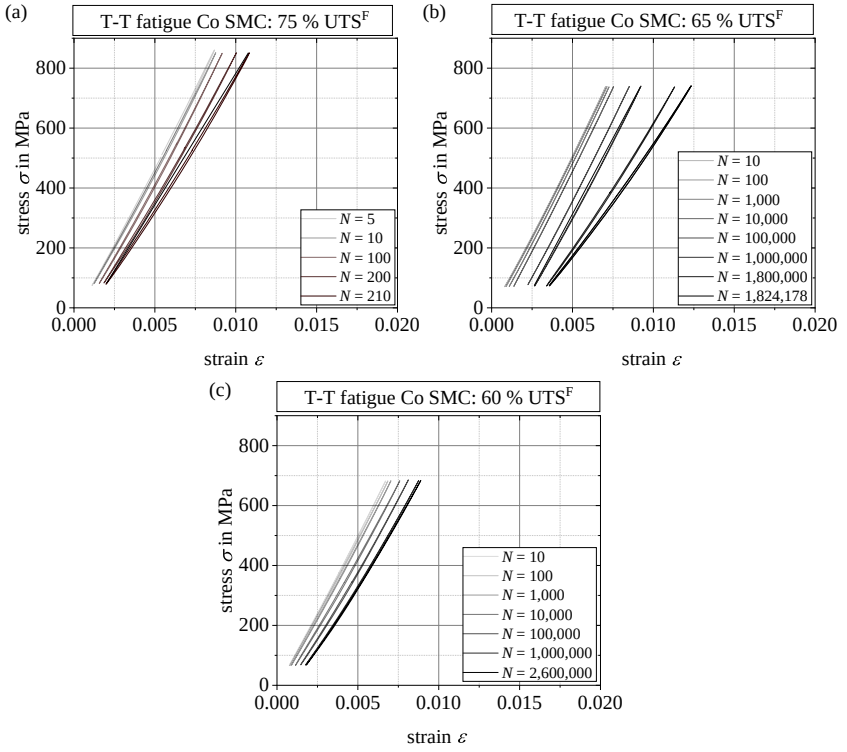

Figure 5.24: Hysteresis loops of Co SMC specimens under tension-tension fatigue load obtained at (a) 75 % (N_f = 212), (b) 65 % (N_f = 1,824,228) and (c) 60 % UTS^F (runout), respectively.

Stiffness degradation

The normalized stiffness degradation curves of Co SMC specimens are illustrated in Figure 5.25. At a maximum stress of 65 % UTS^F, no valid strain data for specimens with an average fatigue life was available, compared to other specimens tested at the same stress level. Therefore, data is presented for two specimens, of which one showed a fatigue life above and one below average. Several jumps occurred in the stiffness degradation curves that were observed to be caused fiber cluster fracture. Occurrence of such fiber cluster fractures within the measuring length led to a sudden drop of stiffness. An (apparent) increase of stiffness was determined for the specimen tested at 65 % UTS^F after approximately 500 cycles. The overall stiffness loss before separation of the specimens increased with decreasing applied load. At 75 % UTS^F final failure occurred after a stiffness loss of approximately 17.5 %, while for the specimens tested at 65 % UTS^F a stiffness loss of 30 % was observed. The specimen tested at 60 % UTS^F lost 16 % of its initial stiffness due to cyclic loading.

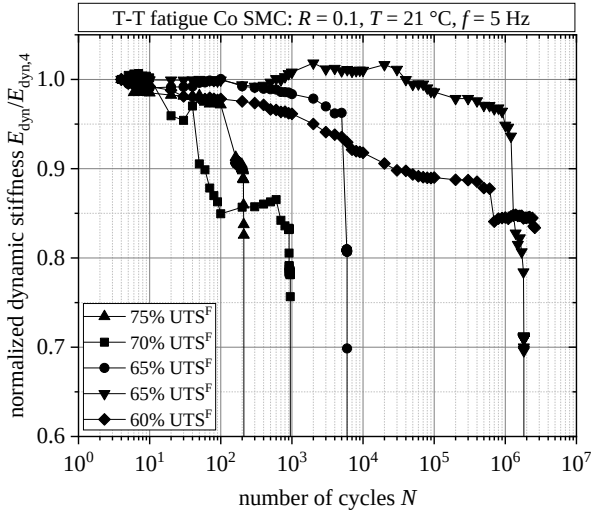

Figure 5.25: Normalized dynamic modulus of Co SMC under tension-tension fatigue load; 100 % $UTS^F \mathrel{\hat{=}} 1140$ MPa, $\bar{E}_{dyn,4} = 103.9$ GPa ($\mu = 2.1$ GPa).

A similar trend of the damage evolution was observed for the different applied maximum stresses from the assessment of the damage parameter in Figure 5.26. Notably, local fiber cluster fracture leading to jumps in the damage curve appeared at different times during the fatigue life, that could not be correlated with the applied maximum stress. The specimen tested at 70 % UTS^F was subject to a considerable amount of damage at an early stage of fatigue life. Looking at the other specimens, a first jump in the damage curve was observed after more than 50 % their respective fatigue life.

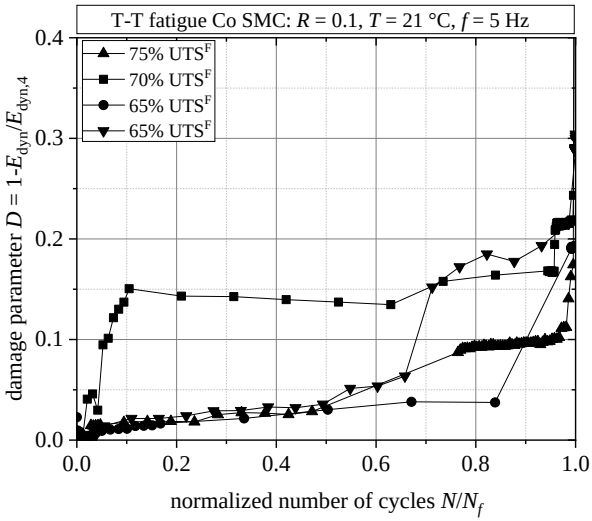

Figure 5.26: Damage parameter of Co SMC obtained under tension-tension fatigue load; 100 % $UTS^F \doteq 1140$ MPa, $\bar{E}_{dyn,4} = 103.9$ GPa ($\mu = 2.1$ GPa).

5.1.2.4 Tension-tension fatigue behavior of CoDiCo SMC

Stress-life data

The stress range in which CoDiCo SMC specimens failed due to fatigue within $2.6 \cdot 10^6$ cycles was between 290 MPa and 380 MPa, as can be seen from Figure 5.27. Above 380 MPa, specimens were likely to fail immediately or within the first few cycles. At a maximum stress of 270 MPa, which corresponds to approximately 60 % UTS^F, no specimen failed within the considered number of cycles. Single runouts were also obtained at higher stresses of up to 75 % UTS^F. For most stress levels, scatter was in the range of three decades of cycles.

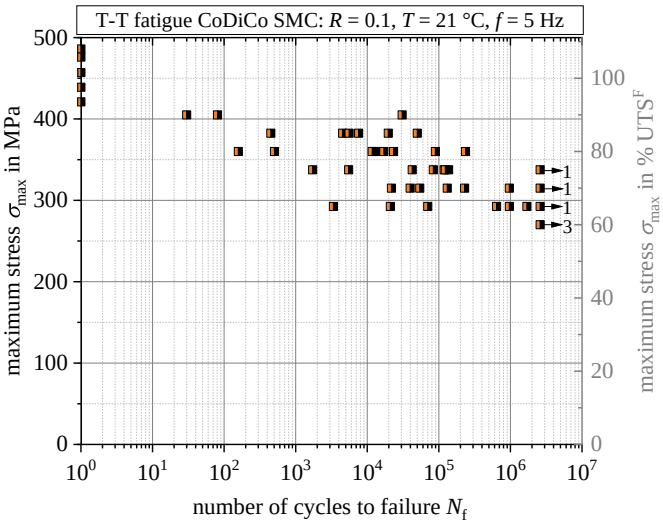

Figure 5.27: S-N data of CoDiCo SMC under tension-tension fatigue load.

Post-mortem analysis of macroscopic damage

Figure 5.28 shows a CoDiCo SMC specimens that failed due to cyclic loading at 85 % UTS^F. The main damage mechanisms were very similar to the ones observed under monotonic loading, such as splitting cracks and fiber fractures in the Co SMC ply, delamination between the Co SMC and DiCo SMC plies, as well as fiber bundle pull-out and pseudo-delamination in the DiCo SMC ply. The density of splitting cracks was higher in specimens tested under cyclic load. Additionally, a large amount of matrix spalling at the surface was observed for cyclically loaded specimens and the crack density in the DiCo SMC ply was higher across the entire specimen length. The proportion of the different damage mechanisms was very distinct from specimen to specimen.

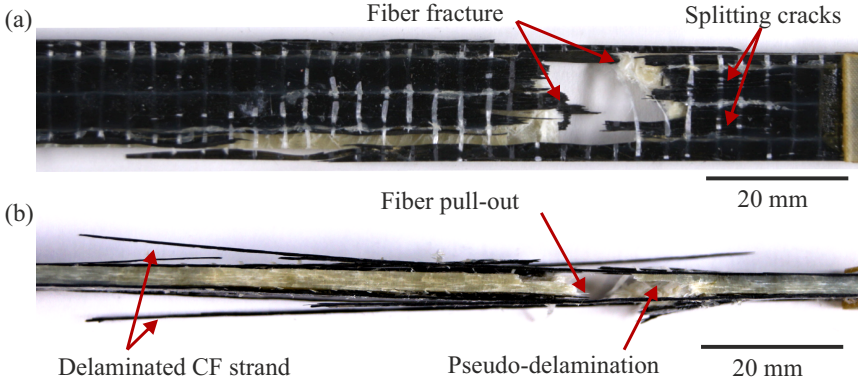

Figure 5.28: (a) Topview and (b) sideview of a CoDiCo SMC specimen tested at 85 % UTS^F after fatigue failure.

CoDiCo SMC specimens that did not fail within the considered number of cycles showed no or only minor signs of damage in the form of detached stitching fibers, some splitting cracks and partial delamination in the Co SMC ply at the specimen edge (Figure 5.29a). In the DiCo SMC ply, a large amount of matrix cracks along the entire specimen was observed, of which only a few were marked in Figure 5.29b.

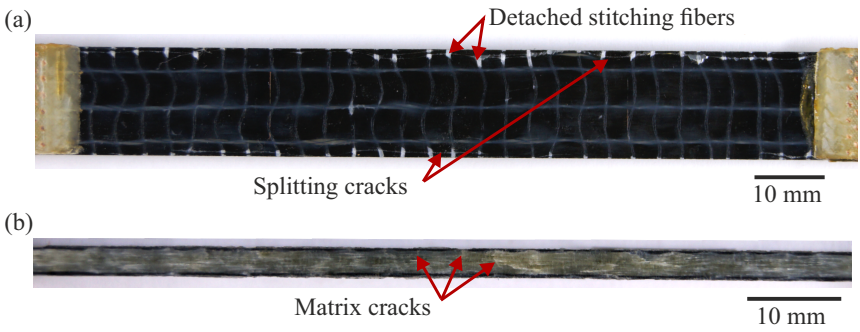

Figure 5.29: (a) Topview of the Co SMC ply and (b) sideview of the DiCo SMC ply of a CoDiCo SMC specimen loaded at 60 % UTS^F after $2.6 \cdot 10^6$ cycles.

Stress-strain data

The evolution of the hysteresis loops of CoDiCo SMC specimens was mainly characterized by increasing tilt. Only a small amount of shift could be observed. The composite exhibited slight tension stiffening, similar to Co SMC (cf. Figure 5.24). For the specimen depicted in Figure 5.30b tested at 89 % UTS^F, a shift of less than 0.1 % strain was determined after $2.3 \cdot 10^5$ cycles, shortly before final failure. This is considerably less than what was observed for DiCo and Co SMC.

Stiffness degradation

As can be seen from Figure 5.31, the dynamic stiffness decreased in an almost linear manner (approximately 1 % stiffness loss per decade of cycles) for a large range of fatigue life and showed a sudden drop, which occurs the sooner, the higher the applied load.

The damage parameter of the specimens tested at loads between 70 % UTS^F and 80 % UTS^F showed a similar course, when related to the normalized number of cycles. A deviation occurred within the last 20 % of fatigue life in form of an abrupt rise of the curve. The specimen tested at 85 % UTS^F displayed a higher amount of damage initiated at an early stage of fatigue life, compared to the specimens

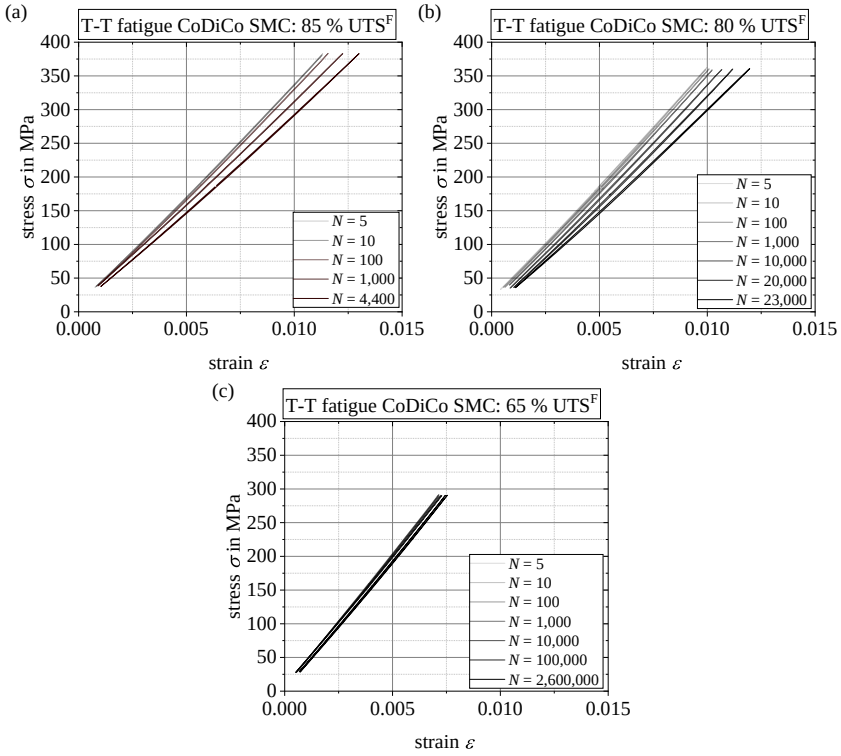

Figure 5.30: Hysteresis loops of CoDiCo SMC specimens under tension-tension fatigue load obtained at (a) 85 % (N_f = 4,524) , (b) 80 % (N_f = 23,306) and (c) 65 % UTS^F (runout), respectively.

tested at lower stresses. For CoDiCo SMC, the relative stiffness loss during fatigue was smaller compared to DiCo SMC throughout most of the specimens' fatigue lives. Comparing Figure 5.32 and Figure 5.13, DiCo SMC specimens lost between 11 % and 14 % of their initial stiffness after 90 % of their fatigue life, while the corresponding stiffness loss for most CoDiCo SMC specimens was between 5 % and 9 % in the same stage of fatigue life.

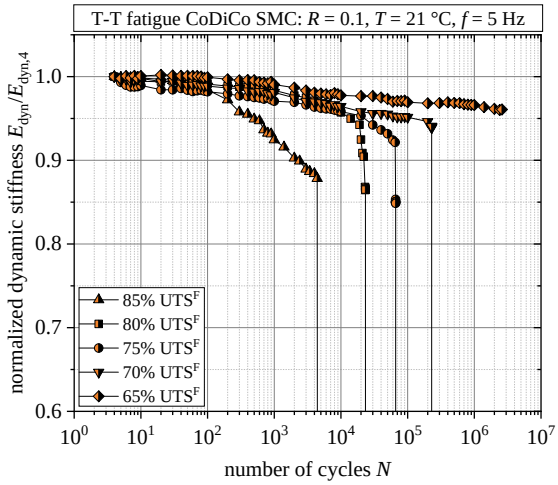

Figure 5.31: Normalized dynamic stiffness of CoDiCo SMC under tension-tension fatigue load; 100 % UTS^F $\hat{=}$ 456 MPa, $\bar{E}_{dyn,4}$ = 36.48 GPa (μ = 1.9 GPa).

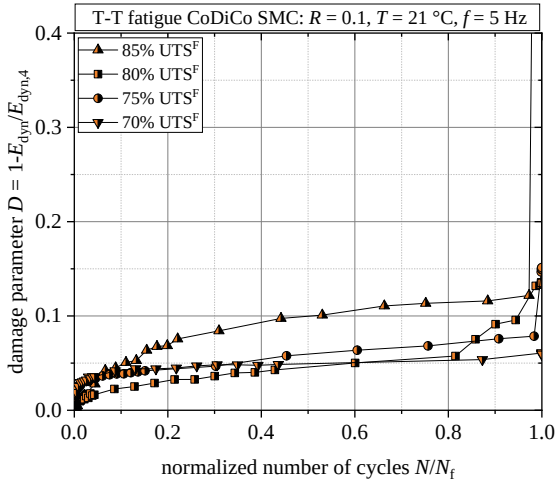

Figure 5.32: Damage parameter of CoDiCo SMC obtained under tension-tension fatigue load; 100 % UTS^F $\hat{=}$ 456 MPa, $\bar{E}_{dyn,4}$ = 36.48 GPa (μ = 1.9 GPa).

Damage evolution

Microscopic images obtained after different numbers of cycles during interrupted fatigue tests are presented in Figure 5.33 for a CoDiCo SMC specimen that was tested at 75 % UTS^F. Within the observed section, the first damage occurred after 100 cycles in the form of carbon fiber fracture. This damage was limited to a region close to the specimen edge. Further cyclic loading caused evolution of matrix cracks (marked by filled arrows) and growing delamination around the broken fibers (marked by the hollow arrow). After 10^4 cycles, the specimen lost approximately 4.5 % of its initial stiffness. A large stiffness drop appeared in the following load step. After 10^5 cycles, pseudo-delamination (marked by hollow arrows) connecting the matrix cracks was observed.

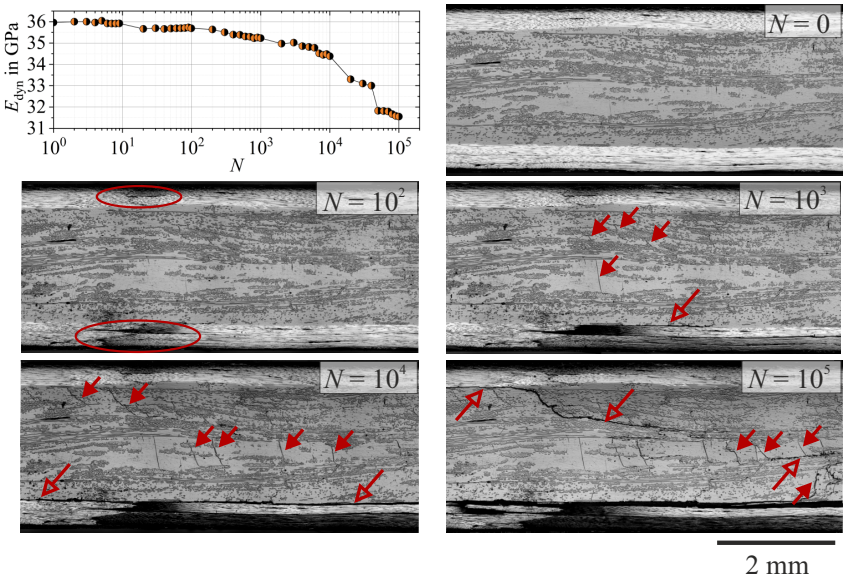

Figure 5.33: Small section of the edge of a CoDiCo SMC specimen tested at 75 % UTS^F after different numbers of cycles. Filled arrows indicate matrix cracks, hollow arrows indicate pseudo-delamination and ellipses mark carbon fiber fracture.

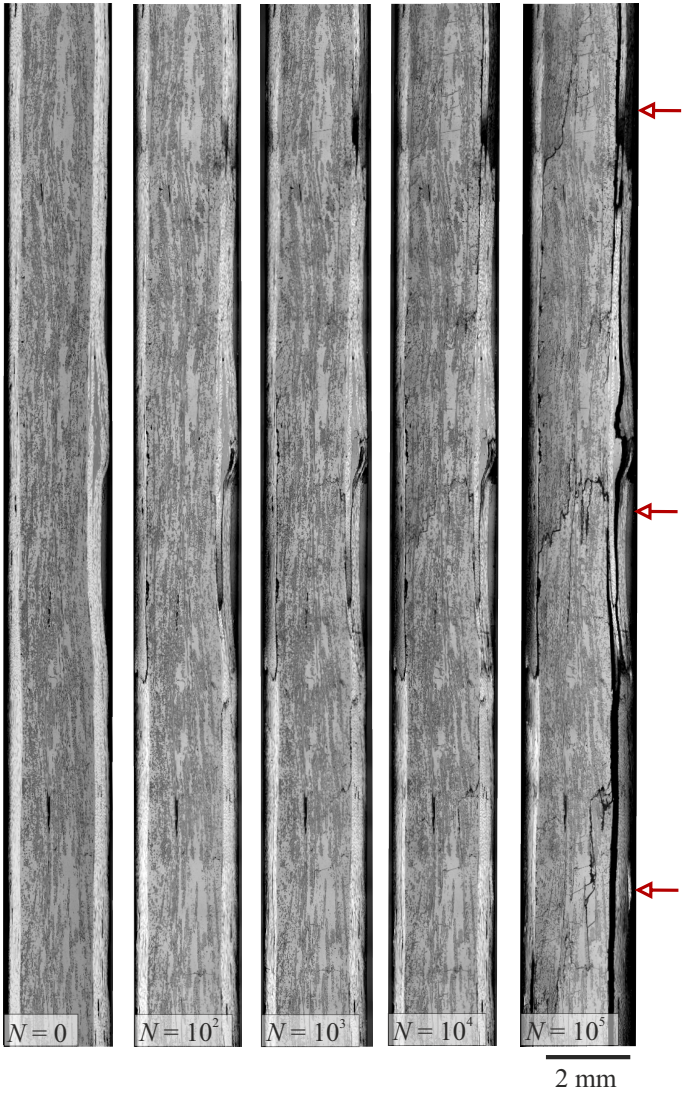

Figure 5.34: Edge of a CoDiCo SMC specimen tested at 75 % UTS^F after different numbers of cycles. Hollow arrows indicate regions in which cracks connect across the entire thickness.

Such connected crack networks were detected at various locations across the entire specimen length, as can be seen from Figure 5.34, which depicts a larger section of the same specimen after different numbers of cycles. The specimen failed after four more cycles outside the gauge length. The location of final failure is shown in Figure 5.35. Final failure was characterized by fiber bundle pull-out and a large amount of pseudo-delamination. Furthermore, parts of the DiCo SMC ply were broken off.

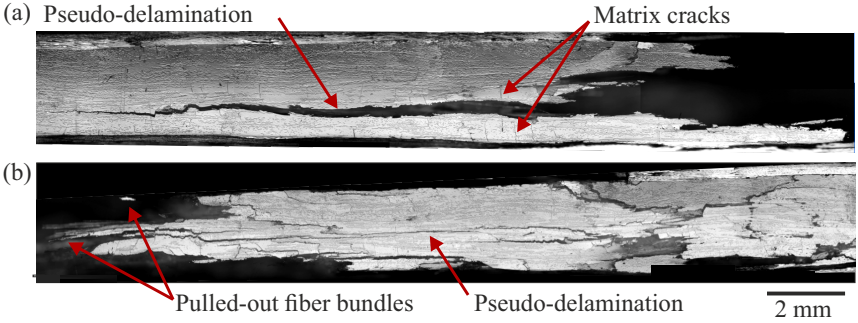

Figure 5.35: Microscopic image of (a) the upper and (b) the lower half of a CoDiCo SMC specimen tested at 75 % UTS^F showing the location of final failure.

The weighted crack length in the DiCo SMC ply was assessed at both specimen edges within the gauge length of the extensometer. The results are shown in Figure 5.36 along with the damage parameter derived from the stiffness degradation curve shown in Figure 5.33. The weighted crack length showed a similar development compared to DiCo SMC (Figure 5.16).

The conversion factor between damage parameter and the weighted crack length is given in Figure 5.37a, in comparison to the corresponding results determined for DiCo SMC (cf. Figure 5.37). The conversion factor was below 0.08 mm and thus lower than the observed values obtained DiCo SMC up to 10^4 cycles. The factor increased to 1.4 mm at 10^5 cycles after the drop in the stiffness degradation curve occurred, which was a result of local failure and delamination of the Co SMC ply. Considering the absolute stiffness loss in Figure 5.37b, the conversion factor was

within the range of the values determined for DiCo SMC up to a cycle number of 10^4 and exceeded those at 10^5, after local failure of the Co SMC ply occurred.

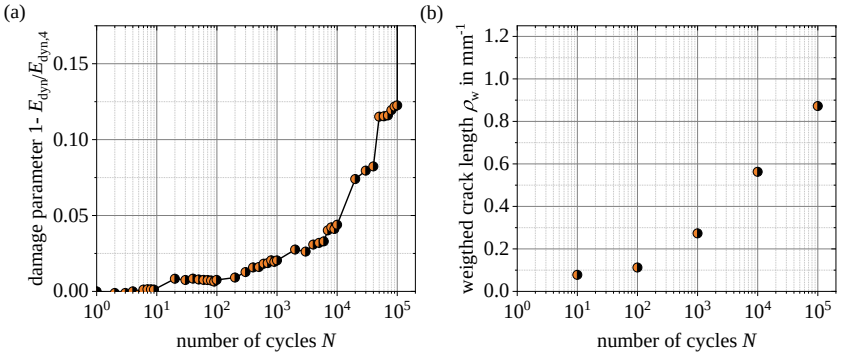

Figure 5.36: (a) Damage parameter of a CoDiCo SMC specimen tested at 75 % UTS^F and (b) weighted crack density in the DiCo SMC ply determined from both specimen edges within the measuring length of the extensometer after different numbers of cycles.

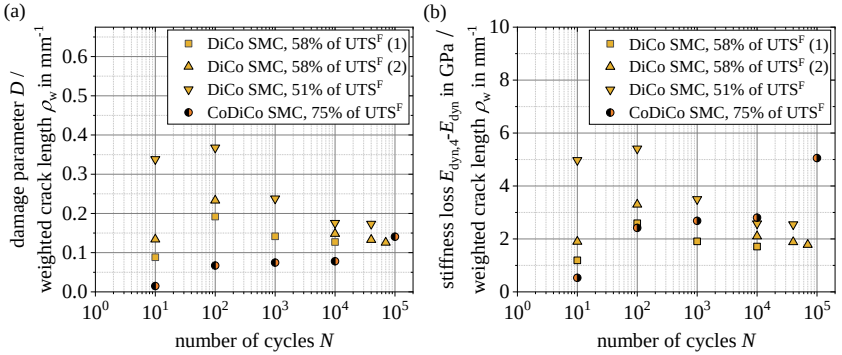

Figure 5.37: Correlation factor between (a) damage parameter and weighted crack length and (b) absolute stiffness loss and weighted crack length for a CoDiCo SMC and different DiCo SMC specimens.

IR thermography analysis

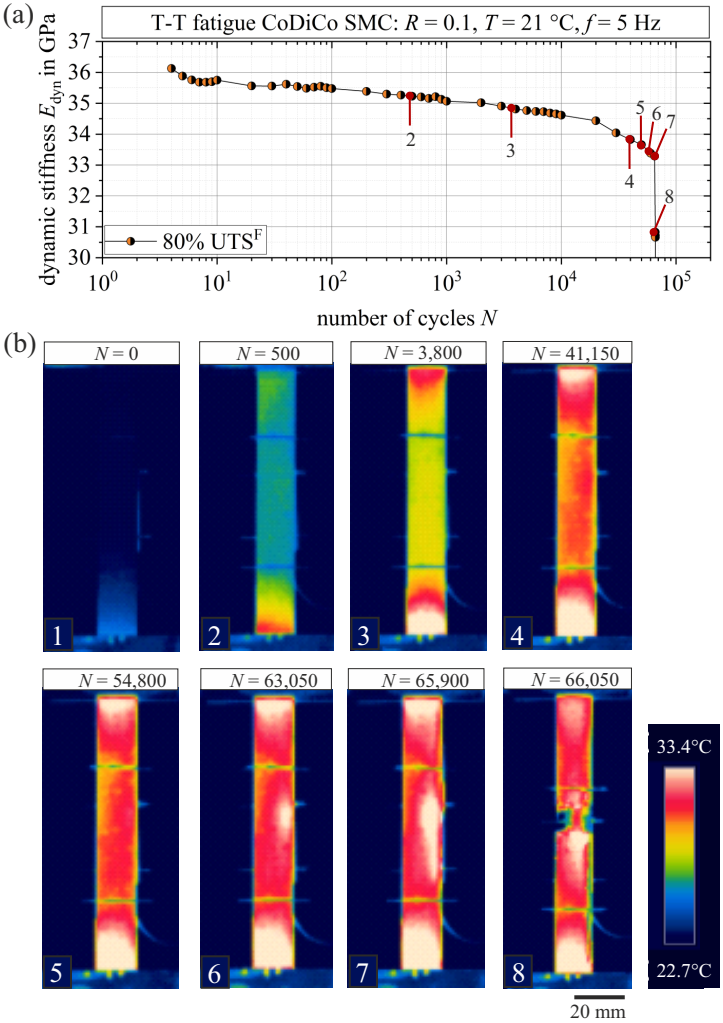

Figure 5.38: (a) Stiffness degradation curve and (b) IR images of a CoDiCo SMC specimen captured during a tension-tension fatigue test at 80 % UTS^F after different numbers of cycles.

Figure 5.38b illustrates the temperature evolution in a representative CoDiCo SMC specimen over the number of cycles. Images were captured at the cycles marked in the stiffness degradation curve (Figure 5.38a). The evolution of temperature is shown in Figure 5.39b along the line in Figure 5.39a. The temperature increase was higher and more homogenous over the specimen length for a longer duration compared to DiCo SMC specimens (Figure 5.20). Localization occurred no earlier than after roughly 3,000 cycles prior to final failure.

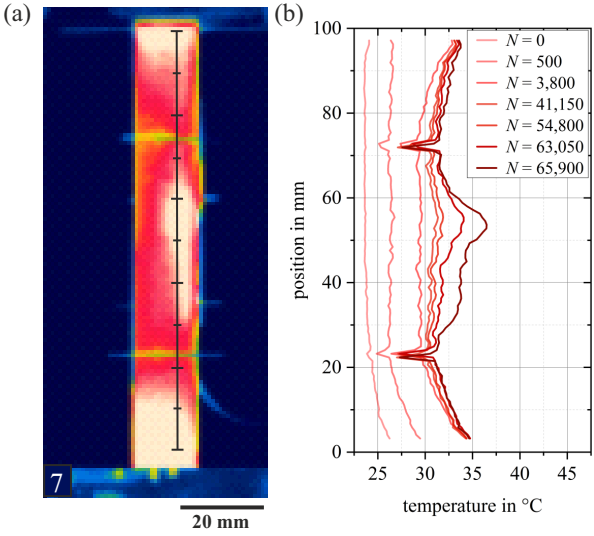

Figure 5.39: (a) CoDiCo SMC specimen tested at 80 % UTS^F marked with a line, along which the temperature data was extracted and (b) temperature profile over specimen length after different numbers of cycles.

5.1.2.5 Tension-tension fatigue behavior of CoDiCo$^{0/90}$ SMC

Stress-life data

The S-N data of CoDiCo$^{0/90}$ SMC specimens is presented in Figure 5.40. Failure due to fatigue occurred at stresses between approximately 194 MPa and 344 MPa, which corresponds to 85 % UTS^{F} and 48 % UTS^{F}, respectively. Two specimens tested at 194 MPa did not fail within the considered number of cycles. Above 344 MPa, all specimens failed immediately. At 40 % UTS^{F}, no failure occurred due to fatigue.

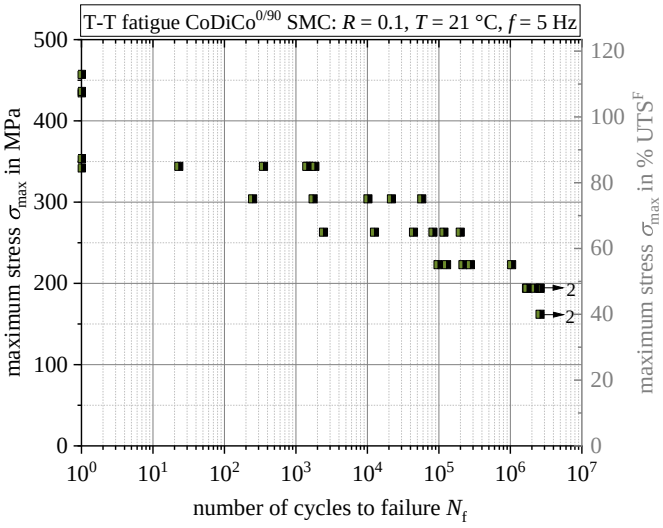

Figure 5.40: S-N data of CoDiCo$^{0/90}$ SMC under tension-tension fatigue load.

Post-mortem analysis of macroscopic damage

Analogous to the observations under monotonic tensile load, specimens that were tested at 75 % UTS^{F} showed large scale delaminations of the 0° carbon fiber plies,

whereas the interface between the 90° ply and DiCo SMC ply remained largely intact (Figure 5.41). Fiber fracture occurred at different positions across the entire specimen length and not exclusively alongside to the end tabs, as observed for the monotonically loaded specimens. The density of splitting cracks too was higher compared to the monotonically loaded specimens.

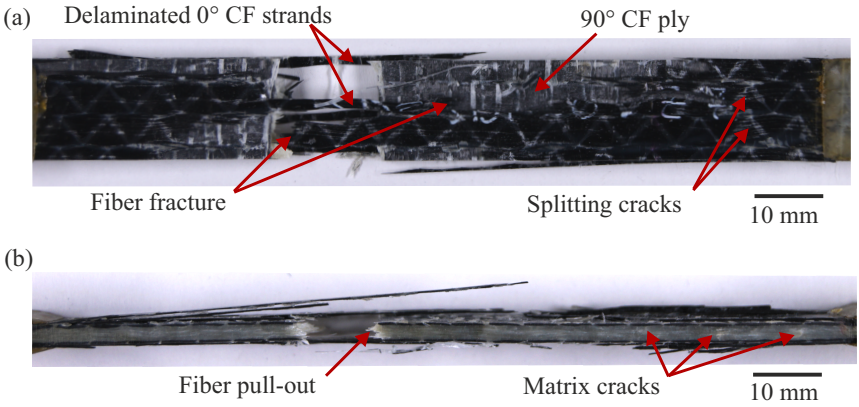

Figure 5.41: (a) Topview and (b) sideview of a CoDiCo$^{0/90}$ SMC specimen loaded at 75 % UTS^{F} after final failure.

For specimens tested at lower maximum stresses, damage was more localized. The specimen presented in Figure 5.42 was tested at 55 % UTS^{F}. Fiber fracture, splitting cracks and delamination between the 0° and the 90° plies occurred in the region of final failure. In contrast, only few splitting cracks were observed across the rest of the specimen length together with partial delamination of a misaligned 0° carbon fiber tows at the specimen edge.

Figure 5.43 depicts a runout specimen tested at 40 % UTS^{F}. Delicate splitting cracks were observed across the entire 0° carbon fiber ply. Several cracks in the 90° ply could be detected in the region where the 0° strands were pushed apart due to the material flow during manufacturing.

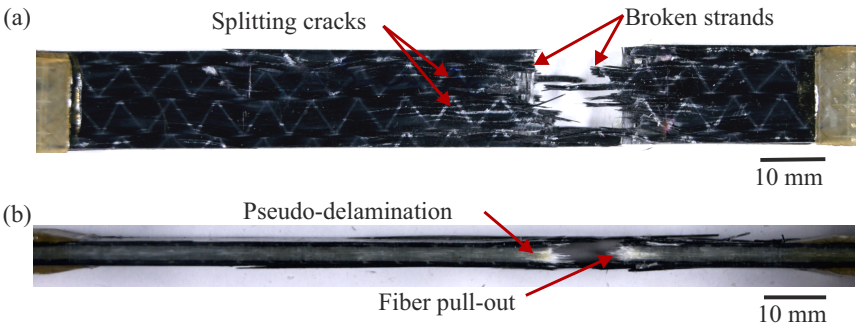

Figure 5.42: (a) Topview and (b) sideview of a CoDiCo$^{0/90}$ SMC specimen loaded at 55 % UTS^{F} after final failure.

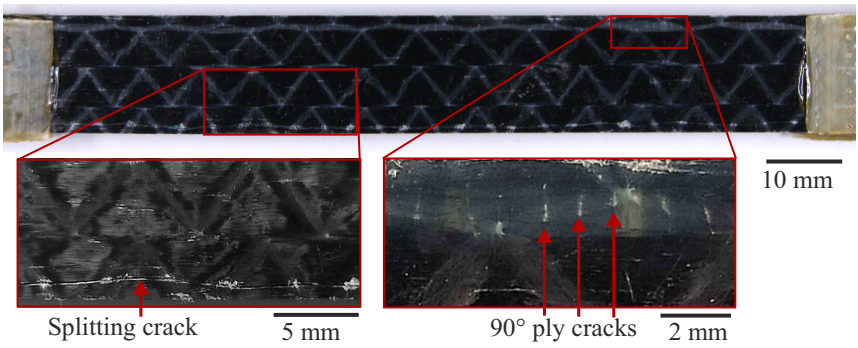

Figure 5.43: CoDiCo$^{0/90}$ SMC specimen loaded at 40 % UTS^{F} after $2.6 \cdot 10^{6}$ cycles.

Stress-strain data

Generally, the evolution of the hysteresis loops was comparable to CoDiCo SMC with a 0° carbon fiber reinforcement only. The shift of the hysteresis loops was negligibly small in the low cycle fatigue range (Figure 5.44a) and more pronounced in the high cycle fatigue range (Figure 5.44b). However, independent of the applied stress, less than 0.1 % strain was detected. For the runout specimens, a slightly stronger shift was observed, compared to that of CoDiCo SMC (Figure 5.44c).

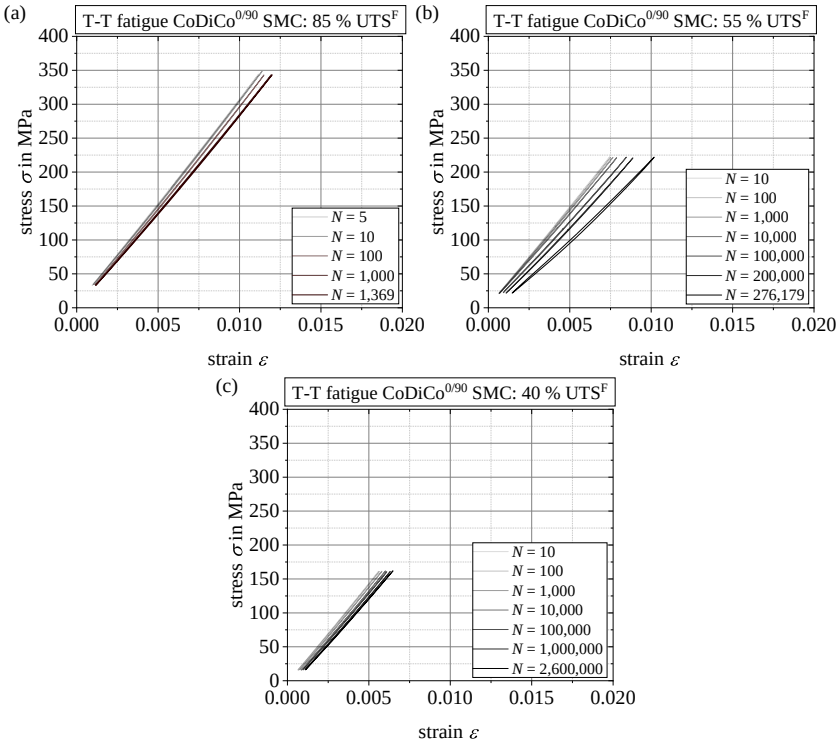

Figure 5.44: Hysteresis loops of CoDiCo$^{0/90}$ SMC under tension-tension fatigue load obtained at (a) 85 % (N_f = 1,419), (b) 55 % (N_f = 276,229) and (c) 40 % UTS^{F} (runout), respectively.

Stiffness degradation

The stiffness degradation behavior (Figure 5.45) was comparable the previously described CoDiCo SMC configuration in Figure 5.31 with approximately 1 % to 1.5 % stiffness loss per decade of cycles. A different behavior was observed in the last phase of fatigue life, where the stiffness decrease was less abrupt. The overall stiffness loss prior to final failure was higher compared to the other CoDiCo SMC configuration. The lower the applied load was, the higher the overall stiffness loss.

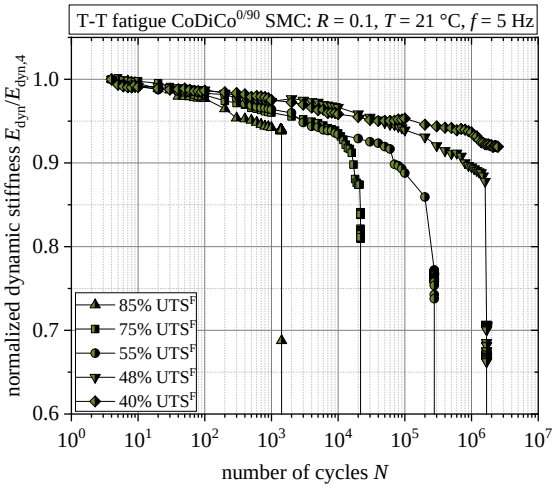

Figure 5.45: Normalized dynamic stiffness of CoDiCo$^{0/90}$ SMC under tension-tension fatigue load; 100 % UTS^{F} ≙ 405 MPa, $\bar{E}_{dyn,4}$ = 30.19 GPa (μ = 1.0 GPa).

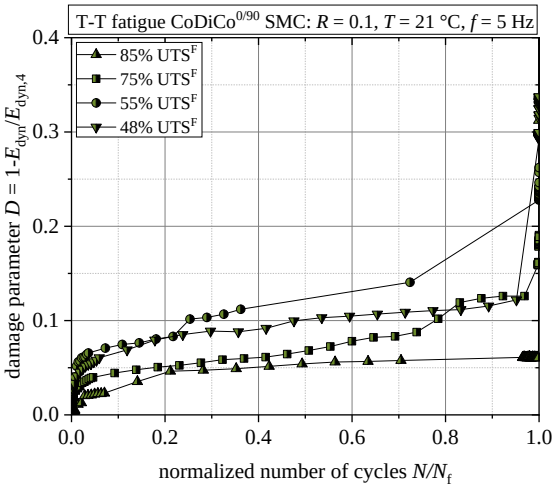

Figure 5.46: Damage parameter of CoDiCo$^{0/90}$ SMC obtained under tension-tension fatigue load; 100 % UTS^{F} ≙ 405 MPa, $\bar{E}_{dyn,4}$ = 30.19 GPa (μ = 1.0 GPa).

Stiffness loss greater than 12 % on average was determined at 90 % of fatigue life (Figure 5.46). A higher applied load tended to result in separation of the specimens after exhibiting a lower amount of damage. For the specimens tested at 55 % UTS^F and 75 % UTS^F, a small jump of the curve led to a deviant behavior.

Damage evolution

A $CoDiCo^{0/90}$ SMC specimen tested at 55 % UTS^F depicted in Figure 5.47 shows several ply cracks in the 90° Co SMC ply, then could be observed after as little as 10 cycles. These cracks grew into the DiCo SMC ply with additional loading, which can be seen in more detail in Figure 5.47, showing two magnified sections, that are marked by a green and a blue box. Furthermore, these cracks initiated delamination between the 0° and the 90° Co SMC ply, highlighted by hollow arrows. After 10^5 cycles, one crack grew far into the middle of the DiCo SMC ply and finally connected with another crack network coming from the other side of the specimen, which led to its separation. The number of matrix cracks that formed within the DiCo SMC ply independently of the cracks in the 90° plies, was small compared to the crack density that was observed in DiCo SMC and CoDiCo SMC specimens.

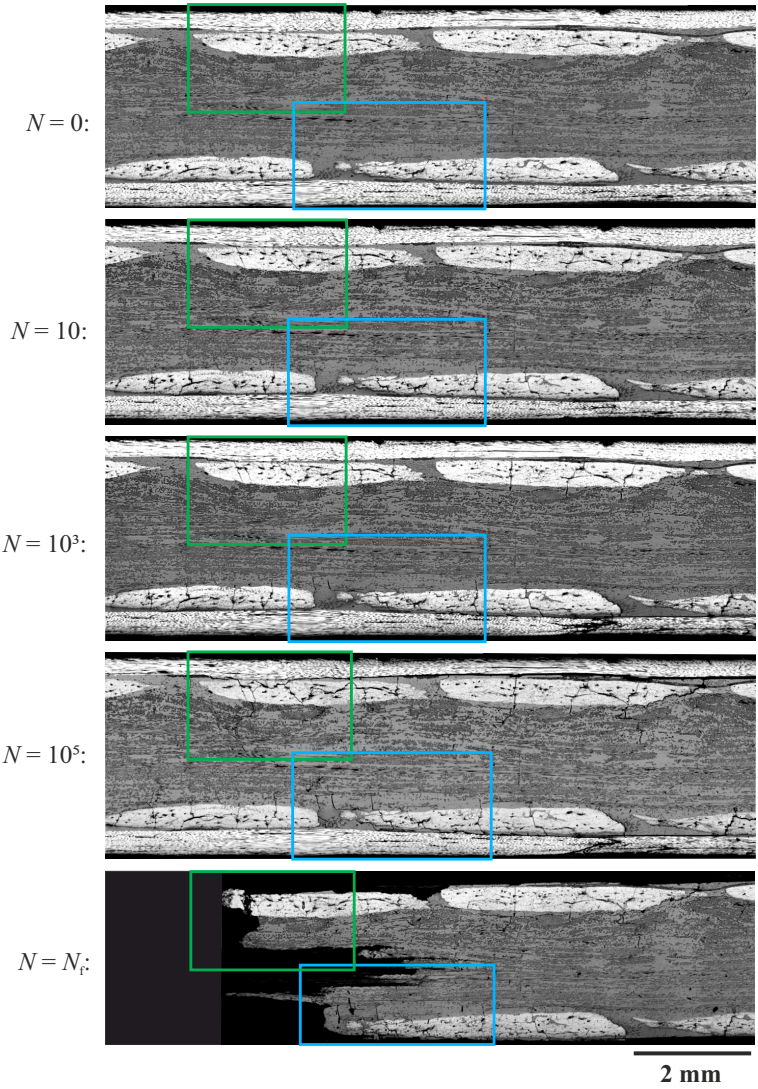

Figure 5.47: Edge of a CoDiCo$^{0/90}$ SMC specimen that was tested at 55 % UTS^{F} after different numbers of cycles.

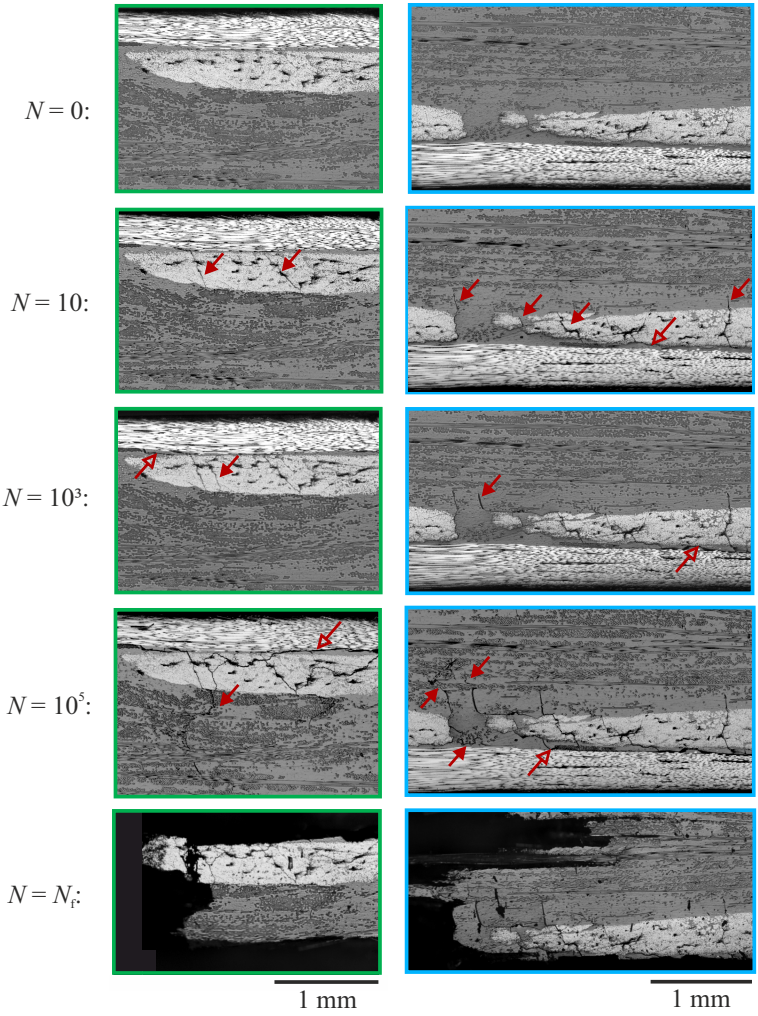

Figure 5.48: Magnified view on the damage mechanisms in a CoDiCo$^{0/90}$ SMC specimen tested at 55 % UTS^{F} after different numbers of cycles.

5.2 Mechanical properties and damage behavior under application-related loading

5.2.1 Flexural properties

5.2.1.1 Ultimate flexural strength

Results of the bending tests at quasi-static and fatigue strain rate are summarized in Table 5.3. In terms of CoDiCo SMC, only the configuration with a 0° carbon fiber reinforcement was examined under application-related loading. Increasing the strain rate led to an enhanced flexural strength of Co SMC, DiCo SMC and CoDiCo SMC by 3 % 11 % and 10 %, respectively.

Table 5.3: Ultimate flexural strength of all analyzed materials determined at quasi-static strain rate UFS^S (crosshead velocity of 2 mm/min for Co SMC and DiCo SMC and 5 mm/min for CoDiCo SMC) and fatigue strain rate UFS^F (crosshead velocity of 90 mm/s for Co SMC and DiCo SMC and 180 mm/s for CoDiCo SMC). Failure was defined by a force drop of >80 %.

	UFS^S			UFS^F		
	$\bar{x}$ in MPa	μ in MPa	CV in %	$\bar{x}$ in MPa	μ in MPa	CV in %
DiCo	399	47	11.9	425	30	7.1
Co	930	91	9.8	962	60	6.2
CoDiCo	616	65	10.6	678	21	3.1

5.2.2 Bending fatigue behavior

5.2.2.1 Bending fatigue test parameters

Table 5.4 summarizes the stress levels employed for the bending fatigue tests. The stated values correspond to the maximum homogenized stresses, which were

calculated by 4.9, neglecting the macroscopically inhomogenous microstructure. Of note, these values do not correspond to the actual local stresses within the plies, but allow for a comparison of the different material systems.

Table 5.4: Investigated stress levels for all analyzed materials in terms of maximum homogenized stress both in % UFS^F and in MPa.

DiCo SMC		Co SMC		CoDiCo SMC	
applied load in		applied load in		applied load in	
% UFS^F	MPa	% UFS^F	MPa	% UFS^F	MPa
69	295	80	769	90	611
61	261	70	673	85	577
55	232	60	577	80	543
47	199	50	481	75	509
39	166			70	475
31	133				

5.2.2.2 Bending fatigue behavior of DiCo SMC

Stress-life data

The fatigue life diagram of DiCo SMC is shown in Figure 5.49. Failure due to cyclic loading was defined by a stiffness degradation of at least 80 % and occurred in the stress range between 166 MPa and 295 MPa. Depending on the load level, scatter in the range of one to three decades of cycles was observed, which is comparable to the range of scatter in tension-tension fatigue tests. A first runout was obtained at a maximum stress of 166 MPa, which corresponds to approximately 39 % UFS^F. At 133 MPa (31 % UFS^F), no specimens failed with the conducted range of $2.6 \cdot 10^6$ cycles.

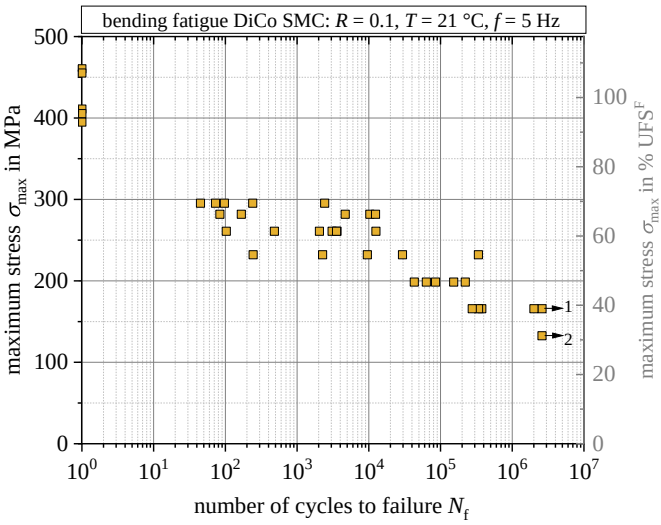

Figure 5.49: S-N data of DiCo SMC under cyclic bending.

Post-mortem damage analysis

The DiCo SMC specimen shown in Figure 5.50 was tested at 47 % UFS^F and failed after approximately $1.5 \cdot 10^5$ cycles. The location of final failure was characterized by matrix cracking, pseudo-delamination and fiber bundle pull-out on the tension-loaded side. Several transverse matrix cracks were observed outside of the site of final failure, that were not or barely present in monotonically tested specimens. The compression-loaded side showed only a small amount of damage in the form of matrix-bundle separation on the surface. The whitish color identified the pseudo-delaminated area. The damage pattern was similar for all specimens tested at different loads.

Figure 5.51 shows a specimen that was tested at 31 % UFS^F and did not fail within $2.6 \cdot 10^6$ cycles. While no signs of damage were evident on the compression loaded side, matrix cracks and pseudo-delamination spreading from the specimen edges were observed on the tension-loaded side.

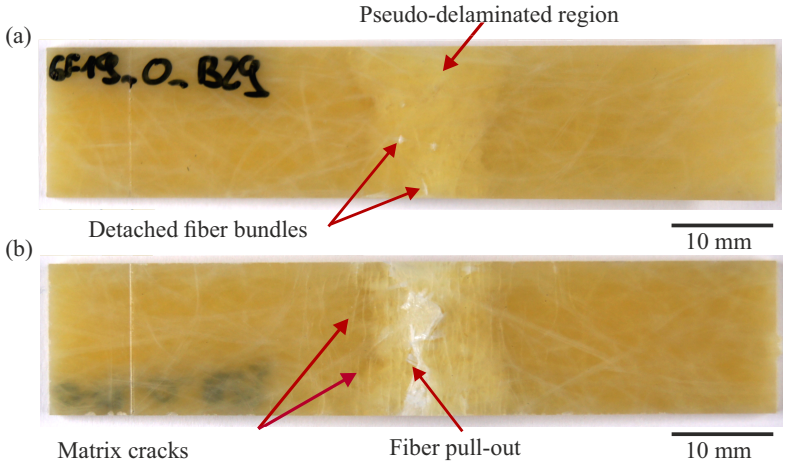

Figure 5.50: (a) Compression-loaded side and (b) tension-loaded side of a DiCo SMC specimen tested under bending fatigue load at 47 % UFS^F after final failure.

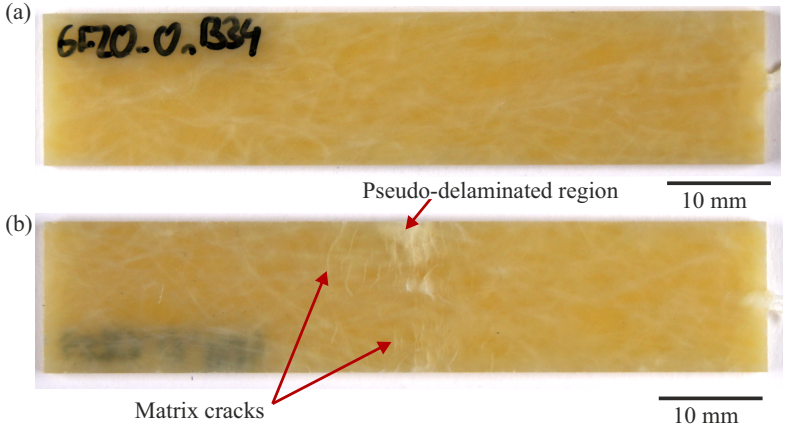

Figure 5.51: (a) Compression-loaded side and (b) tension-loaded side of a DiCo SMC specimen tested under bending fatigue load at 31 % UFS^F after $2.6 \cdot 10^6$ cycles.

Stiffness degradation

The normalized dynamic modulus of six DiCo SMC specimens, that were tested at different maximum stresses, is presented in Figure 5.52. The specimens were chosen to be representative for the analyzed stress level, showing an average fatigue life compared to the other specimens tested at the same load.

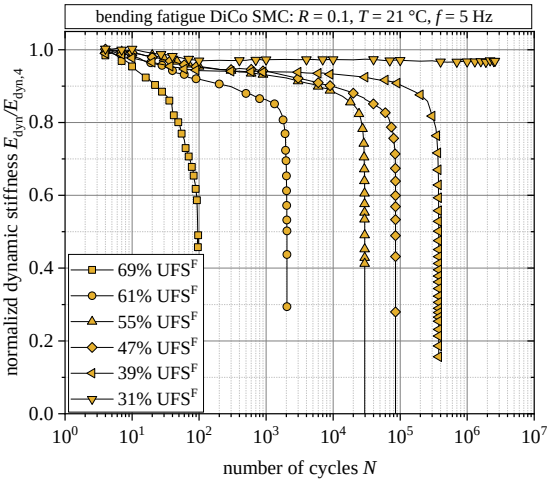

Figure 5.52: Normalized dynamic stiffness of DiCo SMC under cyclic bending load; 100% $UFS^F \mathrel{\hat{=}} 425$ MPa, $\bar{E}_{dyn,4} = 12.6$ GPa ($\mu = 1.6$ GPa).

The stiffness degradation curves could each be categorized into three phases. Within the first 100 cycles, stiffness strongly decreased by 3 % to 8 % at loads between 39 % UFS^F and 61 % UFS^F. The stiffness degradation was the more pronounced, the higher the applied load. After 100 cycles, the degradation curves flattened and stiffness degradation progressed at a lower rate, that was dependent on the applied load. The third phase was characterized by another continuous increase of the degradation rate prior to final failure of the specimens. In case of the specimen tested at 31 % UFS^F, almost no stiffness degradation was observed

after 100 cycles. For the specimen tested at 69 % UFS^F, no definite distinction between the different phases of fatigue life was possible.

Figure 5.53 shows the stiffness degradation of the same specimens expressed in terms of the damage parameter over the normalized number of cycles. The curves representing the specimens tested at loads between 61 % UFS^F and 39 % UFS^F showed a similar progression. After 90 % of fatigue life, the specimens lost more than 20 % of their initial stiffness. A deviating behavior was only seen for the specimen tested at 69 % UFS^F.

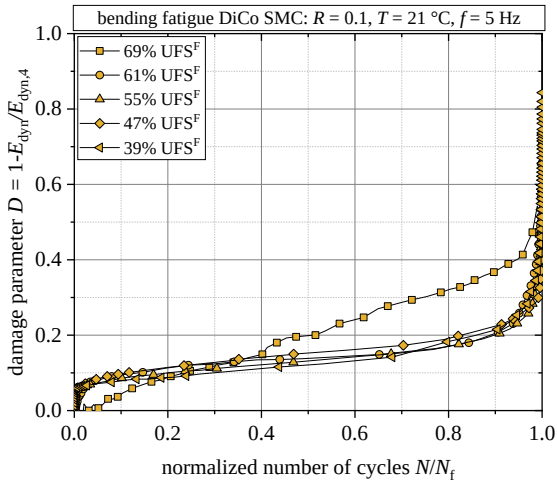

Figure 5.53: Damage parameter of DiCo SMC under cyclic bending load; 100% $UFS^F \mathrel{\hat{=}} 425$ MPa, $\bar{E}_{dyn,4} = 12.6$ GPa ($\mu = 1.6$ GPa).

5.2.2.3 Bending fatigue behavior of Co SMC

Stress-life data

Figure 5.54 shows the fatigue life diagram of Co SMC. Fatigue strength decreased roughly by 100 MPa per decade of cycles, on average. Scatter was in the range of

approximately three decades of cycles for all tested stress levels. Five out of six specimens tested at 577 MPa (60 % UFS^F), failed within $2.6 \cdot 10^6$ cycles, whereas all specimens tested at a maximum stress of 481 MPa (50 % UFS^F) were runouts.

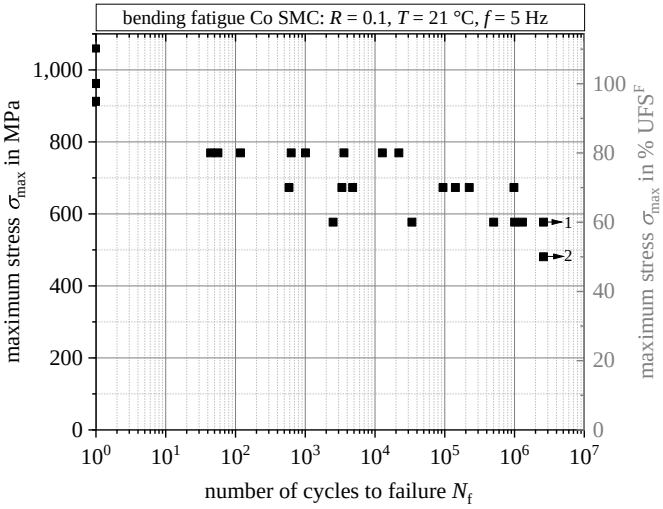

Figure 5.54: S-N data of Co SMC under cyclic bending.

Post-mortem damage analysis

Damage under cyclic bending load started on the compression-loaded side, which is depicted on the runout specimen in Figure 5.55, which shows fiber fracture in the upper ply, where the loading nose applied the force. The tension-loaded side showed no signs of damage. Final failure came with fiber fracture on the tension-loaded side along with delamination (Figure 5.56).

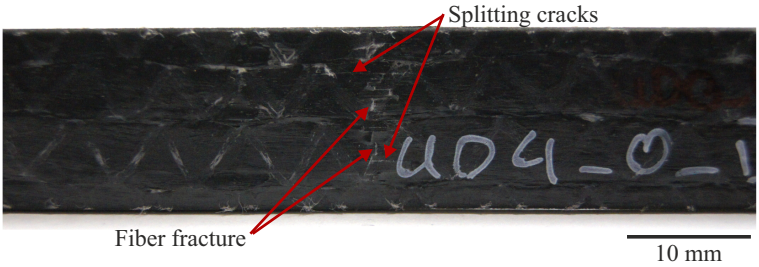

Figure 5.55: Topview of a Co SMC specimen (runout) tested at 50 % UFS^F after $2.6 \cdot 10^6$ cycles.

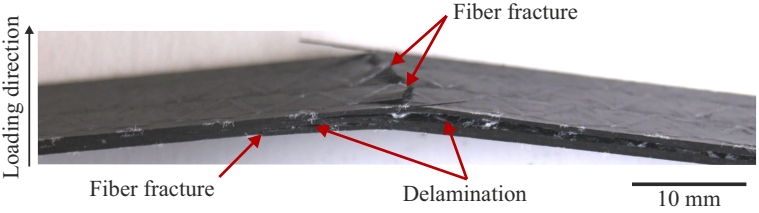

Figure 5.56: Co SMC specimen tested at 60 % UFS^F after final failure.

Stiffness degradation

In comparison to DiCo SMC, the overall loss of stiffness during cyclic loading was comparatively small (Figure 5.57). It was approximately 2 % to 4 % prior to a spontaneous drop in the degradation curve that led to a further stiffness reduction at an increased degradation rate and ultimately resulted in final failure. Such drops originated from fiber fracture on the compression-loaded side of the specimen. The overall stiffness loss before final failure was higher in specimens that were tested at lower stresses. For the runout specimen, that was tested at 50 % UFS^F, no significant decrease of the dynamic stiffness was determined for up to $2.6 \cdot 10^6$ cycles.

In terms of the damage parameter over the normalized fatigue life (Figure 5.58), the curves were comparable only at the beginning of the fatigue life. Over the subsequent course of loading, jumps of the damage curves appeared spontaneously at various relative fatigue lives.

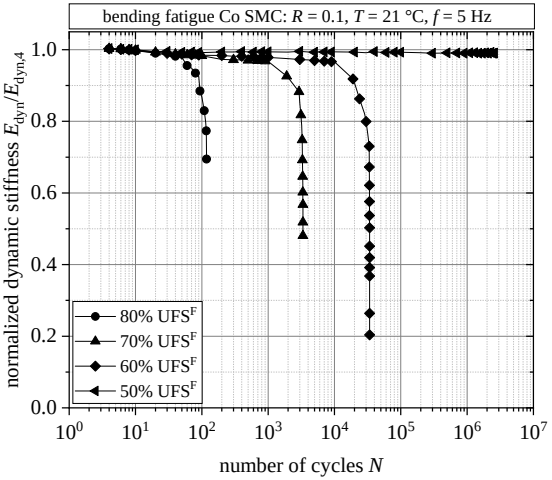

Figure 5.57: Normalized dynamic stiffness of Co SMC under cyclic bending load; 100% UFS^F ≙ 932 MPa, $\bar{E}_{dyn,4}$ = 72.6 GPa (μ = 1.9 GPa).

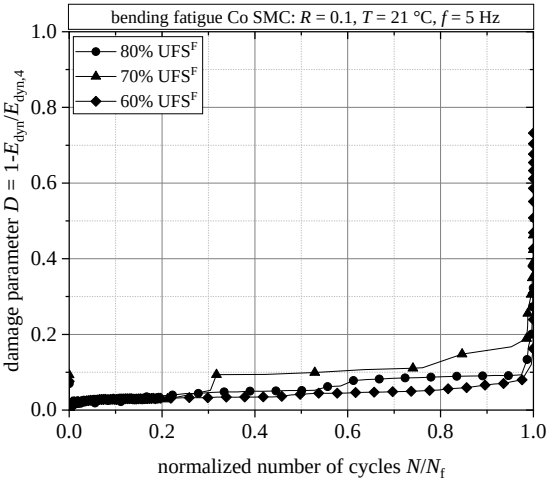

Figure 5.58: Damage parameter of Co SMC under cyclic bending load; 100% UFS^F ≙ 932 MPa, $\bar{E}_{dyn,4}$ = 72.6 GPa (μ = 1.9 GPa).

5.2.2.4 Bending fatigue behavior of CoDiCo SMC

Stress-life data

In the case of CoDiCo SMC, the stress range in which specimens failed due to fatigue, was between 509 MPa and 610 MPa and quite low compared to DiCo SMC and Co SMC (Figure 5.59). Scatter was in the range of up to four decades of cycles and was thus considerably more pronounced compared to DiCo SMC and Co SMC. In terms of the UFS^F, the load level at which all specimens were runouts, was considerably higher with 70 % (475 MPa), which is equal to the approximate fatigue strength determined for Co SMC.

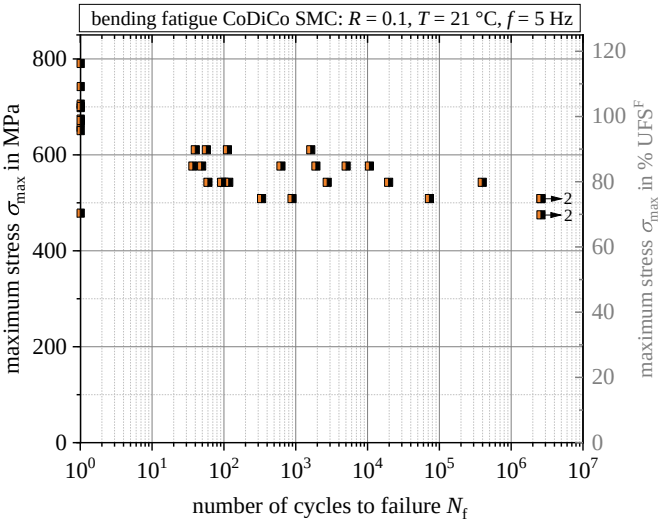

Figure 5.59: S-N data of CoDiCo SMC under cyclic bending.

Stiffness degradation

As shown in Figure 5.60, no significant stiffness degradation was observed during cyclic loading prior to the sudden drops. They were either pronounced and immediately led to final failure if the applied load was high, or the drops were slight and only led to an increased stiffness degradation rate in the case of lower applied loads. In line with DiCo SMC, these drops originated from partial or complete failure of the continuous carbon fiber plies on the compression-loaded side of the specimens. The residual stiffness before final failure amounted to approximately 30 % of the initial stiffness for almost all tested specimens. The initial stiffness degradation rate was the greater, the higher the applied load. In case of the runout specimen tested at 70 % UFS^F, stiffness was reduced by 2.5 % after $7 \cdot 10^5$ cycles before the slope increased again due to a small displacement of the specimen on the lower supports, that was observed during testing.

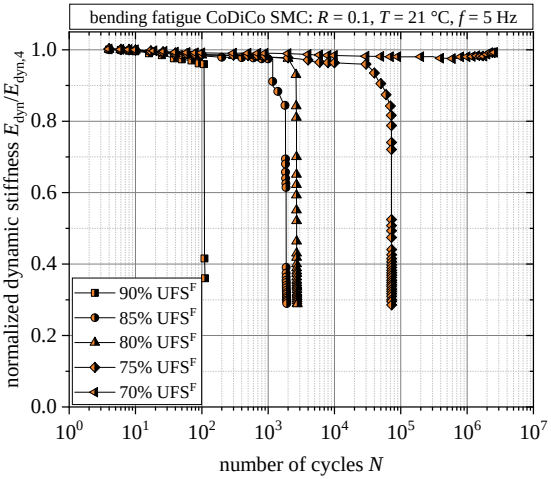

Figure 5.60: Normalized dynamic stiffness of CoDiCo SMC under cyclic bending load; 100% $UFS^F \mathrel{\hat{=}} 678$ MPa, $\bar{E}_{dyn,4} = 50.25$ GPa ($\mu = 1.85$ GPa).

In Figure 5.61, that data is displayed by means of the damage parameter versus the normalized number of cycles to failure. Compared to the results obtained under tension-tension fatigue load, the value of the damage parameter remained close to zero for a long period of fatigue life, before sudden drops appeared at different times during the specimens' fatigue lives, which did not correlate to the applied load.

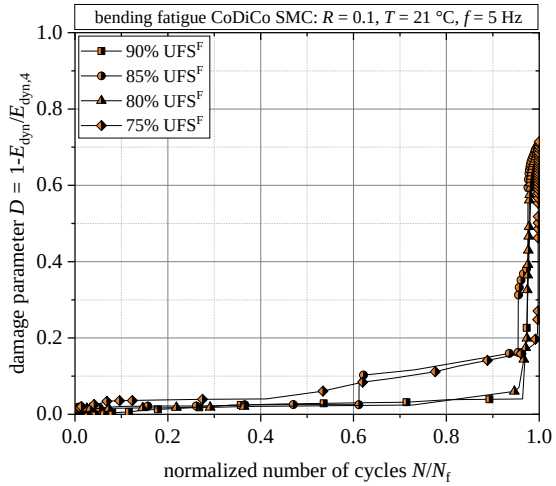

Figure 5.61: Damage parameter of CoDiCo SMC under cyclic bending load; 100% $UFS^F \triangleq 678$ MPa, $\bar{E}_{dyn,4} = 50.25$ GPa ($\mu = 1.85$ GPa).

Damage evolution

Figure 5.62 shows the damage evolution of CoDiCo SMC under bending fatigue load. The specimen depicted was tested at 75 % UFS^F after polishing the edges and the test was interrupted after every decade of cycles for microscopic and macroscopic imaging. The evolution of the dynamic stiffness is displayed at the top of the figure. The damage state is shown at four different positions on the specimen after 1,000 cycles, just when a small stiffness jump was recorded, as

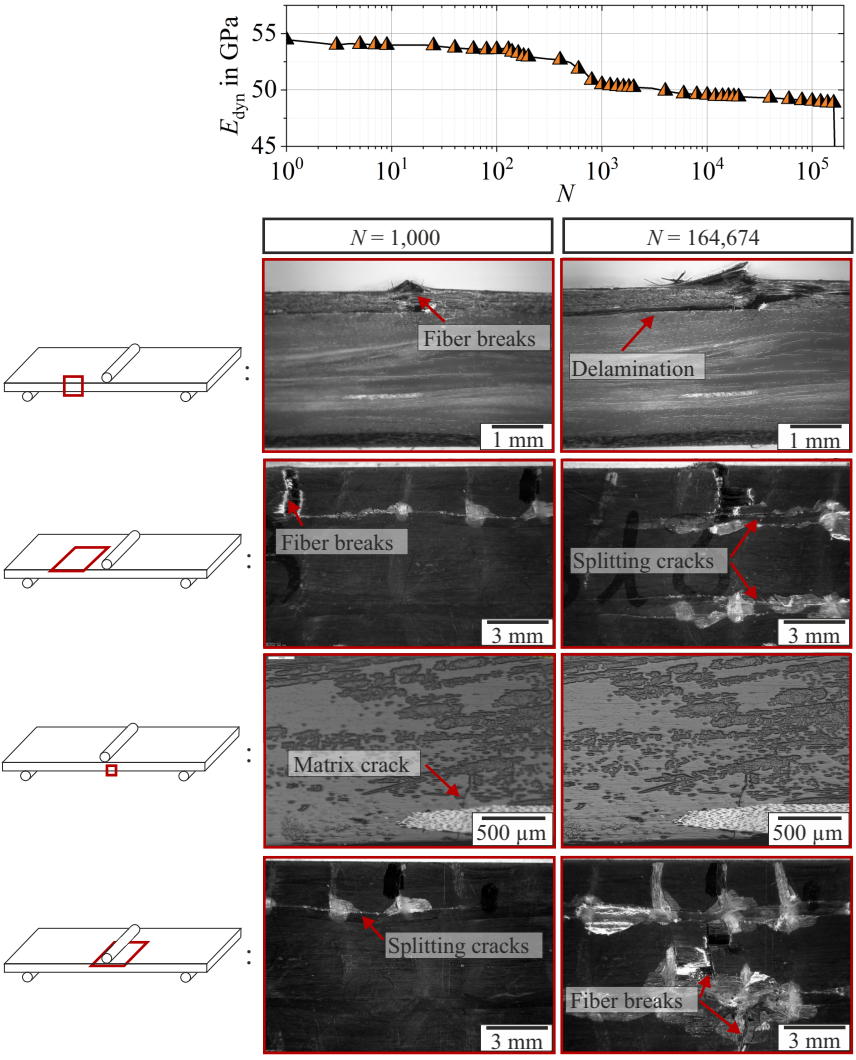

Figure 5.62: Stiffness degradation curve and damage evolution of a CoDiCo SMC specimen tested at 75 % UFS^F under bending fatigue load. The damage pattern is shown at four different positions after 1,000 cycles and 164,674 cycles, respectively.

well as after 164,674 cycles, where a 65 % stiffness drop was observed. After 1,000 cycles, one carbon fiber tow close to the specimen edge broke due to compression 15 mm away from the loading nose, which was accompanied by a large splitting crack and delamination of the tow. A small matrix crack was observed at the same time on the tension-loaded side at the edge of a carbon fiber tow. After 164,674 cycles, the other carbon fiber tows on the compression-loaded side failed close to the loading nose, leading to a pronounced stiffness jump, while the tows on the tension-loaded side remained intact and no growth of the matrix crack on the tension-loaded side was observed. Further loading beyond this point caused fracture of the lower carbon fiber ply as well was pseudo-delamination and fiber bundle pull-out in the DiCo SMC ply, as shown in Figure 5.63.

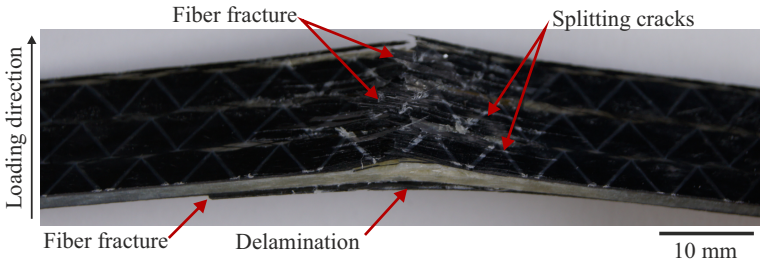

Figure 5.63: CoDiCo SMC specimen tested at 80 % UFS^F after final failure.

5.2.3 Influence of temperature

5.2.3.1 Temperature-dependence of flexural strength

Monotonic bending tests on DiCo SMC and CoDiCo SMC specimens were carried out at -20 °C and 80 °C and at different strain rates, to characterize the influence of temperature on the materials' flexural strength. As shown in Figure 5.64, for DiCo SMC, a temperature increase from 21 °C to 80 °C resulted in a 24 % decrease in average flexural strength at quasi-static strain rate and a 14 % decrease at fatigue strain rate. No significant difference in the flexural strength is observed between specimens tested at -20 °C and 21 °C.

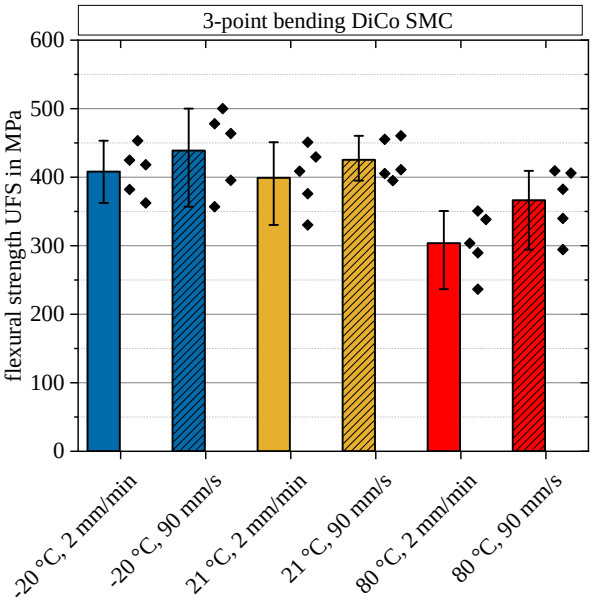

Figure 5.64: Temperature-dependent flexural strength of DiCo SMC at different strain rates.

The influence of temperature on the flexural strength of CoDiCo SMC is shown in Figure 5.65. The average flexural strength decreased by 7 % at quasi-static strain

rate and by 12 % at fatigue strain rate due to a temperature increase from 21 °C to 80 °C. However, since the scatter bars overlap, the difference is not significant. At -20 °C, an increase of 25 % and 14 %, compared to the results at room temperature, was observed at quasi-static and fatigue strain rate, respectively.

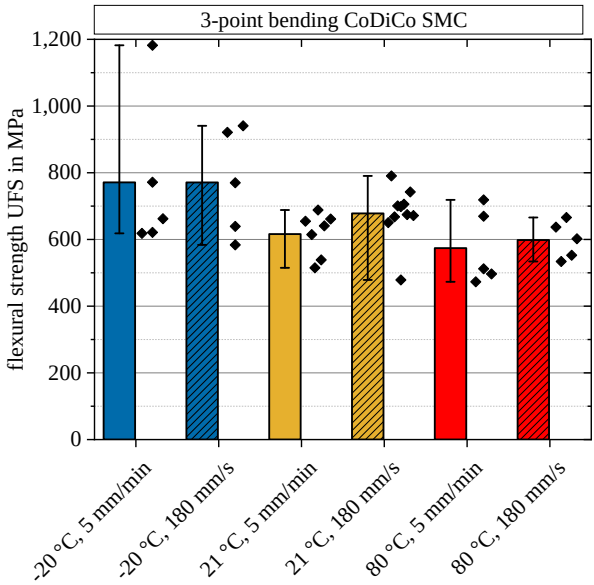

Figure 5.65: Temperature-dependent flexural strength of CoDiCo SMC at different strain rates.

5.2.3.2 Temperature-dependent fatigue properties

Bending fatigue test at -20 °C and 80 °C were carried out to characterize the influence of temperature on the fatigue life of DiCo SMC and CoDiCo SMC. S-N data are summarized in Figure 5.66 and Figure 5.67, respectively. The P-S-N curves for failure probabilities of $P_S = 10\,\%$ and $P_S = 90\,\%$ are displayed to mark the range, in which the data points are located and thus to enable better comparability of the results obtained at different temperatures. Results obtained

at room temperature are included for comparison. Due to the limited capacity of the liquid nitrogen container, the temperature of -20 °C could be kept constant for up to 20 hours, which corresponds to around $3.6 \cdot 10^5$ cycles. Specimens that did not fail within this time frame were marked as runouts. DiCo SMC specimens tended to have a higher fatigue life when tested at lower temperatures. While data obtained at 80 °C was still in the scatter range of that obtained at room temperature, the scatter range of S-N data at -20 °C was clearly beyond the fatigue lives of specimens tested at 80 °C. The fatigue strength was comparable for specimens tested at room temperature and 80 °C.

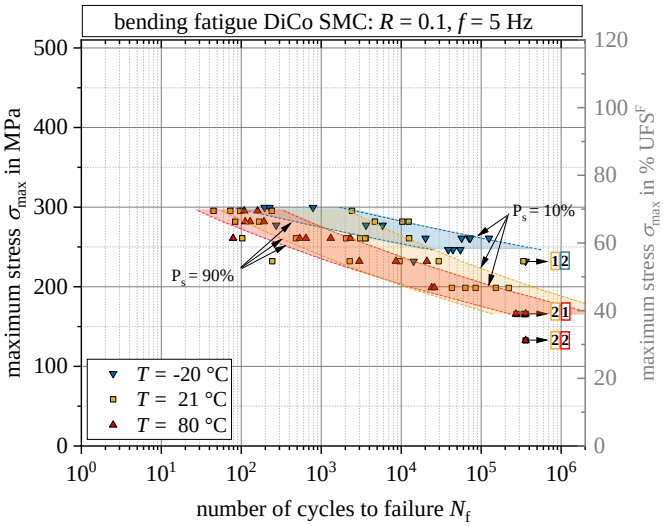

Figure 5.66: S-N data of DiCo SMC under bending fatigue load at different temperatures together with corresponding P-S-N curves for failure probabilities of $P_S = 10\,\%$ and $P_S = 90\,\%$.

The influence of temperature on the fatigue life was much more pronounced for CoDiCo SMC than for DiCo SMC. The stress range of the results obtained at -20 °C was approximately 100 MPa higher than at room temperature. Likewise, the load at which no failure occurred within the number of cycles tested, was approximately 100 MPa higher. Comparing the results at room temperature with

those obtained at 80 °C, the effect was even more pronounced. At maximum applied stresses that went down to 407 MPa, which is 68 MPa below the fatigue strength of CoDiCo SMC at room temperature, almost all specimens failed in the low cycle fatigue range within less than 10^4 cycles. At a maximum stress of 305 MPa, both specimens tested at 80 °C withstood the conducted $3.6 \cdot 10^5$ cycles. This is approximately 270 MPa below the stress, at which all specimens tested at -20 °C withstood the same number of cycles.

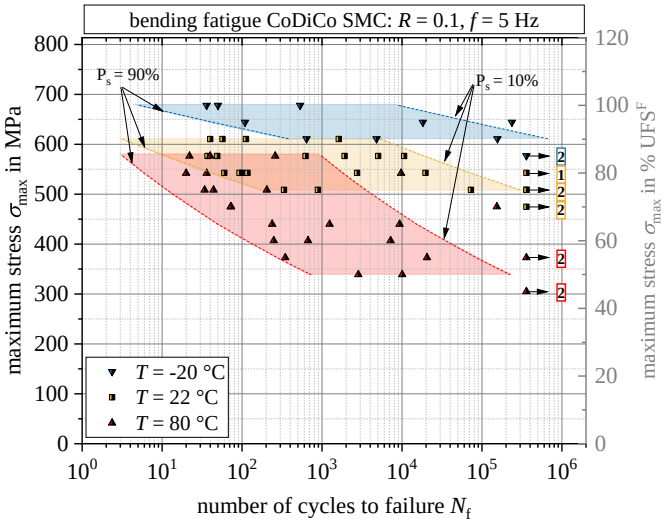

Figure 5.67: S-N data of CoDiCo SMC under bending fatigue load at different temperatures together with corresponding P-S-N curves for failure probabilities of $P_S = 10\,\%$ and $P_S = 90\,\%$.

From the stiffness degradation curves shown in Figure 5.68, the different damage behavior of specimens tested at 80 °C compared to those tested at lower temperatures (cf. Figure 5.60) became evident. For most specimens throughout all investigated load levels, a comparatively early 50 % to 60 % stiffness drop was determined, that arose from compressive failure of the upper Co SMC ply. Depending on the applied load, the specimens still withstood several cycles, while stiffness decreased at a considerably higher rate. The normalized dynamic stiffness

values after the stiffness drop have no significance, due to the large displacement. Still, the entire curves are shown for the reader to assess the difference between the number of cycles to failure of the upper Co SMC ply and the remaining plies.

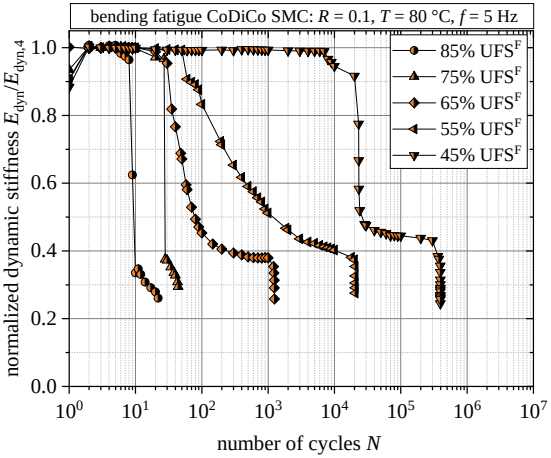

Figure 5.68: Normalized dynamic stiffness of CoDiCo SMC under cyclic bending load at 80 °C.

5.2.4 Influence of frequency

The S-N data obtained from bending fatigue tests of DiCo SMC at a frequency of 1 Hz and 10 Hz are depicted in Figure 5.69 along with the results of the tests carried out at 5 Hz (cf. Figure 5.49). Fatigue tests at 1 Hz were evaluated after $3.6 \cdot 10^5$ cycles due to the prolonged testing. All specimens that withstood this number of cycles were considered runouts in this evaluation and marked with an arrow. A higher frequency led to slightly higher fatigue lives in case of high applied loads in the low cycle fatigue range. In high cycle fatigue, no such trend was observed and fatigue life seemed to be independent of frequency within the investigated range. First runouts were obtained at a maximum stress of 166 MPa for all analyzed frequencies. Similar observations were made for CoDiCo SMC. As shown in Figure 5.70, specimens tested at 1 Hz tended to fail sooner compared

to specimens tested at 5 Hz and 10 Hz in the low cycle fatigue range, respectively, while no clear trend is observed in the high cycle fatigue range.

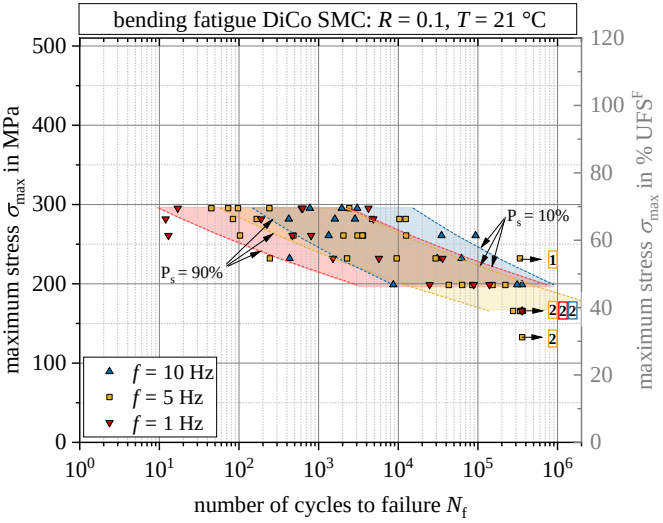

Figure 5.69: S-N data of DiCo SMC under bending fatigue load at different frequencies together with corresponding P-S-N curves for failure probabilities of $P_S = 10\,\%$ and $P_S = 90\,\%$.

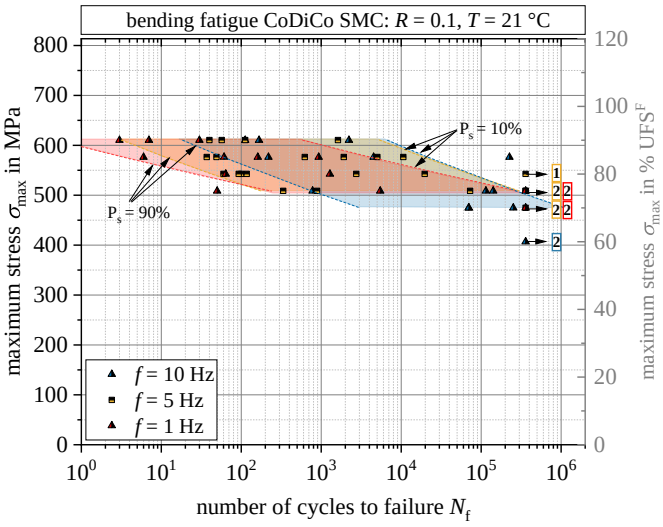

Figure 5.70: S-N data of CoDiCo SMC under bending fatigue load at different frequencies together with corresponding P-S-N curves for failure probabilities of $P_S = 10\,\%$ and $P_S = 90\,\%$.

6 Discussion

6.1 Investigated load cases

The fatigue behavior of hybrid Co SMC, DiCo SMC and CoDiCo SMC composites was characterized on coupon level under tension-tension and 3-point bending load. The sandwich-like structure of CoDiCo SMC is especially suited for the latter type of loading, as the strong and stiff carbon fibers are positioned at maximum distance from the neutral bending axis. Structural components in the automotive industry are mainly subjected to bending loads (e.g. subfloor structures with a normal load or leaf springs), which is why bending fatigue represents the more application-related load case. Nevertheless, in this thesis, a strong focus was placed on tension-tension loads, which allows for a more sophisticated initial analysis of damage mechanisms due to the reduced complexity of the stress state. For an application that requires highest tensile fatigue properties, the considered hybrid configuration is not expected to be the best option due to the low degree of dispersion of the two fiber types (Hofer et al., 1978; Swolfs et al., 2014).

6.2 Characterization methods

6.2.1 Determination of S-N diagrams

In the determination of S-N data, failure was defined by the separation of the specimens. Depending on the intended application, absolute or relative loss of strength or stiffness (as defined by O'Brien and Reifsnider (1981) or Hwang and

Han (1986)) present other possible failure criteria. While the measurement of the residual strength generally involves a very high experimental effort, the residual stiffness could be determined non-destructively during the tests. Corresponding S-N diagrams for different allowable residual stiffnesses can be generated analogously from the obtained test data.

6.2.2 Characterization of stiffness degradation

In this thesis, the dynamic stiffness, defined by Equation 2.2, has been chosen as a measure of the degradation of mechanical properties. Due to the almost linear stress-strain behavior of the analyzed materials, the dynamic stiffness is approximately equivalent to the tensile modulus of elasticity, but has the advantage of allowing continuous measurement during fatigue testing. In addition to the increasing tilt, which is described by the evolution of the dynamic stiffness, a shift of the hysteresis loops can also be observed for all investigated composites, as shown in Figure 5.11, Figure 5.24, Figure 5.30 and Figure 5.44. If such behavior is critical for certain applications, the fatigue modulus defined in Hwang and Han (1986) might be a more useful parameter to consider.

6.2.3 Evaluation of methods for damage characterization

Optical microscopy was the method of choice to analyze damage evolution in DiCo SMC and CoDiCo SMC. As discussed in Section 2.4, this method offered the advantage that small damage events, such as matrix cracks, could be easily detected and damage mechanisms could reliably be distinguished without the need for further interpretation or data processing. Damage in the DiCo SMC ply incorporated in the hybrid composite could be detected by an observation of the specimen edge. The method allowed for a quantitative analysis of crack density as shown, for example, in Figure 5.16. Besides the fact that careful and time-consuming specimen preparation was required, the biggest disadvantage

of this method was the limitation to surface analyses. The damage mechanisms observed at the specimen edges in DiCo SMC were qualitatively in agreement with observations by Schöttl et al. (2020), who carried out in-situ µCT measurements on the same composite.

µCT scans were used to characterize the microstructure of the analyzed materials, as shown in Figure 3.7 and Figure 3.6. However, µCT scanning additionally offers very high potential for analyzing the damage evolution in FRP qualitatively and quantitatively, even in hybrid composites. This makes the method highly interesting for future studies. As discussed in Section 2.4, µCT scanning allows to observe damage in the bulk material. By means of damage evaluation methods described by Schöttl et al. (2020) and Schöttl et al. (2021), the damage pattern can further be analyzed in a quantitative manner. However, there are still some challenges that come with this method. The larger the scanned specimen volume is, the lower the resolution. An analysis of matrix cracks in DiCo SMC, presented by Schöttl et al. (2020) and Schöttl et al. (2021) only considered small specimen volumes. When scanning tensile specimens with dimensions like the ones investigated in this thesis, the resolution is inevitably lower making it more difficult to detect small damage events. Furthermore, cracks can only be identified with a high probability, if opened by an applied tensile load. Still, tensile loads in one direction open only transverse cracks, but longitudinal cracks or (pseudo-)delamination, as seen in Figure 5.14, might remain undetected.

IR thermography served well to characterize the time and position on the specimen, at which damage started to localize. Localization of damage in DiCo SMC starting from the specimen edge was observed at an early stage during cyclic loading (cf. Figure 5.20). However, the results obtained from IR thermography only allowed to narrow down the area of localized damage and did not present information on the actual damage mechanisms. As discussed in Munoz et al. (2016), small damage events, such as the formation of individual small matrix cracks, which is the dominating damage mechanism in DiCo SMC, leads to low heat dissipation and is thus difficult to detect. Roughly determining the time and position of damage localization was also possible using IR thermography for CoDiCo SMC, as shown in Figure 5.38. But since the temperature field was measured

only on the surface of the Co SMC ply, it could not be distinguished, whether it was delamination of damage accumulation in the DiCo SMC ply that caused the heat dissipation.

AE analysis was successfully applied to determine the onset of damage in DiCo SMC and CoDiCo SMC under monotonic loading. Corresponding tests were conducted to determine the stress, at which the first damage event occurred without the specific aim to identify the damage mechanism. An analysis of damage evolution during testing with the aim to distinguish between mechanisms would require a considerable higher experimental effort in advance to identify the AE features of the individual mechanisms, which was beyond the scope of this study.

6.3 Fatigue behavior

6.3.1 Fatigue behavior of discontinuous SMC

S-N data and fatigue limit

Due to the differences in the material configuration (e.g. resin and fiber content) of DiCo SMC composites investigated by different authors, experimental results could not be compared directly. However, expressed in terms of normalized values, their S-N behavior was largely similar to the linearized S-N curve, that featured a slope of approximately 10 % of the materials' ultimate tensile strength per decade of cycles (Mandell and Meier, 1983; Wang and Chim, 1983; Denton, 1979). This is in agreement with the S-N data obtained for the UPPH-based DiCo SMC studied in this thesis, that featured a fatigue strength of around 40 % UTS^F after 10^6 cycles (cf. Figure 5.8). The results obtained in this study are also consistent with the literature in that a significant degradation of stiffness was observed in runout specimens under tension-tension fatigue load (cf. Figure 5.12). Hence, the fatigue strengths at $>10^6$ cycles reported in Section 5.1.2 did not correspond to a real fatigue limit.

A fatigue limit of DiCo SMC could be defined at 24 % UTS^F. This corresponds to the stress at which damage started to initiate in a monotonic test, as shown by AE analysis (Figure 5.6). Specimens loaded cyclically at 24 % UTS^F showed no signs of damage or reduction in stiffness after $2.6 \cdot 10^6$ cycles. Similar observations were made by von Bernstorff (1989), who studied the fatigue behavior of SMC above and below the knee point and found no fatigue damage in the latter case. Thus, AE analysis during tensile testing can possibly be used to estimate the fatigue limit of DiCo SMC.

For fatigue damage to occur, there must be one or more mechanisms of irreversibility causing accumulation of damage from cycle to cycle. Common energy-dissipating mechanisms are plasticity, friction and crack surface formation (Talreja and Singh, 2012). Friction between crack surfaces and new surface formation by brittle fracture are considered to be the predominant mechanisms in thermoset-based FRPs (Talreja and Singh, 2012) and are at the same time the two mechanisms, that can be detected by AE analysis. Thus, the assumption that no fatigue damage occurs below the stress, at which cracks first initiates under monotonic loading, implies, that plastic deformation is negligible in SMC. Indeed, FRPs do not exhibit plastic material behavior at the macroscopic level, but plastic deformation of the matrix can occur due to the size effect and the local multiaxiality of the stress state at the micro level. However, within the cycle range considered in this thesis, this mechanism has a negligible effect on the macroscopic fatigue behavior.

Stiffness degradation

The stiffness degradation behavior of the UPPH-based DiCo SMC studied in this thesis matched the observations by other authors in that the degradation rate increased with increasing applied load (cf. Figure 5.12). The stiffness degradation curves determined by Wang and Chim (1983), who studied polyester-based SMC with 50 wt.-% (35.4 vol.-%) glass fibers, revealed a higher total stiffness loss (20 % at 70 % UTS^S). Higher stiffness loss with more than 25 % before separation of the specimens was also obtained for the polyester-based SMC with 25 wt.-%

glass fibers investigated by Heimbuch and Sanders (1978). Denton (1979) found that stiffness of polyester-based SMC with 50 wt.-% (35.4 vol.-%) glass fibers decreased with increasing numbers of cycles even when tested at 15 % to 20 % UTS^F. Since the fiber content of the SMC composites investigated by Wang and Chim (1983) and Denton (1979) was higher compared to the composite analyzed in this study, which contained 44.7 wt.-% (26.3 vol.-%) fibers on average, the stiffness degradation behavior must have been influenced by other factors. One reason for the better performance of the DiCo SMC considered in this thesis in terms of residual stiffness might be the lack of fillers. The materials investigated by other authors were filled with $CaCO_3$, which led to damage initiation at lower stresses (Renz et al., 1988) and thus to a more pronounced stiffness degradation.

Damage evolution

As pointed out by Reifsnider et al. (1983), stiffness degradation is an ideal measure for the quantification of damage in FRP, since it is directly correlated with the occurring damage mechanisms. This was shown to be true for glass chopped strand mat/polyester resin laminates investigated by Owen and Howe (1972), who observed a correlation of stiffness and the amount of transverse matrix cracking. Similar results were obtained within this thesis as shown, for example, in Figure 5.16. Following the recommendation of Quaresimin et al. (2014), the weighted crack length was chosen to quantify crack density instead of the number of cracks, as was done by Owen and Howe (1972). The crack density showed a similar evolution as the normalized stiffness loss. Howe and Owen (1972) indicated a higher crack density at higher fatigue lives for the polyester-based chopped glass strand mat they studied. In contrast, Mandell and Meier (1983) stated, that there is no correlation between crack density and fatigue life and that the measured crack density was rather dependent on the local microstructure. For the UPPH-based DiCo SMC examined in this thesis, the crack density in specimens tested in the high cycle fatigue range was generally significantly higher, than in specimens tested in the low cycle fatigue range. However, finding a reliable quantitative correlation between the crack density and fatigue life with

the comparatively small numbers of specimens investigated, did not yield any meaningful results. This is due to sample-specific differences in the damage behavior resulting from the strong variations in the microstructure. Von Bernstorff (1989), among others, suggested, that there is a CDS for SMC in the sense that crack density in failed specimens is independent of the loading history and similar for monotonic and cyclic loading. This behavior could not be confirmed in this thesis. While crack density at failure was subject to high scatter, it was clearly shown that considerably less cracks were observed in specimens that failed due to monotonic load (cf. Figure 5.1) or after very low number of cycles (cf. Figure 5.10) compared to specimens that failed in the high cycle fatigue range (cf. Figure 5.9).

6.3.2 Fatigue behavior of continuous SMC

S-N data

The ultimate tensile strength of the carbon/epoxy FRP composite studied by Taheri-Behrooz et al. (2010) was twice as high compared to Co SMC, even though the fiber volume content was comparable. The fibers used by Taheri-Behrooz et al. (2010) featured a tensile strength that was 18.4 % higher compared to the carbon fibers used for the Co SMC composite studied in this thesis (cf. Table 2.4 and Table 3.1). The unidirectional FRP composites studied by Kawai and Yano (2016) and Chen and Hwang (2006) featured tensile strengths that were approximately 130 % higher compared to Co SMC. The fiber volume contents were 12 % and 14 % higher, respectively. While the tensile strength of the fibers used by Chen and Hwang (2006) was 18.4 % higher, compared to the fibers used in this study, the fibers used by Kawai and Yano (2016) were even stronger with almost 33 % higher tensile strength compared to the fibers within this thesis (cf. Table 2.4).

Absolute values of the S-N data are were directly comparable due to the use of different fibers, different fiber volume fractions and probably also differences in the fiber-matrix bonding. However, the normalized S-N data of UPPH-based Co SMC was well within the range given by the data reported by other authors,

even though higher scatter was recorded. This could be attributed to the fact that good impregnation of unidirectional fibers at a high weight content in the SMC process is still challenging. Some dry spots could be observed in the specimens, as for example in the one shown in Figure 5.23.

Stiffness degradation

The stiffness degradation curves for Co SMC, presented in Figure 5.25, were less smooth than those of DiCo SMC. Several jumps occurred spontaneously, that were attributed to fiber cluster fracture. Their occurrence was highly stochastical and dependent on the local strength of the fibers as well as local stress concentrations, for example due to adjacent crack tips or voids. Therefore, the stiffness degradation behavior was difficult to predict.

For one specimen tested at 65 % UTS^F, an (apparent) increase of stiffness was determined after approximately 500 cycles. One possible explanation for this behavior might be the partial failure of a tow outside of the measuring length that was observed during the experiment and led to a changing load distribution over the specimen width.

Besides a loss of the dynamic stiffness due to cyclic loading, a strong shift of the hysteresis loops was observed for Co SMC, as was shown in Figure 5.24. In applications that are critical in terms of maximum strains, this behavior must be taken into account and a different choice of stiffness parameter might have to be considered.

6.4 Effects of hybridization

6.4.1 CoDiCo SMC under tensile load

Monotonic tests

The tensile strength at quasi-static strain rate UTS^S of the CoDiCo SMC composite examined in this thesis was 126 % higher than that of DiCo SMC. Analogous studies of a similar material system by Trauth (2020) yielded a 193 % increase of UTS^S due to hybridization. The tensile strength of DiCo SMC measured in this thesis was slightly higher and the tensile strength of Co SMC was lower compared to the values depicted by Trauth (2020). CoDiCo SMC showed a less pronounced strain rate dependence compared to DiCo SMC, since the strain rate insensitive Co SMC dominated the material behavior. Therefore, the effect of hybridization was smaller at fatigue strain rate. UTS^F of CoDiCo SMC increased by only 92 % compared to DiCo SMC.

Failure of the hybrid composite was clearly dominated by the Co SMC plies that failed first, which resulted in additional stresses in the DiCo SMC ply, that ultimately exceeded its ultimate strength. This is in accordance with observations by Trauth (2020). Acoustic emission analysis showed, that the onset of damage in CoDiCo SMC under tensile loading occurred at approximately the same stress at which damage initiated in DiCo SMC. However, the first damage events were not attributed to matrix cracks in the DiCo SMC ply, but to fiber fracture in the Co SMC plies. The stress at which the first matrix cracks appeared was higher for CoDiCo SMC than for DiCo SMC specimens. An exact stress value was difficult to determine, since damage mechanisms besides fiber fracture could not be clearly distinguished.

To better evaluate effects of hybridization, the stresses in the individual plies of the hybrid composite at final failure were approximated and compared to the tensile strength of DiCo SMC and Co SMC. Knowing the average initial stiffness of DiCo SMC and Co SMC, as well as the approximate volume ratios of the

individual components in the hybrid, the stress-strain behavior of CoDiCo SMC was approached under the following assumptions:

- the plies are homogenous on a macroscopic scale,
- they show a linear elastic material behavior,
- strains are equal in the different plies (Voigt model),
- the plane stress condition applies,
- and the Poisson's effect is neglected.

Using 1D Hooke's law $\sigma(\varepsilon) = E\varepsilon$, the assumption of equal strains in all plies provides

$$\sigma_{\mathrm{Co}}(\varepsilon) = \frac{E_{\mathrm{Co}}}{E_{\mathrm{DiCo}}}\sigma_{\mathrm{DiCo}}(\varepsilon). \tag{6.11}$$

With $F(\varepsilon) = \sigma(\varepsilon)A$, the total force $F_{\mathrm{CoDiCo}}(\varepsilon) = F_{\mathrm{DiCo}}(\varepsilon) + F_{\mathrm{Co}}(\varepsilon)$ can be written as

$$\sigma_{\mathrm{CoDiCo}}(\varepsilon)A_{\mathrm{CoDiCo}} = \sigma_{\mathrm{DiCo}}(\varepsilon)A_{\mathrm{DiCo}} + \sigma_{\mathrm{Co}}(\varepsilon)A_{\mathrm{Co}}. \tag{6.12}$$

By using Equation 6.11, Equation 6.12 can be expressed by

$$\sigma_{\mathrm{DiCo}}(\varepsilon) = \frac{\sigma_{\mathrm{CoDiCo}}(\varepsilon)}{\gamma_{\mathrm{DiCo}} + \dfrac{E_{\mathrm{Co}}}{E_{\mathrm{DiCo}}}\gamma_{\mathrm{Co}}}. \tag{6.13}$$

γ_{Co} and γ_{DiCo} are the volume fractions of Co SMC and DiCo SMC, respectively. Under the assumption of constant width, they were approximated by taking the results from the thickness measurements of the individual plies (cf. Section 3.3), which yielded $\gamma_{\mathrm{DiCo}} = 0.769$ and $\gamma_{\mathrm{Co}} = 0.231$.

Equation 6.13 and 6.11 were slightly modified to

$$\sigma_{\mathrm{DiCo}}(\varepsilon) = \frac{\sigma_{\mathrm{CoDiCo}}(\varepsilon)}{\gamma_{\mathrm{DiCo}} + \frac{\bar{E}_{\mathrm{dyn,4,Co}}}{\bar{E}_{\mathrm{dyn,4,DiCo}}}\gamma_{\mathrm{Co}}} \tag{6.14a}$$

$$\text{and } \sigma_{\mathrm{Co}}(\varepsilon) = \frac{\bar{E}_{\mathrm{dyn,4,Co}}}{\bar{E}_{\mathrm{dyn,4,DiCo}}}\sigma_{\mathrm{DiCo}}(\varepsilon). \tag{6.14b}$$

$\bar{E}_{\mathrm{dyn,4,DiCo}} = 13.9$ GPa and $\bar{E}_{\mathrm{dyn,4,Co}} = 103.9$ GPa (cf. Section 5.1.2) correspond to the average initial dynamic moduli of the Co SMC and DiCo SMC specimens, respectively, that, unlike tensile modulus of elasticity, could be determined during the continuous fatigue tests.

With the $\mathrm{UTS}^{\mathrm{F}}$ of CoDiCo SMC of 456 MPa (cf. Table 5.1), Equation 6.14a and Equation 6.14b yielded $\sigma_{\mathrm{DiCo}}(\varepsilon_{\mathrm{t,CoDiCo}}) = 182$ MPa and $\sigma_{\mathrm{Co}}(\varepsilon_{\mathrm{t,CoDiCo}}) = 1366$ MPa. $\varepsilon_{\mathrm{t,CoDiCo}}$ corresponds to the failure strain of CoDiCo SMC. According to this approximation, the stress in the DiCo SMC ply was 55 MPa lower than the ultimate tensile strength $\mathrm{UTS}^{\mathrm{F}}$ of DiCo SMC, whereas the stress in the Co SMC plies was 226 MPa higher than the ultimate tensile strength $\mathrm{UTS}^{\mathrm{F}}$ of Co SMC (cf. Table 5.1).

The Co SMC plies withstood significantly higher loads compared to the solely continuous reinforced specimens. One explanation for an enhancement of strength might be residual stresses, that resulted from the manufacturing process. After compression molding of the plaques at temperatures of approximately 145 °C (cf. Section 3.2), cooling them down to room temperature resulted in a strain, than can be approximated by

$$\varepsilon(\Delta T) = \alpha_{\mathrm{Co}}\Delta T + \Delta\varepsilon_{\mathrm{Co}} = \alpha_{\mathrm{DiCo}}\Delta T + \Delta\varepsilon_{\mathrm{DiCo}}, \tag{6.15}$$

with the coefficients of thermal expansion of DiCo SMC[1] $\alpha_{\mathrm{DiCo}} = 1.6 \cdot 10^{-5}$ K^{-1} and Co SMC $\alpha_{\mathrm{Co}} = 6.8 \cdot 10^{-7}$ K^{-1} and a temperature difference $\Delta T = -124$ K. α_{Co} was approached by

$$\alpha_{\mathrm{Co}} = \frac{E_{\mathrm{CF}}\alpha_{\mathrm{CF}}\gamma_{\mathrm{CF}} + E_{\mathrm{UPPH}}\alpha_{\mathrm{UPPH}}(1-\gamma_{\mathrm{CF}})}{E_{\mathrm{CF}}\gamma_{\mathrm{CF}} + E_{\mathrm{UPPH}}(1-\gamma_{\mathrm{CF}})}, \tag{6.16}$$

with the tensile modulus of elasticity of the carbon fibers $E_{\mathrm{CF}} = 242$ GPa (Zoltek, 2017) and the UPPH resin system $E_{\mathrm{UPPH}} = 3.45$ GPa (Trauth, 2020), the fiber volume content $\gamma_{\mathrm{CF}} = 0.64$ (cf. Chapter 3) and the coefficient of thermal expansion of the carbon fibers $\alpha_{\mathrm{CF}} = 8 \cdot 10^{-8}$ K^{-1} (Dugin et al., 2020) and the matrix system $\alpha_{\mathrm{UPPH}} = 7.5 \cdot 10^{-5}$ K^{-1} (Kehrer, 2019).

$\Delta\varepsilon_{\mathrm{DiCo}}$ and $\Delta\varepsilon_{\mathrm{Co}}$ result from constraining effects that lead to residual stresses. Those residual stresses must result in an equilibrium of forces

$$\Delta F_{\mathrm{Co}} = -\Delta F_{\mathrm{DiCo}}, \tag{6.17}$$

which, by considering Hooke's law, leads to

$$E_{\mathrm{Co}}\gamma_{\mathrm{Co}}\Delta\varepsilon_{\mathrm{Co}} = -E_{\mathrm{DiCo}}\gamma_{\mathrm{DiCo}}\Delta\varepsilon_{\mathrm{DiCo}}. \tag{6.18}$$

Inserting Equation 6.16 yields

$$\Delta\varepsilon_{\mathrm{Co}} = \frac{E_{\mathrm{DiCo}}\gamma_{\mathrm{DiCo}}}{E_{\mathrm{Co}}\gamma_{\mathrm{Co}} + E_{\mathrm{DiCo}}\gamma_{\mathrm{DiCo}}}(\alpha_{\mathrm{DiCo}} - \alpha_{\mathrm{Co}})\Delta T. \tag{6.19}$$

By applying Hooke's law and using the respective initial dynamic moduli of Co SMC and DiCo SMC instead of the corresponding modulus of elasticity, Hooke's law provides

[1] α_{DiCo} was measured in a dilatometer test by Juliane Lang, Institute of Engineering Mechanics, KIT.

$$\Delta\sigma_{\mathrm{Co}} = \bar{E}_{\mathrm{dyn,4,Co}}\Delta\varepsilon_{\mathrm{Co}} = -60.8\,\mathrm{MPa}. \tag{6.20}$$

The corresponding residual stress is the DiCo SMC ply could be determined to

$$\Delta\sigma_{\mathrm{DiCo}} = \frac{\gamma_{\mathrm{DiCo}}}{\gamma_{\mathrm{Co}}}\Delta\sigma_{\mathrm{Co}} = 18.3\,\mathrm{MPa}. \tag{6.21}$$

In conclusion, the residual stresses in the Co SMC plies alone do not explain the enhanced tensile strength in the hybrid composite. In conclusion, a change in damage mechanisms must lead to a higher exploitation of the carbon fibers' mechanical performance, as discussed by Swolfs et al. (2014). The more ductile component, which is the DiCo SMC ply in this case, is assumed to have influenced the damage behavior of the more brittle component, which are the Co SMC plies, by bridging local fiber fracture, reducing stress concentrations leading to a slower damage evolution and increasing the critical size of fiber fracture clusters.

S-N behavior

Hybridization of DiCo SMC with unidirectional Co SMC had an even more pronounced effect on the fatigue strength than on the ultimate tensile strength. While $\mathrm{UTS}^{\mathrm{F}}$ increased by 92 %, fatigue strength of CoDiCo SMC was 209 % higher than that of DiCo SMC. The fatigue ratio of CoDiCo SMC, which describes the stress, at which all tested specimens were runouts, divided by the ultimate tensile strength $\mathrm{UTS}^{\mathrm{F}}$ (Dickson et al., 1989) was 0.6 and thus higher than that of both DiCo SMC (fatigue ratio of 0.37) and Co SMC (fatigue ratio of 0.55).

Since the predominant mechanisms leading to failure of a composite are effective only in a limited range of applied maximum strain (Talreja, 1981), there is merit for expressing fatigue-life data in terms of strain instead of stress, to better evaluate hybridization effects and analyze underlying mechanisms. The fatigue-life diagram is expected to consist of different parts, each corresponding to a different underlying damage mechanism (Talreja, 1981). Stress-life data auf

Co SMC, DiCo SMC and CoDiCo SMC presented in Section 5.1.2 was converted into strain-life data under the assumption of a linear elastic material behavior, by using the corresponding initial dynamic stiffness. The results are depicted in Figure 6.1. Strain-life curves, depicted as solid lines, were approximated by using the restricted form of the power law function (Júnior and Belísio, 2014)

$$\log(\varepsilon) = P_1 - P_2 \ \log(N) \tag{6.22}$$

with the parameters P_1 and P_2, that were determined from the experimental data via linear regression.

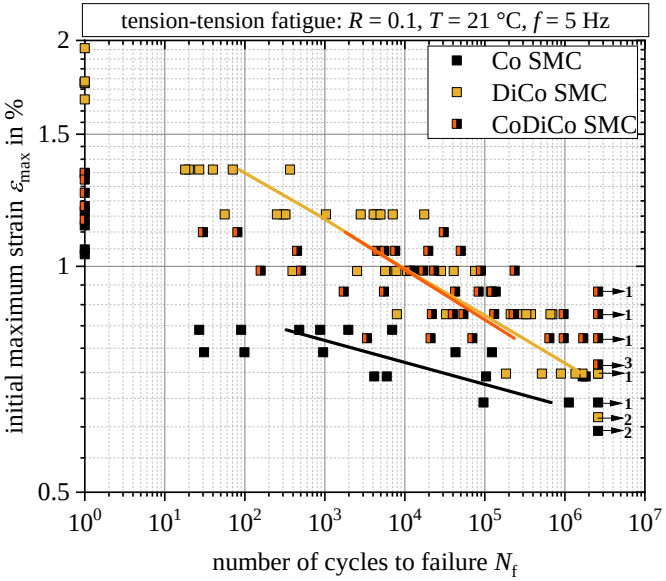

Figure 6.1: Strain-life diagram of Co SMC, DiCo SMC and CoDiCo SMC, determined by converting stresses into initial strains by using the initial dynamic modulus. Solid lines depict S-N curves determined by linear regression.

The difference in failure strain of Co SMC and DiCo SMC was pronounced especially under monotonic loading and diminished with increasing numbers of cycles. While the mechanical behavior of CoDiCo SMC was dominated by the Co SMC plies under monotonic loading, a change of mechanisms was observed under fatigue loading at initial maximum strains below 1.1 % that led to progressive damage of the specimens. The fatigue behavior was clearly dominated by the DiCo SMC ply with the strain-life curves of DiCo SMC and CoDiCo SMC showing good correlation. Under the assumption of equal strains in all plies of the hybrid composite, the Co SMC plies showed significantly higher fatigue strains compared to solely continuous reinforced specimens, which can be considered a positive effect of hybridization. In the high cycle fatigue range ($>10^5$ cycles), the interaction between the Co and DiCo plies was also an important mechanism, with continuous reinforcement supporting the DiCo plies where crack networks formed. At an initial maximum strain of 0.74 %, no failure of CoDiCo SMC specimens occurred within $2.6 \cdot 10^6$ cycles. This is a remarkable result, since this is higher compared to corresponding values obtained for both Co SMC (0.6 %) and DiCo SMC (0.63 %). In the high cycle fatigue range, CoDiCo SMC performed better than both of its components.

Similar findings were obtained by approximating the initial stresses to which each individual ply in a CoDiCo SMC specimen was subjected during the fatigue tests. This was done under the assumptions discussed in Section 6.4.1 by using Equation 6.14a and Equation 6.14b with σ_{Co}, σ_{DiCo} and σ_{CoDiCo} now being a function of the number of cycles to failure. Figure 6.2 shows the analytically determined initial ply stresses in each tested CoDiCo SMC specimen (cf. Figure 5.27) via the fatigue life of the corresponding CoDiCo SMC specimen. Under the assumption, that the number of cycles to failure of the hybrid composite corresponds to the number of cycles to failure of all plies, which is in accordance with the experimental observations, these results can be interpreted as approximated S-N data of the individual plies in the hybrid. It should be noted that, in this approximation, a constant amplitude problem was assumed, even though the stress amplitude slightly varied due to different amounts of stiffness degradation in the different plies. Also shown in Figure 6.2 are the experimentally determined S-N data of

DiCo SMC specimens (cf. Figure 5.8) and Co SMC specimens (cf. Figure 5.22) for comparison.

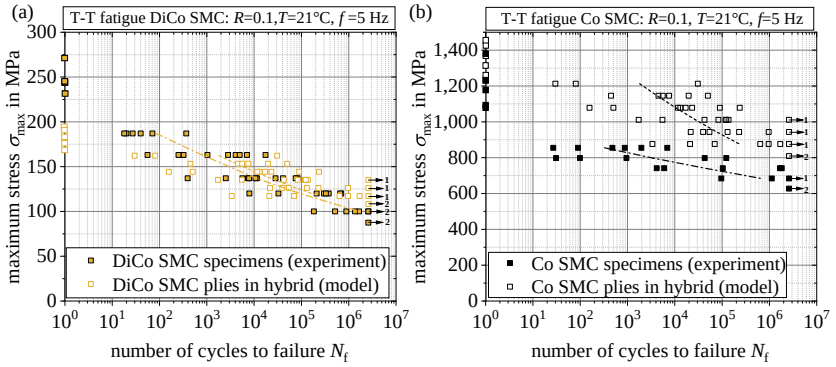

Figure 6.2: Analytically determined S-N data of (a) the DiCo SMC ply and (b) the Co SMC plies in the hybrid CoDiCo SMC specimens together with the experimentally determined S-N data of DiCo SMC and Co SMC specimens for comparison.

As can be seen from Figure 6.2a, the fatigue stress of the DiCo SMC plies were well within the range of the fatigue stress of DiCo SMC specimens for medium numbers of cycles. The mechanical performance of the DiCo SMC plies in the hybrid was generally largely unaffected by the much thinner Co SMC plies. While a Co SMC dominance was observed under monotonic tensile loading, a change of mechanisms took place at higher numbers of cycles. Several CoDiCo SMC specimens did not fail within $2.6 \cdot 10^6$ cycles, even though the analytically determined initial stress in both the Co SMC and DiCo SMC plies exceeded the components' fatigue strength. Looking at the runout specimen in Figure 5.29, the DiCo SMC ply was significantly damaged, whereas the Co SMC plies remained largely intact. It can be concluded, that the amount of stiffness degradation was higher in the DiCo SMC ply compared to the Co SMC plies. This resulted in a stress redistribution leading to decreasing stresses in the DiCo SMC ply and slightly increasing stresses in the Co SMC plies. In this case, the Co SMC plies supported the DiCo SMC ply, which represented the weaker link in the high cycle fatigue range. Figure 5.34 depicts, how the Co SMC plies bridged weak spots

in the DiCo SMC ply, that resulted from the coalescence of cracks and would have resulted in total failure without the additional support of the continuous reinforcement.

The observations discussed allow an approximate estimation of the fatigue behavior of CoDiCo SMC using an empirical modeling approach. Knowing that the fatigue behavior of CoDiCo SMC is largely dominated by the DiCo SMC ply, there is merit for assuming that a stress, which is applied to the hybrid, equals the fatigue strength of the hybrid at a specific number of cycles *N*, if it results in a stress in the DiCo SMC ply, which equals the fatigue strength of DiCo SMC at the same number of cycles *N*. In analogy to Equation 6.14a, the S-N curve of CoDiCo SMC can thus be approximated by

$$\sigma_{\mathrm{CoDiCo}}(N) = \sigma_{\mathrm{DiCo}}(N)\left(\gamma_{\mathrm{DiCo}} + \frac{\bar{E}_{\mathrm{dyn,4,Co}}}{\bar{E}_{\mathrm{dyn,4,DiCo}}}\gamma_{\mathrm{Co}}\right) \tag{6.23}$$

with $\sigma_{\mathrm{DiCo}}(N)$ being the S-N curve of DiCo SMC. The result obtained from Equation 6.23 is depicted in Figure 6.3 as solid yellow line, which is in good correlation with the S-N curve of CoDiCo SMC determined from experimental results via linear regression.

The DiCo SMC dominated region depicted in Figure 6.3 is limited laterally by 10 % and 90 % P-S-N-curves that were calculated by using Equation 6.23 and by inserting the 10 % and 90 % P-S-N-curves of DiCo SMC. Since scatter was more pronounced in CoDiCo SMC compared to DiCo SMC, the region described by the model is more narrow compared to the range covered by the experimental data. The DiCo SMC dominated region, is limited towards the top by the scatter range of the ultimate tensile strength of CoDiCo SMC (Co SMC dominated region). At high numbers of cycles ($>5 \cdot 10^5$ cycles), the model underestimates the performance of CoDiCo SMC and provides a rather conservative estimate. A more accurate approximation might be possible by considering the changing stiffness ratio leading to changing stresses in the individual plies with increasing numbers of cycles. A residual stiffness model for both DiCo SMC and Co SMC would thus

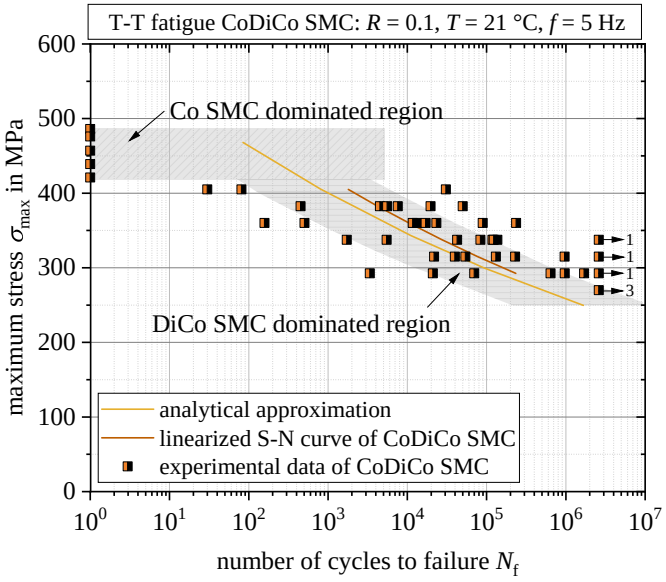

Figure 6.3: Analytical approximation of the fatigue life of CoDiCo SMC. The solid yellow line approximates the S-N curve of CoDiCo SMC based on the S-N curve of DiCo SMC. The orange line depicts the S-N curve of CoDiCo SMC, that was determined from the experimental results via linear regression. The grey shaded areas indicate the predominant damage mechanisms.

be helpful for a better approximation. However, the empirical approach presented here serves well for a rough estimate.

Stress-strain behavior

The stress-strain behavior of CoDiCo SMC was largely dominated by the Co SMC plies. As can be seen from Figure 5.30, the hysteresis loops depicted a tension stiffening behavior similar to that of Co SMC (cf. Figure 5.24). However, the shift of the hysteresis loops was considerably smaller in the hybrid CoDiCo SMC compared to both Co SMC (cf. Figure 5.24) and DiCo SMC (cf. Figure 5.11), which can be considered a positive effect of hybridization. Besides that, the

behavior was mainly dominated by Co SMC with the stress-strain curves showing a tension stiffening behavior.

Stiffness degradation and damage evolution

For most part of fatigue life, stiffness degradation was less pronounced in CoDiCo SMC (cf. Figure 5.32) compared to DiCo SMC (Figure 5.13). The Co SMC plies supported the DiCo SMC ply, as long as they were not overloaded. Therefore, if a fatigue criterion was defined by a critical amount of stiffness degradation instead of ultimate failure, as discussed in Section 6.3.1, CoDiCo SMC would perform even better compared to DiCo SMC.

The analysis of damage evolution in the DiCo SMC ply of the hybrid composite confirmed the statement, that its fatigue behavior was largely unaffected by the continuous reinforcement. Figure 6.4a shows that the absolute loss of stiffness versus normalized fatigue life is similar for DiCo SMC and CoDiCo SMC in the beginning. Jumps in the CoDiCo SMC curves, that were attributed to partial failure of the Co SMC plies, led to deviation from the DiCo SMC curve. The evolution of crack density in the DiCo SMC specimens and in the DiCo SMC plies of the hybrid composite were largely similar, as can be seen from Figure 6.4b.

Comparison with other CoDiCo FRP composites

To the author's knowledge, no research on the fatigue behavior of CoDiCo FRPs reinforced with discontinuous glass fibers and unidirectional carbon fibers has been published yet. Riegner and Sanders (1979), Kundrat et al. (1982) and Springer (1983) considered fatigue of CoDiCo FRPs with glass fibers being used as discontinuous and continuous reinforcement. Riegner and Sanders (1979) found runouts at 40 % UTS^S that lost 7 % of their initial stiffness after 10^6 cycles. Kundrat et al. (1982) reported a fatigue strength of 38 % UTS^F at $3 \cdot 10^6$ cycles and Springer (1983) found fatigue strength to be less than 50 % UTS^F at 10^6 cycles. In comparison, for the hybrid composite considered in this thesis, all specimens

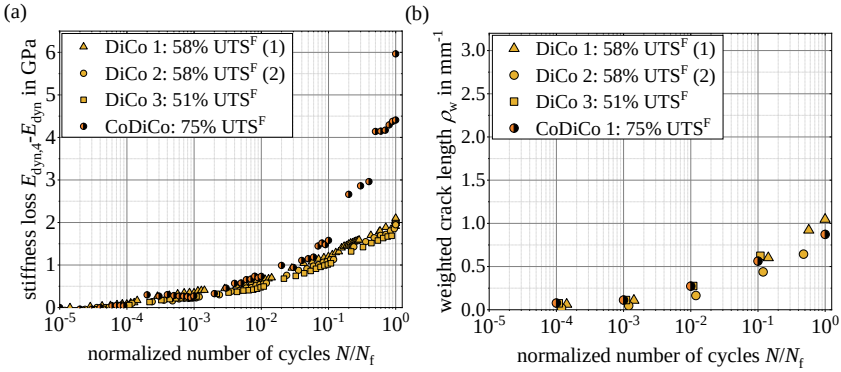

Figure 6.4: Damage evolution in DiCo SMC and CoDiCo SMC in terms of (a) the absolute stiffness loss and (b) the crack density in the DiCo SMC specimens and the DiCo SMC plies of CoDiCo SMC specimens.

tested at 65 % UTS^F were runouts. Single runouts were obtained also at considerably higher stresses. The lower ductility of the unidirectional carbon fiber reinforcement compared to glass fibers, led to more pronounced constraining effects and to a higher ultimate strength and fatigue strength.

6.4.2 CoDiCo$^{0/90}$ SMC under tensile load

Monotonic tests

The ultimate tensile strength at quasi-static strain rate UTS^S and fatigue strain rate UTS^F of CoDiCo$^{0/90}$ SMC increased by 94 % and 71 %, respectively, compared to DiCo SMC. these values are lower than those obtained for CoDiCo SMC, which was expected due to the additional 90° plies not carrying a significant amount of the load. While the specimens' cross-section increased by 22 % on average, the load bearing capacity did not increase significantly.

S-N behavior

The particularly pronounced effect of hybridization on the fatigue strength, that was determined for CoDiCo SMC with a 0° continuous reinforcement, could not be obtained with a 0°/90° reinforcement. In the case of $CoDiCo^{0/90}$ SMC, fatigue strength increased by only 85 % compared to DiCo SMC. This is significantly less compared to the increase of 209 % determined for CoDiCo SMC. In terms of the fatigue ratio, no positive effect of hybridization was observed. The fatigue ratio of 0.4 is comparable to the value determined for DiCo SMC and significantly lower compared to Co SMC, which indicated a core-dominated fatigue behavior.

To better evaluate hybridization effects, maximum stresses were converted to initial maximum strain by using the initial dynamic stiffness of $CoDiCo^{0/90}$ SMC. The corresponding strain-life diagram is depicted in Figure 6.5.

In contrast to CoDiCo SMC with a unidirectional continuous reinforcement, $CoDiCo^{0/90}$ SMC showed a less pronounced Co-dominated behavior under monotonic loading. Under fatigue loading, the initial maximum strain was significantly higher compared to Co SMC but still below the results obtained for DiCo SMC. Runouts were obtain for initial maximum strains below those of DiCo SMC and Co SMC. Hence, a negative effect of hybridization in terms of initial maximum strain was observed for $CoDiCo^{0/90}$ SMC.

Stress-strain behavior

As depicted in Figure 5.44, the hysteresis loops of $CoDiCo^{0/90}$ SMC also revealed a tension stiffening behavior, that was already observed for CoDiCo SMC. The shift of the hysteresis loops was also comparable to that of CoDiCo SMC and smaller compared to both DiCo SMC and Co SMC, which can be considered a positive effect of hybridization.

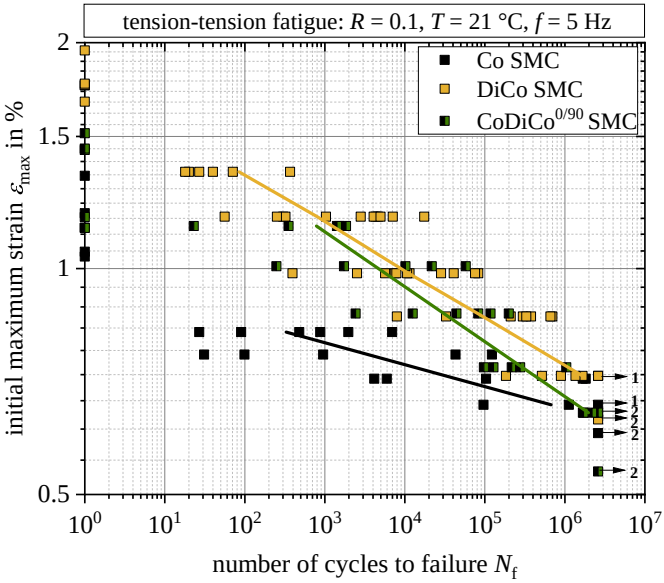

Figure 6.5: Strain-life diagram of Co, DiCo and CoDiCo$^{0/90}$ SMC, determined by converting stresses into initial strains by using the initial dynamic modulus. Solid lines depict S-N curves determined by linear regression.

Stiffness degradation and damage evolution

CoDiCo$^{0/90}$ SMC performed considerably worse compared to CoDiCo SMC in terms of relative stiffness degradation. After 90 % of fatigue life, a stiffness loss of more than 12 % was observed for all applied stresses except the ones tested at the highest stress of 85 % UTS^{F}. The stiffness loss is hence comparable to the values obtained for DiCo SMC. Corresponding values were between 5 % and 9 % for CoDiCo SMC. When comparing the damage variable of DiCo SMC (Figure 5.13) and CoDiCo$^{0/90}$ SMC (Figure 5.32), a similar strong increase within the first 5 % of fatigue life could be observed, which again indicates a core-dominated fatigue behavior.

The comparably low fatigue strength and high stiffness degradation observed for CoDiCo$^{0/90}$ SMC can be explained taking the damage evolution into account (Figure 5.47). Due to the low strength and stiffness of the 90° ply, even comparably low applied stresses resulted in the formation of multiple ply cracks within the first few loading cycles, similar to the behavior in cross-ply laminates. They occurred at a regular spacing and were considerably large with the ply thickness being approximately 0.32 mm. With further loading, they grew into the matrix and triggered delamination between the 0° and the 90° ply. The typical evolution of crack density in the DiCo SMC ply observed in DiCo SMC specimens as well as in CoDiCo SMC was not found in CoDiCo$^{0/90}$ SMC. It was the growth and coalescence of opposing large cracks initiated in the 90° ply, that caused separation of the specimens. In the CoDiCo$^{0/90}$ SMC specimens analyzed in this thesis, the 0° plies were located on the surface and the 90° plies were in proximity to the DiCo SMC ply. Investigations by Montesano et al. (2015) and Nairn and Hu (1992) showed a negative effect on the stiffness of cross-ply laminates, when 90° plies served as surface layers. However, no information on strength or fatigue strength was given. Based on the findings from the damage analysis of the hybrid composites, it is possible that a 90° ply on the outside might crack and lose most of its load bearing capacity without substantial influence of the fatigue behavior of the 0° ply and the DiCo SMC ply. For applications subject to multiaxial loading, both cases need to be considered.

6.4.3 CoDiCo SMC under bending load

Monotonic tests

The ultimate flexural strength at quasi-static strain rate UFS^{s} of CoDiCo SMC increased by 54 % compared to DiCo SMC. In comparison, Trauth (2020) determined a 101 % increase in flexural strength. While the flexural strength of CoDiCo SMC measured in this thesis was 8 % above the value determined by Trauth (2020) and still within the range of the standard deviation, the flexural strength of DiCo SMC was found to be 25 % higher than that obtained by

Trauth (2020). This effect might be traced back to the influence of friction, since application of PTFE tape on the lower supports and the loading nose had a significant influence on the bending strength. The ultimate flexural strength UTS^F increased by 60 %, which is comparable to the effect of hybridization observed at quasi-static strain rate.

S-N behavior

Due to the sandwich-like structure of CoDiCo SMC, the effect of hybridization was even more pronounced under bending fatigue load compared to tension-tension fatigue load. The flexural fatigue strength of CoDiCo SMC was 258 % higher compared to DiCo SMC and almost as high as the fatigue strength of Co SMC. The fatigue ratio of CoDiCo SMC was 0.7 and thus higher compared to both DiCo SMC and Co SMC that featured a fatigue ratio of 0.3 and 0.5, respectively.

Stiffness degradation and damage evolution

The stiffness degradation behavior of CoDiCo SMC under bending fatigue load was largely dominated by the Co SMC ply. As can be seen from Figure 5.32 and Figure 5.26, the evolution of the damage variable was very similar for both materials. In comparison, stiffness degradation in DiCo SMC was far more pronounced (cf. Figure 5.13). On average, the damage variable of CoDiCo SMC was reduced by more than 50 % compared to that of DiCo SMC.

As shown in Figure 5.62, CoDiCo SMC specimens failed due to shear buckling of the compression loaded Co SMC ply. Not only is the compressive strength of Co SMC less than 50 % of it's tensile strength (Trauth, 2020), compressive residual stresses that are a result of the different coefficients of thermal expansions of Co SMC and DiCo SMC led to the reduced resistance to compressive loads of the Co SMC ply. The DiCo SMC ply and the Co SMC ply on the tension loaded side hardly showed any damage until the compression loaded Co SMC ply failed. A material configuration with a continuous reinforcement only on the

tension loaded side would enable better exploitation of the materials' potential in terms of strength but would feature a significantly reduced modulus of elasticity (Akiyama, 2014). However, the different coefficients of thermal expansions would result in strong warpage, that needs to be accounted for during the manufacturing process.

6.5 Influence of temperature

The influence of temperature on the mechanical properties of DiCo SMC and CoDiCo SMC was first observed in monotonic bending tests, as shown in Figure 5.64 and Figure 5.65. In the case of DiCo SMC, increasing the temperature from 21 °C to 80 °C resulted in a decrease of flexural strength of 24 % at quasi-static strain rate and 14 % at fatigue strain rate. No significant effect was observed by reducing the temperature to -20 °C. This is in agreement with observations by Denton (1979), who found the effect of temperature on the fatigue behavior of polyester-based SMC to be stronger at high temperatures (Figure 2.6). Heimbuch and Sanders (1978) observed a similar behavior for epoxy-based SMC.

In the case of CoDiCo SMC, decreasing the temperature to -20 °C resulted in an increase in flexural strength by 25 % at quasi-static strain rate and 14 % at fatigue strain rate. Increasing the temperature to 80 °C did not result in a significant decrease in flexural strength. While there is no data available from literature on flexural strength at -20 °C, Kliger (1978) reported results on quasi-static bending tests of polyester-based glass fiber DiCo SMC and CoDiCo SMC at enhanced temperatures (Table 2.3). Increasing the temperature from 21 °C to 80 °C led to a reduction of flexural strength by 36 % in case of DiCo SMC and between 43 % and 48 % in the case of CoDiCo SMC, depending on the number of unidirectional carbon fiber plies. In contrast to the results obtained in this thesis, Kliger (1978) observed a more pronounced effect of temperature on flexural strength. Under tensile load, DiCo SMC showed a reduction in strength of 39 % due to the temperature increase, while the decrease in a hybrid composite was only between

14 % and 21 %. The results by Kliger (1978) indicate, that a less pronounced effect under tension load compared to bending load can be expected.

For DiCo SMC, an influence of temperature on the fatigue behavior was small when comparing the S-N curves at room temperature and at 80 °C. A shift of 20 MPa (7 % lower maximum stress) could be seen in the low cycle fatigue range, while the influence was negligible in the high cycle fatigue range. Experiments carried out at -20 C showed a higher influence. A shift of the S-N curve to higher normalized stresses of up to 50 MPa (27 % higher maximum stress) was observed. The influence was more pronounced in the high cycle fatigue range than in the low cycle fatigue range. The DiCo SMC material examined in this thesis showed a lower sensitivity to temperature than the polyester-based DiCo SMC investigated by Springer (1983), who determined a reduction of fatigue strength of approximately 50 % and 30 % for SMC with fiber weight contents of 65 % and 25 %, respectively, by increasing the temperature from 23 °C to 93 °C. The influence of temperature was comparable to that observed by Tamboura et al. (2020), who investigated highly oriented polyester-based DiCo SMC with a fiber content of only 28 wt.-%, that was filled with 37 wt.-% $CaCO_3$ particles, in 0° and 90° direction as well as a randomly oriented configuration. When comparing the results between the experiments at -30 °C and 80 °C, a shift of the normalized S-N curve of approximately 15 % was observed for the highly oriented specimens in 0° direction as well as for the randomly oriented specimens. The shift was more pronounced (approximately 24 %) for highly oriented specimens in 90° direction. The room temperature curves presented by Tamboura et al. (2020) were close to the curves obtained at -30 °C in the high cycle fatigue range and slightly below the -30 °C curve at lower numbers of cycles. This is in contrast to the observations in this thesis. The material investigated was influenced stronger by a decrease of temperature in contrast to an increase. To better compare and evaluate the temperature influence, the glass transition temperature of the materials studied by the other authors need to be taken into account. However, this information is often not presented in the literature.

Despite the fact, that unidirectional FRPs are largely insensitive to temperature in the fiber direction (Kawai et al., 2001), the effect of temperature was far more

pronounced in hybrids combining DiCo SMC and Co SMC. Fatigue strength was reduced by 170 MPa, compared to the fatigue strength at room temperature, when increasing the temperature to 80 °C, while an increase of approximately 100 MPa was observed for temperatures of -20 °C. At 80 °C, the Co SMC ply on the compression-loaded side failed after a low number of cycles in nearly all specimens tested, while the remaining plies were still able to withstand the applied load. However, stiffness degraded at a higher rate due to the increased load the plies had to carry. According to Kawai et al. (2001), Shimokawa et al. (2008) and Montesano et al. (2012), the influence of temperature is not significant under tension-tension fatigue loading for composites showing a fiber-dominated behavior. Investigations by Shimokawa et al. (2008) showed that this also holds true for cyclic compressive loads. The shear stresses in the transition zone between the Co SMC and the DiCo SMC ply might possibly be the main reason for the high temperature-dependence of the hybrid CoDiCo SMC. This assumption is based on the findings by Sjogran (2002), who investigated the fatigue behavior of epoxy-based continuous FRPs under mode I, mode II and mixed-mode fatigue load and showed that temperature significantly accelerates delamination crack growth. Partial delamination of the Co SMC ply might lead to micro-buckling or kinking and ultimately fracture of the carbon fibers. Since delamination and fiber-breakage usually occurred simultaneously, it is difficult to establish a causal link between the different damage mechanisms. Sjogran (2002) only considered double cantilever beam, end-notch flexural and mixed mode bending tests in his study. Consequently, it is unclear whether the same effect can be expected under uniaxial loads. To the author's knowledge, studies on the influence of temperature on the fatigue behavior of continuous-discontinuous composites were published solely by Riegner and Sanders (1979) and Springer (1983). In these publications, reinforcement, be it continuous or discontinuous, was realized by glass fibers. According to Springer (1983), the reinforcement of DiCo SMC with continuous fibers led to a reduced temperature sensitivity under tension-tension load in transverse direction. Riegner and Sanders (1979) also found the effect of temperature to be small in transverse direction, while more pronounced temperature dependence was observed in transverse direction. Based on these observations,

a less pronounced temperature sensitivity of CoDiCo SMC is expected under tension-tension load in flow direction.

6.6 Influence of frequency

For the examined frequencies, no significant frequency-dependence was observed for both DiCo SMC and CoDiCo SMC, as can be seen from Figure 5.69 and Figure 5.70. The results are in accordance with Heimbuch and Sanders (1978) who found no frequency effect on the fatigue lives of polyester-based and epoxy-based SMC for frequencies up to 20 Hz. Shirinbayan et al. (2017) came to similar conclusions. They showed no frequency-dependence of vinyl ester-based DiCo SMC for frequencies up to 50 Hz in case of small applied loads and a slight tendency towards decreasing fatigue lives with increasing frequency when the applied load was high. Frequencies of 100 Hz and higher led to induced thermal fatigue and in turn affected fatigue lives for both low and high applied stresses.

According to Barron et al. (2001), no effect of frequency on the fatigue behavior of continuous FRPs with a unidirectional orientation could be observed. Therefore, the combination of DiCo SMC with unidirectional Co SMC is not expected to show a frequency-dependent behavior when induced thermal fatigue can be ruled out. Investigations carried out in this thesis confirmed this assumption. However, frequency might have an effect in the case of a 0°/90° Co SMC reinforcement, since cross-ply laminates do show frequency dependency, especially at high stress amplitudes, as shown by Mandell and Meier (1983) and Barron et al. (2001).

According to Heimbuch and Sanders (1978), frequencies of 20 Hz can be encountered in the automotive service environment. In this range, frequency effects were found to be negligible, at least in case of CoDiCo SMC with a unidirectional continuous reinforcement.

6.7 Causes of scatter

Several manufacturing-related variations in the material's microstructure result in scatter of mechanical properties. In DiCo SMC, the most evident factors are variations in fiber content and orientation.

As presented in Chapter 3, the local and global fiber weight fractions of Co SMC and DiCo SMC are subject to large scatter. Results from TGA showed high cross-plaque deviations and even higher deviations within a plaque. Looking for example at DiCo SMC plaque 6 (Figure 3.5), the fiber weight content in specimen No. 4 and No. 5 varied by more than 7 %, even though they were extracted from the same plaque at a distance of only 25 mm from one another. Similar observations were reported by Trauth (2020).

Trauth (2020) further analyzed fiber orientation distributions of DiCo SMC and CoDiCo SMC specimens. A comparison of four different DiCo SMC specimens showed no significant difference in the global fiber orientation. However, going through the specimens' thickness, variations of the local fiber orientation could be observed.

The aforementioned factors obviously have an impact on the materials stiffness and explain the scatter of the initial dynamic stiffness measured in the fatigue tests. However, the respective global quantities are not the main reason for scatter in the S-N data, especially not in the case of tension-tension load. This can be seen from a lack of correlation between the initial stiffness and the fatigue life. The number of cycles to failure of DiCo SMC, CoDiCo SMC and CoDiCo$^{0/90}$ SMC tested at different stresses were plotted against the initial dynamic stiffness in Figure 6.6. No clear dependence between the two quantities could be observed.

Failure due to cyclic loading promoted the heterogeneity of the microstructure resulting in weak spots either in resin-rich areas or areas with a locally unfavorable orientation and distribution of the fiber bundles. These weak spots varied in number and characteristics from specimen to specimen. As could be seen from

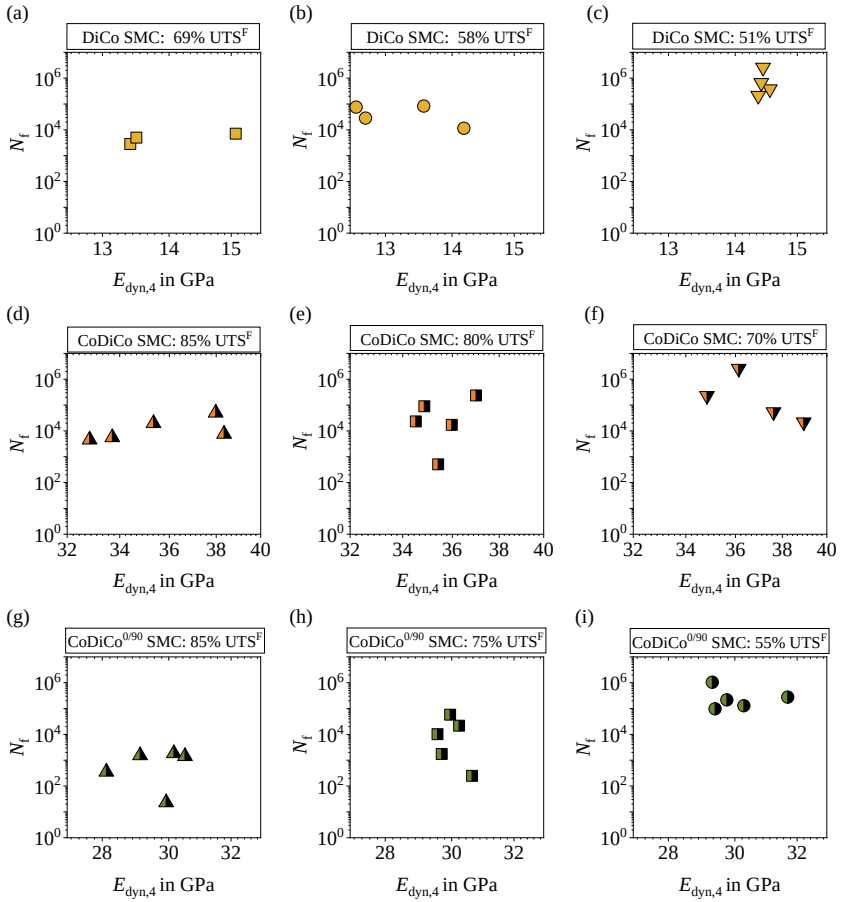

Figure 6.6: Fatigue life over initial dynamic modulus of (a)-(c) DiCo SMC, (d)-(f) CoDiCo SMC and (g)-(i) CoDiCo$^{0/90}$ SMC at different stress levels under tension-tension fatigue load.

the IR thermography results in Figure 5.20, damage in DiCo SMC was strongly localized at a corresponding weak point at an early stage during fatigue life.

Under cyclic 3-point bending, a clearer connection between the initial dynamic stiffness and fatigue life could be observed, at least for DiCo SMC and CoDiCo SMC, since the specimens were stressed more locally and damage was limited to a smaller volume. However, the results were not consistent throughout all analyzed stress levels. No clear connection between the initial dynamic stiffness and fatigue life was observed for Co SMC (Figure 6.7). Scatter in the fatigue properties of Co SMC was mainly caused by different amounts of fiber misalignment and fiber undulations, as well as dry spots resulting from an insufficient impregnation of the semi-finished material. The fiber volume fraction was too subject to scatter as well, however, a higher fiber volume fraction did not necessarily lead to higher strengths, as was already discussed by Trauth (2020). Consequently, slight differences in fiber volume fraction are not assumed to significantly influence fatigue life, if other variances such as fiber misalignment, fiber undulations and/or dry spots are present.

In general, scatter was most pronounced for CoDiCo SMC. This was mostly caused by the higher number of different damage mechanisms due to a higher complexity in the random local microstructure of the composite plies. In addition, characteristics of the transition zone between DiCo SMC and Co SMC plies differed in each specimen, which resulted in even more uncertainties. As shown by Trauth (2020) and as confirmed in this thesis, the thicknesses of the different plies in the CoDiCo SMC also varied. While thickness variations of the DiCo SMC and Co SMC specimens were accounted for in calculating the stresses based on the individual specimens' dimensions, only the total thickness of CoDiCo SMC specimens was considered, neglecting the influence of varying ply thicknesses.

An analysis of the DiCo SMC microstructure in $CoDiCo^{0/90}$ SMC specimens revealed that the shell-core effect, that is already known from SMC (Le et al., 2008; Trauth, 2020), was more notable in CoDiCo SMC (Trauth, 2020) and even more pronounced in $CoDiCo^{0/90}$ SMC. Going from the center of the plaque (charge region) towards the edges of the plaque (flow region), the amount of fiber bundle splicing and curvature increased strongly and hardly any intact bundles were observed in the flow region (Figure 3.7). These microstructural variations might have also been responsible for a changed damage behavior. Although

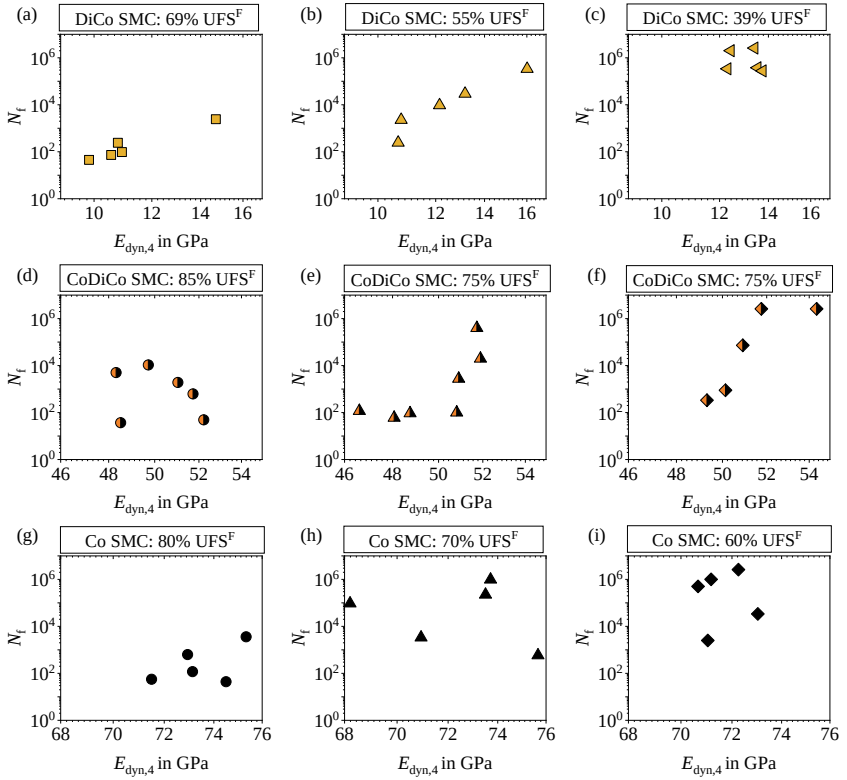

Figure 6.7: Fatigue life over initial dynamic modulus of (a)-(c) DiCo SMC, (d)-(f) CoDiCo SMC and (g)-(i) Co SMC at different stress levels under bending fatigue load.

this effect was more pronounced for CoDiCo$^{0/90}$ SMC specimens, scatter of the corresponding S-N data was smaller than in to CoDiCo SMC. This is probably due to a single damage mechanism, namely the initiation and growth of cracks in the 90° ply, dominating the fatigue damage behavior.

7 Summary and Conclusions

7.1 Summary

Within the framework of the International Research Group GRK 2078 "Integrated engineering of continuous-discontinuous long fiber-reinforced polymer structures", continuous-discontinuous sheet molding compounds (CoDiCo SMC) based on a two-step curing unsaturated polyester-polyurethane hybrid (UPPH) resin have been extensively investigated. Research in the fields of technology, design, simulation and characterization aims to provide a fundamental understanding of the material, the processing and the structural behavior. The work presented in this thesis was conducted within the framework of the GRK 2078 and focused on the fatigue behavior of such hybrid composites and effects of hybridization under cyclic loading. In line with the research questions defined in Section 2.6, this chapter summarizes the main results of this thesis.

Fatigue behavior of UPPH-based continuous and discontinuous SMC

Experimental investigations of the fatigue behavior of UPPH-based discontinuous SMC (DiCo SMC) and continuous SMC (Co SMC) were carried out to evaluate their properties in comparison with conventional continuous and discontinuous FRP. In addition, the investigations provided a basis for evaluating hybridization effects.

The stress-life behavior of the DiCo SMC investigated in this study was comparable to that of conventional SMC composites, which are mainly based on polyester,

vinyl ester, or epoxy resin and filled with $CaCO_3$ particles. The fatigue strength decreased by approximately 10 % with each decade of cycles. However, scatter was more pronounced than for other material systems. Stiffness steadily decreased and stiffness loss ranged from 11 % to 14 % after 90 % of the fatigue life under tension-tension loading. This was slightly lower than the values determined for SMC composites studied by other authors. Stiffness degradation was mainly attributed to transverse matrix cracking. Stiffness loss under flexural fatigue loading ranged between 20 % and 23 % after 90 % of the fatigue life.

The fatigue strength of the UPPH-based Co SMC, expressed in absolute values, was significantly lower than that of unidirectional CFRPs studied by other authors. Reasons are lower mechanical properties of the fibers, that were used in this study, as well as a slightly lower impregnation quality compared to CFRPs that were manufactured in conventional processes (e.g. autoclave). By normalizing the results to ultimate tensile strength, S-N behavior was comparable. However, scatter was much more pronounced in the composite investigated in this thesis. The stiffness degradation curves exhibited several jumps. These were attributed to fiber cluster fractures, some of which occurred early in fatigue life and in a highly stochastic manner. No experimental stiffness degradation data were presented by the other authors.

Effects of hybridization on fatigue properties

While hybridization resulted in a 126 % and 92 % increase in tensile strength (compared to DiCo SMC) at quasi-static strain rate and fatigue strain rate, respectively, the effect on fatigue strength was even more pronounced. Under tension-tension load, the stress level at which all specimens withstood at least $2.6 \cdot 10^6$ cycles was increased by 209 %. This could be explained by a change of mechanisms from a Co SMC dominated damage behavior under monotonic loading to a DiCo SMC dominated damage behavior under cyclic loading. When expressing S-N data in terms of initial maximum strain instead of maximum stress, the results further showed, that hybrid CoDiCo SMC performed better than both of Co SMC and DiCo SMC in the high cycle fatigue range. The fatigue ratio of CoDiCo SMC was

higher compared to both of its components. In addition, the relative stiffness loss was less pronounced with between 5 % and 9 % shortly before ultimate failure. Due to the sandwich-like structure of the specimens, the effect of hybridization was even more pronounced under bending fatigue load. For CoDiCo SMC, the fatigue strength was 258 % higher than for DiCo SMC. The stiffness reduction ranged between 4 % and 16 % after 90 % of fatigue life.

Experimental techniques for fatigue damage analysis

Results from microscopic examinations of the specimen edges were successfully used to analyze effects of hybridization on the DiCo SMC ply in terms of damage mechanisms and damage evolution. During interrupted tension-tension fatigue tests, matrix cracks were observed in both the DiCo SMC specimens and the DiCo SMC ply of the hybrid specimens, which were the main drivers for stiffness degradation. The observations also allowed for a quantitative analysis of matrix crack densities.

Effects of hybridization on the damage behavior

Reinforcement with Co SMC hardly affected the damage behavior of the DiCo SMC ply in the hybrid. The evolution of crack density was comparable to that observed in DiCo SMC specimens. It can be assumed, that the extent of stiffness degradation was also comparable. In contrast, the damage behavior of Co SMC was strongly influenced by hybridization. Effects of hybridization were due to residual stresses resulting from compression molding and a change in damage development leading to a better exploitation of the carbon fiber properties.

Effects of a cross-ply continuous reinforcement

This thesis also investigated a hybrid composite reinforced with a 0° and a 90° Co SMC ply on both sides. The 0° ply was located at the surface, while the 90°

ply was adjacent to the DiCo SMC ply. Cyclic loading resulted in early crack initiation in the 90° plies, even at comparatively low applied stresses. With an average ply thickness of 0.32 mm, these cracks were considerably large. They triggered delamination between the 0° ply and the 90° ply and also grew into the adjacent DiCo SMC. Aside from these large cracks, whose coalescence led to the final separation of the specimens, hardly any transverse matrix crack developed in the DiCo SMC ply. This damage evolution resulted in significantly higher stiffness loss of more than 12 % on average at 90 % of fatigue life. While tensile strength at quasi-static strain rate and fatigue strain rate increased by 94 % and 71 %, respectively, compared to DiCo SMC, fatigue strength at $2.6 \cdot 10^6$ cycles increased by 85 %. The fatigue ratio of the hybrid composite was comparable to that of DiCo SMC.

Effects of frequency and temperature

The fatigue behavior of discontinuous glass fiber SMC and unidirectional CFRP is known to be largely insensitive to different frequencies, especially as long as they are in a range where thermal induced fatigue plays a minor role. As expected, CoDiCo SMC was also unaffected by frequency, at least in the investigated frequency range between 1 Hz and 10 Hz.

In contrast, it is well known that mechanical properties of DiCo SMC are affected by temperature. This was also observed for the DiCo SMC examined in this thesis in bending fatigue tests conducted at -20 °C, 21 °C and 80 °C. The average fatigue strengths at -20 °C and 80 °C differed by more than 50 MPa in the high cycle fatigue range. Unidirectional CFRP is not known to exhibit significant temperature dependence in this temperature range. Nevertheless, the fatigue behavior of CoDiCo SMC was strongly influenced by temperature. The fatigue strength at 80 °C was reduced by more than 170 MPa and by more than 260 MPa in the low and high cycle fatigue range, respectively, compared to results obtained at -20 °C. The influence of temperature was thus far more pronounced than in DiCo SMC.

Fatigue life prediction modeling

A phenomenological model can provide a good first lifetime estimation for the CoDiCo SMC composite investigated in this thesis. The model presented here approximates the S-N behavior of CoDiCo SMC based on the volume ratio and initial stiffness ratio of DiCo SMC and Co SMC under the assumption that a stress, that is applied to the hybrid, equals the fatigue strength of the hybrid at a specific number of cycles, if it results in a stress in the DiCo SMC ply, that equals the fatigue strength of DiCo SMC at the same number of cycles. A more profound modeling approach, that accounts for changing stiffness ratios during cyclic loading could lead to a better fatigue life assessment. However, such a phenomenological model is, however, not transferable to arbitrary configurations of CoDiCo SMC composites. Changing the ply thicknesses and/or orientations would lead to different mechanisms, that are not captured in the model at hand.

7.2 Conclusions and Outlook

Hybrid composites combining a discontinuous glass fiber reinforcement and a continuous carbon fiber reinforcement have been shown to offer great potential for structural applications due to their excellent mechanical properties combined with high geometric flexibility and low manufacturing time and costs. The experimental results presented in this thesis highlight in particular their advantages under cyclic loading conditions. It is essential to consider, that hybridization effects under cyclic loading are less pronounced, when continuous reinforcements other than unidirectional ones are used. In addition, the temperature sensitivity of CoDiCo SMC is particularly critical and must be taken into account when dimensioning CoDiCo SMC components.

Although this thesis provided notable contributions to understand the fatigue behavior of CoDiCo SMC, additional research is needed for an all-encompassing characterization. The following points are of particular interest for further investigations:

- Experimental investigation focused on the fatigue behavior in flow direction. Since the examined materials are highly anisotropic, future experimental investigations should also assess mechanical properties in 90° direction.
- Not only the mechanical properties, but also damage evolution is anisotropic. Stiffness degradation measurements were only carried out in the direction of loading. The effect that a unidirectional load has on the properties in transverse direction remains to be investigated.
- While only tension-tension and bending fatigue loads were considered in this thesis, future investigations should also focus on tension-compression and compression-compression as well as multi-axial loading conditions.
- This thesis focused on hybrid composites combining DiCo SMC and Co SMC in two different configurations. Since hybridization effects depend on various factors, such as the relative amount of the different fibers, their mechanical properties (e.g. elastic properties, failure strain ratio and fiber strength distribution) and the degree of dispersion, the results presented here are not readily transferable to arbitrary material configurations. The development of more profound models, that capture effects of hybridization on the mechanistic level, is necessary to reduce experimental effort in the future and to efficiently design hybrid CoDiCo SMC components.

List of Figures

List of Tables

List of Publications

Journal articles

M. Bartkowiak, L. Schöttl, P. Elsner, and K.A. Weidenmann. Combined in-situ x-ray computed tomography and acoustic emission analysis for composite characterization - a feasibility study. *Key Engineering Materials*, 809:604–609, 2019. doi: 10.4028/www.scientific.net/KEM.809.604.

M. Bartkowiak, M. Kizak, W.V. Liebig, and K.A. Weidenmann. Fatigue behavior of hybrid continuous-discontinuous fiber-reinforced sheet molding compound composites under application-related loading conditions. *Composites Part C: Open Access*, 8:100265, 2022a. doi: 10.1016/j.jcomc.2022.100265.

M. Bartkowiak, W.V. Liebig, J. Montesano, and K.A. Weidenmann. Effects of hybridization on the tension-tension fatigue behavior of continuous-discontinuous sheet molding compounds. *International Journal of Fatigue*, 161:106879, 2022b. doi: 10.1016/j.ijfatigue.2022.106879.

Conference contributions

M. Bartkowiak, H. Weit, J. Montesano, and K. A. Weidenmann. Characterization of discontinuous fiber reinforced sheet molding compounds under tension-tension fatigue load. In *Proceedings of the American Society for Composites—Thirty-fourth Technical Conference*, Atlanta, USA, September 2019.

M. Bartkowiak, W.V. Liebig, and K.A. Weidenmann. Fatigue damage behavior of continuous-discontinuous fiber reinforced sheet molding compounds. In *Proceedings of the 4th International Conference Hybrid 2020 Materials and Structures*, pages 71–77, Karlsruhe, Germany, April 2020.

S. Revfi, A. Albers, N. Meyer, L. Kärger, L. Schöttl, M. Bartkowiak, and K. Behdinan. Manufacturing simulation of sheet molding compound (SMC). In *Proceedings of the NAFEMS World Congress 2021*, Online-Conference, October 2021.

Supervised student theses

M.I. Aliano Ramos. Experimental investigation of the degradation behavior of continuous-discontinuous fiber-reinforced plastics under cyclic loading. Master's thesis (not published), Karlsruhe Institute of Technology, 2021.

D. Beyer. Experimentelle Untersuchung der Biegeermüdungseigenschaften von diskontinuierlich glasfaserverstärkten Sheet Molding Compounds. Bachelor's thesis (not published), Karlsruhe Institute of Technology, 2019.

P. Hardy. Temperatur- und Frequenzabhängigkeit des Ermüdungsverhaltens von DiCo SMC und CoDiCo SMC. Bachelor's thesis (not published), Karlsruhe Institute of Technology, 2020.

M. Kizak. Experimental analysis of the bending fatigue properties of continuous-discontinuous sheet molding compound composites. Masters's thesis (not published), Karlsruhe Institute of Technology, 2020.

T. Nuber. Modellierung der Steifigkeitsdegradation eines kontinuierlich-diskontinuierlich faserverstärkten Kunststoffs. Master's thesis (not published), Karlsruhe Institute of Technology, 2021.

H. Weit. Experimentelle Untersuchung der Ermüdungseigenschaften von Sheet Molding Compounds unter Zugbelastung. Bachelor's thesis (not published), Karlsruhe Institute of Technology, 2019.

Bibliography

K. Akiyama. Development of PCM (prepreg compression molding) technology. In *Proceedings of the Automotive Lightweight Procurement Symposium, Düsseldorf, Germany*, pages 1–37, 2014.

M. Alves and S. Pimenta. A computationally-efficient micromechanical model for the fatigue life of unidirectional composites under tension-tension loading. *International Journal of Fatigue*, 116(11):677–690, 2018. ISSN 01421123. doi: 10.1016/j.ijfatigue.2018.05.017.

M. F. Ashby. *Materials selection in mechanical design*. Elsevier/Butterworth-Heinemann, Amsterdam, Netherlands, 4th edition, 2011. ISBN 9781856176637. URL http://www.loc.gov/catdir/enhancements/fy1606/2010020691-d.html.

F. Aymerich and S. Meili. Damage assessment in an SMC composite by means of ultrasonic techniques. *NDT.net*, 4(3):1–7, 1999. URL https://www.ndt.net/article/v04n03/7/7.htm.

F. Aymerich and S. Meili. Ultrasonic evaluation of matrix damage in impacted composite laminates. *Composites Part B: Engineering*, 31(1):1–6, 2000. ISSN 13598368. doi: 10.1016/S1359-8368(99)00067-0.

AZO. E-glass fibre, 2021. URL https://www.azom.com/properties.aspx?ArticleID=764. accessed on 23 November 2021.

V. Barron, M. Buggy, and N. H. McKenna. Frequency effects on the fatigue behaviour on carbon fibre reinforced polymer laminates. *Journal of Materials Science*, 36(7):1755–1761, 2001. ISSN 00222461. doi: 10.1023/A:1017576725885.

M. Bartkowiak, L. Schöttl, P. Elsner, and K. A. Weidenmann. Combined in-situ X-ray computed tomography and acoustic emission analysis for composite characterization - a feasibility study. *Key Engineering Materials*, 809:604–609, 2019. doi: 10.4028/www.scientific.net/KEM.809.604.

BASF. Lupranat M20 R, 2019. URL `https://chemicals.basf.com/global/monomers/tds_isocyanate/lupranat/Lupranat%20M20R.pdf`. accessed on 23 November 2021.

V. Bellenger, A. Tcharkhtchi, and P. Castaing. Thermal and mechanical fatigue of a PA66/glass fibers composite material. *International Journal of Fatigue*, 28 (10):1348–1352, 2006. ISSN 01421123. doi: 10.1016/j.ijfatigue.2006.02.031.

M. R. Bhat, M. A. Majeed, and C.R.L. Murthy. Characterization of fatigue damage in unidirectional GFRP composites through acoustic emission signal analysis. *NDT & E International*, 27(1):27–32, 1994. ISSN 09638695. doi: 10.1016/0963-8695(94)90007-8.

T. Böhlke, L. Kärger, K. A. Weidenmann, and F. Henning. Continuous-discontinuous long fiber-reinforced polymer structures: Modeling, characterization and validation (presentation). In *AFBW AG Composite-Simulation*, Karlsruhe, Germany, 2016.

T. Böhlke, F. Henning, A. Hrymak, L. Kärger, K. A. Weidenmann, and J. T. Wood. *Continuous–Discontinuous Fiber-Reinforced Polymers*. Carl Hanser Verlag GmbH & Co. KG, Munich, Germany, 2019. ISBN 978-1-56990-692-7. doi: 10.3139/9781569906934.

Borchers. Borchi Kat 0243, 2021. URL `https://www.borchers.com/wp-content/uploads/2019/06/Borchi-Kat-0243-TDS-L029116.pdf`. accessed on 23 November 2021.

P. E. Bourban, A. Bögli, F. Bonjour, and J.-A.E. Månson. Integrated processing of thermoplastic composites. *Applied Mechanics Reviews*, 58(5):633–637, 1998. ISSN 0266-3538. doi: 10.1016/S0266-3538(97)00135-8.

M. Bruderick, D. Denton, M. Shinedling, and M. Kiesel. Applications of carbon fiber SMC for the Dodge Viper. In *Proceedings of the Automotive Composites Conference & Exhibition*, pages 1–10, Detroit, USA, 2013.

D. Bücheler. *Locally Continuous-fiber Reinforced Sheet Molding Compound.* Dissertation, Karlsruher Institut für Technologie (KIT), Karlsruhe, Germany, 2018. URL http://nbn-resolving.de/urn:nbn:de:swb:90-791635.

D. Bücheler and F. Henning. Hybrid resin improves position and alignment of continuously reinforced prepreg during compression co-molding with sheet molding compound. In *Proceedings of the 17th European Conference on Composite Materials*, pages 26–30, Munich, Germany, 2016.

BYK. BYK-P 9085 Data Sheet, 2012. URL https://www.byk.com/en/products/additives-by-name/byk-p-9085. accessed on 23 November 2021.

BYK. BYK 9076 Data Sheet, 2014. URL https://www.byk.com/en/products/additives-by-name/byk-9076. accessed on 23 November 2021.

BYK. BYK-A 530 Data Sheet, 2016. URL https://www.byk.com/en/products/additives-by-name/byk-a-530. accessed on 23 November 2021.

C. C. Chamis and J. H. Sinclair. Analysis/design of strip reinforced random composites (strip hybrids). In *American Society of Mechanical Engineers, Winter Annual Meeting*, pages 1–10, San Francisco, California, USA, 1978.

ChemBK. Trigonox 117, 2015. URL https://www.chembk.com/en/chem/Trigonox%20117. accessed on 23 November 2021.

A. S. Chen and B. Harris. Fatigue-induced damage mechanisms in carbon fibre-reinforced plastic composites. *Journal of Materials Science*, 28(8):2013–2027, 1993. ISSN 00222461. doi: 10.1007/BF00367557.

H.-S. Chen and S.-F. Hwang. Accelerated fatigue properties of unidirectional carbon/epoxy composite materials. *Polymer Composites*, 27(2):138–146, 2006. ISSN 02728397. doi: 10.1002/pc.20181.

D. M. Corbridge, L. T. Harper, D.S.A. de Focatiis, and N. A. Warrior. Compression moulding of composites with hybrid fibre architectures. *Composites Part A: Applied Science and Manufacturing*, 95:87–99, 2017. ISSN 1359835X. doi: 10.1016/j.compositesa.2016.12.018.

J. Degrieck and W. van Paepegem. Fatigue damage modeling of fibre-reinforced composite materials: Review. *Applied Mechanics Reviews*, 54(4):279–300, 2001. ISSN 0266-3538. doi: 10.1115/1.1381395.

D. L. Denton. Mechanical properties characterization of an SMC-R50 composite. *SAE Transactions*, 88(3):2283–2294, 1979.

R.F. Dickson, G. Fernando, T. Adam, H. Reiter, and B. Harris. Fatigue behaviour of hybrid composites. *Journal of materials science*, 24(1):227–233, 1989.

DIN EN 13554. *Non-destructive testing – Acoustic emission testing – General principles*. Deutsches Institut für Normung e.V., Beuth Verlag GmbH, Berlin, Germany, 2011.

DIN EN ISO 14125. *Faserverstärkte Kunststoffe - Bestimmung der Biegeeigenschaften.* Deutsches Institut für Normung e.V., Beuth Verlag GmbH, Berlin, Germany, 2011.

DIN EN ISO 527-4. *Kunststoffe - Bestimmung der Zugeigenschaften: Teil 4: Prüfbedingungen für isotrop und anisotrop faserverstärkte Kunststoffverbundwerkstoffe*. Deutsches Institut für Normung e.V., Beuth Verlag GmbH, Berlin, Germany, 1997.

DIN EN ISO 527-5. *Kunststoffe - Bestimmung der Zugeigenschaften: Teil 5: Prüfbedingungen für unidirektional faserverstärkte*. Deutsches Institut für Normung e.V., Beuth Verlag GmbH, Berlin, Germany, 2010.

DSM. Product Data Sheet: Daron 41/B1, 2012.

N. A. Dugin, T. M. Zaboronkova, C. Krafft, and G. R. Belyaev. Carbon-based composite microwave antennas. *Electronics*, 9:129–145, 2020.

G. M. Ehrenstein. *Faserverbund-Kunststoffe: Werkstoffe - Verarbeitung - Eigenschaften*. Carl Hanser Verlag GmbH & Co. KG, Munich, Germany, 2nd edition, 2006. ISBN 978-3-446-22716-3. doi: 10.3139/9783446457546. URL http://dx.doi.org/10.3139/9783446457546.

A. D. Evans. *Hybrid carbon fibre architectures for high performance, high volume applications*. PhD thesis, University of Nottingham, Nottingham, UK, 2018.

B. Fazlali, S.V. Lomov, and Y. Swolfs. Fiber break model for tension-tension fatigue of unidirectional composites. *Composites Part B: Engineering*, 220: 108970, 2021. ISSN 13598368. doi: 10.1016/j.compositesb.2021.108970.

M. Fette, M. Hentschel, F. Köhler, J. Wulfsberg, and A. Herrmann. Automated and cost-efficient production of hybrid sheet moulding compound aircraft components. *Procedia Manufacturing*, 6(3):132–139, 2016. ISSN 23519789. doi: 10.1016/j.promfg.2016.11.017.

M. Fette, M. Hentschel, J. G. Santafe, T. Wille, H. Büttemeyer, and P. Schiebel. New methods for computing and developing hybrid sheet molding compound structures for aviation industry. *Procedia CIRP*, 66:45–50, 2017. ISSN 22128271. doi: 10.1016/j.procir.2017.03.289.

E. K. Gamstedt. Effects of debonding and fiber strength distribution on fatigue-damage propagation in carbon fiber-reinforced epoxy. *Journal of Applied Polymer Science*, 76(4):457–474, 2000. ISSN 0021-8995. doi: 10.1002/(SICI)1097-4628(20000425)76:4{\textless}457::AID-APP3{\textgreater}3.0.CO;2-L.

K. W. Gan, Y. W. Ho, Z. Y. Ow, H. A. Israr, and K. J. Wong. Aligned discontinuous carbon fibre tows in hybrid composites and their tensile behaviour: An experimental study. *Journal of Composite Materials*, 53(26-27):3893–3907, 2019. ISSN 0021-9983. doi: 10.1177/0021998319849697.

G. Gardiner. Teaming to define what automotive CFRP could be, 2018. URL https://www.compositesworld.com/articles/teaming-to-define-what-automotive-cfrp-could-be. accessed on 23 November 2021.

K. W. Garrett and J. E. Bailey. Multiple transverse fracture in 90 cross-ply laminates of a glass fibre-reinforced polyester. *Journal of Materials Science*, 12(1):157–168, 1977. ISSN 00222461. doi: 10.1007/BF00738481.

R. F. Gibson and A. Yau. Complex moduli of chopped fiber and continuous fiber composites: Comparison of measurements with estimated bounds. *Journal of Composite Materials*, 14(2):155–167, 1980. ISSN 0021-9983. doi: 10.1177/002199838001400207.

F. Gortner, L. Medina, and P. Mitschang. Advanced SMC-processing in combination with textile reinforcements. In *Proceedings of the 20th International Conference on Composite Materials*, pages 19–24, Copenhagen, Denmark, 2015a.

F. Gortner, L. Medina, and P. Mitschang. Influence of textile reinforcement on bending properties and impact strength of SMC-components. *KMUTNB International Journal of Applied Science and Technology*, 8(4):259–269, 2015b. ISSN 1906151X. doi: 10.14416/j.ijast.2015.07.005.

H. T. Hahn and R. Y. Kim. Fatigue behavior of composite laminate. *Journal of Composite Materials*, 10(2):156–180, 1976. ISSN 0021-9983. doi: 10.1177/002199837601000205.

K. Handa, A. Kato, and I. Narisawa. Fatigue characteristics of a glass-fiber-reinforced polyamide. *Journal of Applied Polymer Science*, 72(13):1783–1793, 1999. ISSN 0021-8995. doi: 10.1002/(SICI)1097-4628(19990624)72:13<1783::AID-APP14>3.0.CO;2-B.

T. Hayashi. On the improvement of mechanical properties of composites by hybrid composition. In *Proceedings of the 8th International Reinforced Plastics Conference*, pages 149–152, London, UK, 1972.

R. A. Heimbuch and B. A. Sanders. Mechanical properties of automotive chopped fiber reinforced plastics. *Composite Materials in the Automobile Industry*, 12 (4):111–139, 1978.

F. Henning, K. A. Weidenmann, and B. Bader. Hybride Werkstoffverbunde. In F. Henning and E. Moeller, editors, *Handbuch Leichtbau*, pages 413–428. Carl Hanser Verlag GmbH & Co. KG, Munich, Germany, 2011. doi: 10.3139/9783446428911.016.

A. L. Highsmith and K. L. Reifsnider. Stiffness-reduction mechanisms in composite laminates. In K. L. Reifsnider, editor, *Damage in Composite Materials: Basic Mechanisms, Accumulation, Tolerance, and Characterization*, pages 103–117. ASTM International, West Conshohocken, PA, USA, 1982. ISBN 978-0-8031-0696-3. doi: 10.1520/STP34323S.

K.E. Hofer, M. Stander, and L.C. Bennett. Degradation and enhancement of the fatigue behavior of glass/graphite/epoxy hybrid composites after accelerated aging. *Polymer Engineering & Science*, 18(2):120–127, 1978.

R. J. Howe and M. J. Owen. Cumulative damage in chopped strand mat/polyester resin laminates. In *Proceedings of the 8th international reinforced plastics conference*, pages 137–148, London, UK, 1972.

Z.M. Huang and Y.X. Zhou. *Strength of fibrous composites*. Springer Science & Business Media, Berlin, Germany, 2012.

W. Hwang and K. S. Han. Cumulative damage models and multi-stress fatigue life prediction. *Journal of Composite Materials*, 20(2):125–153, 1986. ISSN 0021-9983. doi: 10.1177/002199838602000202.

ISO 13003. *Fibre-reinforced plastics - Determination of fatigue properties under cyclic loading conditions*. International Organization for Standardization, Geneva, Switzerland, 2003.

Z. Jendli, F. Meraghni, J. Fitoussi, and D. Baptiste. Micromechanical analysis of strain rate effect on damage evolution in sheet molding compound composites. *Composites Part A: Applied Science and Manufacturing*, 35(7-8):779–785, 2004. ISSN 1359835X. doi: 10.1016/j.compositesa.2004.01.020.

R. C. S. F. Júnior and A. S. Belísio. Probabilistic S–N curves using exponential and power laws equations. *Composites Part B: Engineering*, 56:582–590, 2014. doi: 10.1016/j.compositesb.2013.08.036.

R. B. Jutte and O. C. Fiberglas. Structural SMC - Material, process and performance review. In *Proceedings of the 29th Meeting of the Mechanical Failures Prevention Group*, page 108, Gaithersburg, Maryland, USA, 1979.

L. M. Kachanov. *Introduction to continuum damage mechanics*, volume 10 of *Monographs and textbooks on mechanics of solids and fluids Mechanics of elastic stability*. Kluwer Academic Publishers Group, Dordrecht, Netherlands, 2nd edition, 1990. ISBN 90-247-3319-7.

M. Kawai and K. Yano. Anisomorphic constant fatigue life diagrams of constant probability of failure and prediction of P–S–N curves for unidirectional carbon/epoxy laminates. *International Journal of Fatigue*, 83(163–186):323–334, 2016. ISSN 01421123. doi: 10.1016/j.ijfatigue.2015.11.005.

M. Kawai, S. Yjima, A. Hachinohe, and Y. Takano. Off-axis fatigue behavior of unidirectional carbon fiber-reinforced composites at room and high temperatures. *Journal of Composite Materials*, 35(7):545–576, 2001. ISSN 0021-9983. doi: 10.1177/002199801772662073.

J. F. Kay. Advances in a structural sheet molding compound. *Journal of Composites Technology and Research*, 4(4):110–115, 1982. ISSN 08846804. doi: 10.1520/CTR10772J.

M. L. Kehrer. *Thermomechanical mean-field modeling and experimental characterization of long fiber-reinforced sheet molding compound composites*, volume 15. KIT Scientific Publishing, Karlsruhe, Germany, 2019.

H. S. Kliger. Development and experimental verification of design values for carbon-glass hybrid sandwich composites. *Composite Materials in the Automobile Industry*, 115:51–65, 1978.

D. Krajcinovic and J. Lemaitre, editors. *Continuum Damage Mechanics Theory and Application*, volume 295 of *International Centre for Mechanical Sciences,*

Courses and Lectures. Springer, Vienna, Italy, 1987. ISBN 978-3-7091-2806-0. doi: 10.1007/978-3-7091-2806-0.

S. V. Kulkarni, C. H. Zweben, R. B. Pipes, G. Epstein, and E.G Wolff, editors. *Composite materials in the automobile industry*. The American Society of Mechanical Engineers, New York, USA, 1978.

R. Kundrat, S. Joneja, and L. J. Broutman. Fatigue damage studies in high strength sheet-molding compound fiberglass composites. *Polymer Composites*, 3(3):105–112, 1982. ISSN 02728397. doi: 10.1002/pc.750030302.

N. Laws and G. J. Dvorak. The effect of fiber breaks and aligned penny-shaped cracks on the stiffness and energy release rates in unidirectional composites. *International Journal of Solids and Structures*, 23(9):1269–1283, 1987. ISSN 00207683. doi: 10.1016/0020-7683(87)90105-3.

T.-H. Le, P.J.J. Dumont, L. Orgéas, D. Favier, L. Salvo, and E. Boller. X-ray phase contrast microtomography for the analysis of the fibrous microstructure of SMC composites. *Composites Part A: Applied Science and Manufacturing*, 39(1): 91–103, 2008. ISSN 1359835X. doi: 10.1016/j.compositesa.2007.08.027.

X. Li, M. Saeedifar, R. Benedictus, and D. Zarouchas. Damage accumulation analysis of cfrp cross-ply laminates under different tensile loading rates. *Composites Part C: Open Access*, 1:100005, 2020. ISSN 26666820. doi: 10.1016/j.jcomc.2020.100005.

J. Llobet, P. Maimí, J. A. Mayugo, Y. Essa, and F. La Martin de Escalera. A fatigue damage and residual strength model for unidirectional carbon/epoxy composites under on-axis tension-tension loadings. *International Journal of Fatigue*, 103 (10):508–515, 2017. ISSN 01421123. doi: 10.1016/j.ijfatigue.2017.06.026.

P. K. Mallick. Effect of fiber misorientation on the tensile strength of compression molded continuous fiber composites. *Polymer Composites*, 7(1):14–18, 1986. ISSN 02728397. doi: 10.1002/pc.750070104.

P. Malnati. Prepreg compression molding makes its commercial debut. *Composites World*, 2015. URL `https://www.compositesworld.com/articles`

/prepreg-compression-molding-makes-its-commercial-debut. accessed on 25 Mai 2022.

J. F. Mandell and U. Meier. Effects of stress ratio, frequency, and loading time on the tensile fatigue of glass-reinforced epoxy. In T. K. O'Brien, editor, *Long-Term Behavior of Composites*. ASTM International, West Conshohocken, PA, USA, 1983. ISBN 978-0-8031-0252-1. doi: 10.1520/STP31816S.

P. W. Manders and M. G. Bader. The strength of hybrid glass/carbon fibre composites. *Journal of Materials Science*, 16(8):2246–2256, 1981. ISSN 00222461. doi: 10.1007/BF00542387.

L. Maragoni, P. A. Carraro, M. Peron, and M. Quaresimin. Fatigue behaviour of glass/epoxy laminates in the presence of voids. *International Journal of Fatigue*, 95(1):18–28, 2017. ISSN 01421123. doi: 10.1016/j.ijfatigue.2016.10.004.

G. Marom, S. Fischer, F. R. Tuler, and H. D. Wagner. Hybrid effects in composites: conditions for positive or negative effects versus rule-of-mixtures behaviour. *Journal of Materials Science*, 13(7):1419–1426, 1978. ISSN 00222461. doi: 10.1007/BF00553194.

N. Meyer, L. Schöttl, L. Bretz, A. N. Hrymak, and L. Kärger. Direct bundle simulation approach for the compression molding process of sheet molding compound. *Composites Part A: Applied Science and Manufacturing*, 132(1):105809, 2020. ISSN 1359835X. doi: 10.1016/j.compositesa.2020.105809.

I. Miskdjian, M. Hajikazemi, and W. van Paepegem. Automatic edge detection of ply cracks in glass fiber composite laminates under quasi-static and fatigue loading using multi-scale digital image correlation. *Applied Mechanics Reviews*, 200:108401, 2020. ISSN 0266-3538. doi: 10.1016/j.compscitech.2020.108401.

Y. Miyano, M. K. McMurray, J. Enyama, and M. Nakada. Loading rate and temperature dependence on flexural fatigue behavior of a satin woven CFRP laminate. *Journal of Composite Materials*, 28(13):1250–1260, 1994. ISSN 0021-9983. doi: 10.1177/002199839402801305.

Y. Miyano, M. Nakada, H. Kudoh, and R. Muki. Prediction of tensile fatigue life under temperature environment for unidirectional CFRP. *Advanced Composite Materials*, 8(3):235–246, 1999. ISSN 0924-3046. doi: 10.1163/156855199X00236.

R. Mohammadi, M. A. Najafabadi, M. Saeedifar, J. Yousefi, and G. Minak. Correlation of acoustic emission with finite element predicted damages in open-hole tensile laminated composites. *Composites Part B: Engineering*, 108(3): 427–435, 2017. ISSN 13598368. doi: 10.1016/j.compositesb.2016.09.101.

J. Montesano. *Fatigue damage characterization of braided and woven fiber reinforced polymer matrix composites at room and elevated temperatures*. PhD thesis, Department of Aerospace Engineering, Ryerson University, Toronto, ON, Canada, 2012.

J. Montesano, M. Selezneva, Z. Fawaz, C. Poon, and K. Behdinan. Elevated temperature off-axis fatigue behavior of an eight-harness satin woven carbon-fiber/bismaleimide laminate. *Composites Part A: Applied Science and Manufacturing*, 43(9):1454–1466, 2012. ISSN 1359835X. doi: 10.1016/j.compositesa.2012.04.016.

J. Montesano, H. Bougherara, and Z. Fawaz. Application of infrared thermography for the characterization of damage in braided carbon fiber reinforced polymer matrix composites. *Composites Part B: Engineering*, 60:137–143, 2014. ISSN 13598368. doi: 10.1016/j.compositesb.2013.12.053.

J. Montesano, M. Selezneva, M. Levesque, and Z. Fawaz. Modeling fatigue damage evolution in polymer matrix composite structures and validation using in-situ digital image correlation. *Composite Structures*, 125:354–361, 2015. ISSN 02638223. doi: 10.1016/j.compstruct.2015.02.035.

S. Mortazavian and A. Fatemi. Fatigue behavior and modeling of short fiber reinforced polymer composites: A literature review. *International Journal of Fatigue*, 70:297–321, 2015. ISSN 01421123. doi: 10.1016/j.ijfatigue.2014.10.005.

V. Munoz, B. Valès, M. Perrin, M. L. Pastor, H. Welemane, A. Cantarel, and M. Karama. Damage detection in CFRP by coupling acoustic emission and infrared thermography. *Composites Part B: Engineering*, 85(3):68–75, 2016. ISSN 13598368. doi: 10.1016/j.compositesb.2015.09.011.

J. A. Nairn. On the use of shear-lag methods for analysis of stress transfer in unidirectional composites. *Mechanics of Materials*, 26(2):63–80, 1997. ISSN 01676636. doi: 10.1016/S0167-6636(97)00023-9.

J. A. Nairn and S. Hu. The formation and effect of outer-ply microcracks in cross-ply laminates: A variational approach. *Engineering Fracture Mechanics*, 41(2):203–221, 1992. ISSN 00137944. doi: 10.1016/0013-7944(92)90181-D.

C. Nony-Davadie, L. Peltier, Y. Chemisky, B. Surowiec, and F. Meraghni. Mechanical characterization of anisotropy on a carbon fiber sheet molding compound composite under quasi-static and fatigue loading. *Journal of Composite Materials*, 53(11):1437–1457, 2019. ISSN 0021-9983. doi: 10.1177/0021998318804612.

T. K. O'Brien and K. L. Reifsnider. Fatigue damage evaluation through stiffness measurements in boron-epoxy laminates. *Journal of Composite Materials*, 15 (1):55–70, 1981. ISSN 0021-9983. doi: 10.1177/002199838101500105.

L. Orgéas and P. J. J. Dumont. Sheet molding compounds. In L. Nicolais, editor, *Wiley Encyclopedia of Composites*, volume 32, page 541. John Wiley & Sons, Inc, Hoboken, NJ, USA, 2011. ISBN 9781118097298. doi: 10.1002/9781118097298.weoc222.

M. J. Owen. Static and fatigue strength of glass chopped strand mat/polyester resin laminates. In B. A. Sanders, editor, *Short Fiber Reinforced Composite Materials*, pages 64–84. ASTM International, West Conshohocken, PA, USA, 1982. ISBN 978-0-8031-0697-0. doi: 10.1520/STP29379S.

M. J. Owen and R. J. Howe. The accumulation of damage in a glass-reinforced plastic under tensile and fatigue loading. *Journal of Physics D: Applied Physics*, 5(9):1637–1649, 1972. ISSN 0368-3931. doi: 10.1088/0022-3727/5/9/319.

P. Potstada, S. Rosini, M. Mavrogordato, I. Sinclair, S. M. Spearing, and M. Sause. Cross-validation of single filament failure by acoustic emission and high-resolution synchrotron computed tomography. In *Proceedings of the 18th European Conference on Composite Materials*, pages 1–8, Athens, Greece, 2018.

A. Puck. *Zur Beanspruchung und Verformung von GFK-Mehrschichten-Verbund-Bauelementen.* Carl Hanser Verlag GmbH & Co. KG, Munich, Germany, 1967.

M. Quaresimin, P. A. Carraro, L. P. Mikkelsen, N. Lucato, L. Vivian, P. Brøndsted, B. F. Sørensen, J. Varna, and R. Talreja. Damage evolution under cyclic multiaxial stress state: A comparative analysis between glass/epoxy laminates and tubes. *Composites Part B: Engineering*, 61(3):282–290, 2014. ISSN 13598368. doi: 10.1016/j.compositesb.2014.01.056.

M. Quaresimin, P. A. Carraro, and L. Maragoni. Early stage damage in off-axis plies under fatigue loading. *Applied Mechanics Reviews*, 128(10):147–154, 2016. ISSN 0266-3538. doi: 10.1016/j.compscitech.2016.03.015.

K. L. Reifsnider, E. G. Henneke, W. W. Stinchcomb, and J. C. Duke. Damaga mechanics NDE of composite laminates. In *Mechanics of Composite Materials*, volume 2, pages 399–420. Elsevier, 1983. ISBN 9780080293844. doi: 10.1016/B978-0-08-029384-4.50032-8.

R. Renz, V. Alstadt, and G. W. Ehrenstein. Hysteresis measurements for characterizing the dynamic fatigue of R-SMC. *Journal of Reinforced Plastics and Composites*, 7(5):413–434, 1988. ISSN 0731-6844. doi: 10.1177/073168448800700502.

D. A. Riegner and B. A. Sanders. A characterization study of automotive continuous and random glass fiber composites. Technical Report GMMD 79-023, GM Manufacturing Development, General Motors Technical Center, Warren, Michigan, USA, 1979.

M. Saeedifar and D. Zarouchas. Damage characterization of laminated composites using acoustic emission: A review. *Composites Part B: Engineering*, 195(22): 108039, 2020. ISSN 13598368. doi: 10.1016/j.compositesb.2020.108039.

M.G.R. Sause, A. Gribov, A. R. Unwin, and S. Horn. Pattern recognition approach to identify natural clusters of acoustic emission signals. *Pattern Recognition Letters*, 33(1):17–23, 2012. ISSN 01678655. doi: 10.1016/j.patrec.2011.09.018.

L. Schöttl, P. Kolb, W. V. Liebig, K. A. Weidenmann, K. Inal, and P. Elsner. Crack characterization of discontinuous fiber-reinforced composites by using micro-computed tomography: Cyclic in-situ testing, crack segmentation and crack volume fraction. *Composites Communications*, 21:100384, 2020. ISSN 24522139. doi: 10.1016/j.coco.2020.100384.

L. Schöttl, W. V. Liebig, K. A. Weidenmann, K. Inal, and P. Elsner. The use of the empirical crack orientation tensor to characterize the damage anisotropy. *Composites Communications*, 25:100613, 2021. ISSN 24522139. doi: 10.1016/j.coco.2020.100613.

K. Schulte. Damage development under cyclic loading. In *Proceedings of the European Symposium on Damage Development and Failure Processes in Composite Materials*, pages 39–54, Leuven, Belgium, 1987.

K. Schulte and C. Baron. Load and failure analyses of CFRP laminates by means of electrical resistivity measurements. *Applied Mechanics Reviews*, 36(1):63–76, 1989. ISSN 0266-3538. doi: 10.1016/0266-3538(89)90016-X.

K. Schulte and W. W. Stinchcomb. Damage development near the edges of a composite specimen during quasi-static and fatigue loading. *Journal of Composites Technology and Research*, 6(1):3, 1984. ISSN 08846804. doi: 10.1520/CTR10876J.

A. I. Selmy, A. R. Elsesi, N. A. Azab, and M. A. Abd El-baky. Monotonic properties of unidirectional glass fiber (U)/random glass fiber (R)/epoxy hybrid composites. *Materials & Design*, 32(2):743–749, 2011. ISSN 02641275. doi: 10.1016/j.matdes.2010.07.031.

A. I. Selmy, A. R. Elsesi, N. A. Azab, and M. A. Abd El-baky. In-plane shear properties of unidirectional glass fiber (U)/random glass fiber (R)/epoxy hybrid

and non-hybrid composites. *Composites Part B: Engineering*, 43(2):431–438, 2012a. ISSN 13598368. doi: 10.1016/j.compositesb.2011.06.001.

A. I. Selmy, A. R. Elsesi, N. A. Azab, and M. A. Abd El-baky. Interlaminar shear behavior of unidirectional glass fiber (U)/random glass fiber (R)/epoxy hybrid and non-hybrid composite laminates. *Composites Part B: Engineering*, 43(4): 1714–1719, 2012b. ISSN 13598368. doi: 10.1016/j.compositesb.2012.01.031.

T. Shimokawa, Y. Kakuta, Y. Hamaguchi, and T. Aiyama. Static and fatigue strengths of a G40-800/5260 carbon fiber/bismaleimide composite material at room temperature and 150°C. *Journal of Composite Materials*, 42(7):655–679, 2008. ISSN 0021-9983. doi: 10.1177/0021998308088605.

M. Shirinbayan, J. Fitoussi, F. Meraghni, B. Surowiec, M. Bocquet, and A. Tcharkhtchi. High strain rate visco-damageable behavior of advanced sheet molding compound (A-SMC) under tension. *Composites Part B: Engineering*, 82(1):30–41, 2015. ISSN 13598368. doi: 10.1016/j.compositesb.2015.07.010.

M. Shirinbayan, J. Fitoussi, F. Meraghni, B. Surowiec, M. Laribi, and A. Tcharkhtchi. Coupled effect of loading frequency and amplitude on the fatigue behavior of advanced sheet molding compound (A-SMC). *Journal of Reinforced Plastics and Composites*, 36(4):271–282, 2017. ISSN 0731-6844. doi: 10.1177/0731684416682853.

Sigma-Aldrich. Styrene, 2021a. URL `https://www.sigmaaldrich.com/DE/de/product/mm/807679?context=product`. accessed on 23 November 2021.

Sigma-Aldrich. p-Benzochinon, 2021b. URL `https://www.sigmaaldrich.com/DE/de/product/mm/802410?context=product`. accessed on 23 November 2021.

A. Sjogran. Effects of temperature on delamination growth in a carbon/epoxy composite under fatigue loading. *International Journal of Fatigue*, 24(2-4): 179–184, 2002. ISSN 01421123. doi: 10.1016/S0142-1123(01)00071-8.

SN 214001:2010-03. *Contact-free cutting - Water jet cutting - Geometrical product specification and quality*. Swiss Association for Standardization, Winterthur, Switzerland, 2010.

B. F. Sørensen and Stergios Goutianos. Micromechanical model for prediction of the fatigue limit for unidirectional fibre composites. *Mechanics of Materials*, 131:169–187, 2019. ISSN 01676636. doi: 10.1016/j.mechmat.2019.01.023.

G. S. Springer. Effects of temperature and moisture on sheet molding compounds. *Journal of Reinforced Plastics and Composites*, 2(2):70–89, 1983. ISSN 0731-6844. doi: 10.1177/073168448300200201.

N. S. Sridharan. Elastic and strength properties of continuous/chopped glass fiber hybrid sheet molding compounds. In B. A. Sanders, editor, *Short Fiber Reinforced Composite Materials*, pages 167–182. ASTM International, West Conshohocken, PA, USA, 1982. ISBN 978-0-8031-0697-0. doi: 10.1520/STP29385S.

M. Such, C. Ward, and K. Potter. Aligned discontinuous fibre composites: A short history. *Journal of Multifunctional Composites*, 2(3):155–168, 2014. doi: 10.12783/issn.2168-4286/2/3/4/Such.

J. Summerscales and D. Short. Carbon fibre and glass fibre hybrid reinforced plastics. *Composites*, 9(3):157–166, 1978. ISSN 00104361. doi: 10.1016/0010-4361(78)90341-5.

Y. Swolfs, L. Gorbatikh, and I. Verpoest. Fibre hybridisation in polymer composites: A review. *Composites Part A: Applied Science and Manufacturing*, 67:181–200, 2014. doi: 10.1016/j.compositesa.2014.08.027.

G. Szebényi and V. Hliva. Detection of delamination in polymer composites by digital image correlation-experimental test. *Polymers*, 11(3), 2019. doi: 10.3390/polym11030523.

D. G. Taggart, R. B. Pipes, R. A. Blake, and J. W. Gillespie JR. Properties of SMC composites. Technical report, University of Delaware: Center for Composite Materials, 1979.

F. Taheri-Behrooz, M. M. Shokrieh, and L. B. Lessard. Progressive fatigue damage modeling of cross-ply laminates, II: Experimental evaluation. *Journal of Composite Materials*, 44(10):1261–1277, 2010. ISSN 0021-9983. doi: 10.1177/0021998309351605.

I. Taketa, T. Okabe, and A. Kitano. A new compression-molding approach using unidirectionally arrayed chopped strands. *Composites Part A: Applied Science and Manufacturing*, 39(12):1884–1890, 2008. ISSN 1359835X. doi: 10.1016/j.compositesa.2008.09.012.

R. Talreja. Fatigue of composite materials: damage mechanisms and fatigue-life diagrams. *Proceedings of the Royal Society of London. A. Mathematical and Physical Sciences*, 378(1775):461–475, 1981. ISSN 0080-4630. doi: 10.1098/rspa.1981.0163.

R. Talreja. Transverse cracking and stiffness reduction in composite laminates. *Journal of Composite Materials*, 19(4):355–375, 1985. ISSN 0021-9983. doi: 10.1177/002199838501900404.

R. Talreja and C. V. Singh. *Damage and failure of composite materials*. Cambridge University Press, Cambridge, UK, 2012. ISBN 978-0-521-81942-8. doi: 10.1017/CBO9781139016063.

S. Tamboura, M. A. Laribi, J. Fitoussi, M. Shirinbayan, R. Tie Bi, A. Tcharkhtchi, and H. Ben Dali. Damage and fatigue life prediction of short fiber reinforced composites submitted to variable temperature loading: Application to sheet molding compound composites. *International Journal of Fatigue*, 138(4): 105676, 2020. ISSN 01421123. doi: 10.1016/j.ijfatigue.2020.105676.

A. Trauth. *Characterisation and Modelling of Continuous-Discontinuous Sheet Moulding Compound Composites for Structural Applications*. KIT Scientific publishing, Karlsruhe, Germany, 2020. doi: 10.5445/IR/1000096578.

A. Trauth and K. A. Weidenmann. Continuous-discontinuous sheet moulding compounds – effect of hybridisation on mechanical material properties. *Composite Structures*, 202:1087–1098, 2018. ISSN 02638223. doi: 10.1016/j.compstruct.2018.05.048.

A. Trauth, D. Bücheler, F. Henning, and K. A. Weidenmann. Mechanical properties of unidirectional continuous carbon fiber reinforced sheet molding compounds. In *Proceedings of the 17th European Conference on Composite Materials*, pages 1–8, Munich, Germany, 2016.

A. Trauth, P. Pinter, and K. A. Weidenmann. Acoustic emission analysis during bending tests of continuous and discontinuous fiber reinforced polymers to be used in hybrid sheet molding compounds. *Key Engineering Materials*, 742: 644–651, 2017a. doi: 10.4028/www.scientific.net/KEM.742.644.

A. Trauth, P. Pinter, and K. A. Weidenmann. Investigation of quasi-static and dynamic material properties of a structural sheet molding compound combined with acoustic emission damage analysis. *Journal of Composites Science*, 1(2): 18, 2017b. doi: 10.3390/jcs1020018.

A. Trauth, Schubert A., D. Bücheler, and K. A. Weidenmann. Component testing of continuously-discontinuously reinforced hybrid sheet moulding compounds (CoDico SMC). In *Proceedings of the 3rd International Conference Hybrid Materials and Structures*, pages 96–103, Bremen, Germany, 2018.

A. Trauth, K. A. Weidenmann, and W. Altenhof. Puncture properties of a hybrid continuous-discontinuous sheet moulding compound for structural applications. *Composites Part B: Engineering*, 158:46–54, 2019. ISSN 13598368. doi: 10.1016/j.compositesb.2018.09.035.

A. Trauth, K. Kirchenbauer, and K. A. Weidenmann. Dynamic-mechanical-thermal analysis of hybrid continuous–discontinuous sheet molding compounds. *Composites Part C: Open Access*, 5(1140):100148, 2021. ISSN 26666820. doi: 10.1016/j.jcomc.2021.100148.

US Congress. Energy policy and conservation act. *Public law*, 94(163):62, 1975.

W. van Paepegem. Fatigue damage modelling of composite materials with the phenomenological residual stiffness approach. In *Fatigue Life Prediction of Composites and Composite Structures*, pages 102–138. Woodhead Publishing, Cambridge, UK, 2010. ISBN 9781845695255. doi: 10.1533/9781845699796.1.102.

B.S.G von Bernstorff. *Zum Schwingverhalten glasfaserverstärkter Harzmatten*. VDI-Verlag, Düsseldorf, Germany, 1989. ISBN 3-18-147405-3.

S. S. Wang and E.S.-M. Chim. Fatigue damage and degradation in random short-fiber SMC composite. *Journal of Composite Materials*, 17(2):114–134, 1983. ISSN 0021-9983. doi: 10.1177/002199838301700203.

S. S. Wang, E. S.-M. Chim, and H. Suemasu. Mechanics of fatigue damage and degradation in random short-fiber composites, Part II—Analysis of anisotropic property degradation. *Journal of Applied Mechanics*, 53(2):347–353, 1986. ISSN 0021-8936. doi: 10.1115/1.3171763.

J. Wulfsberg, A. Herrmann, G. Ziegmann, G. Lonsdorfer, N. Stöß, and M. Fette. Combination of carbon fibre sheet moulding compound and prepreg compression moulding in aerospace industry. *Procedia Engineering*, 81:1601–1607, 2014. ISSN 18777058. doi: 10.1016/j.proeng.2014.10.197.

R. Yahaya, S. M. Sapuan, M. Jawaid, Z. Leman, and E. S. Zainudin. Quasi-static penetration and ballistic properties of kenaf–aramid hybrid composites. *Materials & Design*, 63:775–782, 2014. ISSN 02641275. doi: 10.1016/j.matdes.2014.07.010.

D. S. Zarouchas, J. A. Pascoe, and R. C. Alderliesten. A cycle-by-cycle fatigue damage analysis of biaxial composite structures utilizing acoustic emission. In *Proceedings of the 18th European Conference on Composite Materials*, pages 1–8, Athens, Greece, 2018.

Y. Zhou, Y. Wang, Y. Xia, and S. Jeelani. Tensile behavior of carbon fiber bundles at different strain rates. *Materials Letters*, 64(3):246–248, 2010. ISSN 0167577X. doi: 10.1016/j.matlet.2009.10.045.

Zoltek. Technical Datasheet - Zoltek PX35 Continuous Tow, 2017. URL `https://zoltek.com/wp-content/uploads/2017/09/TDS_PX35_Continuious_Tow.pdf`. accessed on 23 November 2021.

C. Zweben. Tensile strength of hybrid composites. *Journal of materials science*, 12(7):1325–1337, 1977. doi: 10.1007/BF00540846.